**The Dissertation Committee for Dizem Arifler**
**certifies that this is the approved version of the following dissertation:**

# Reflectance-Based Optical Diagnosis of Epithelial Pre-Cancer: Modeling Spectroscopic Measurements, Fiber-Optic Probe Design Considerations, and Analysis of Tissue Micro-Optical Properties

**Committee:**

Rebecca Richards-Kortum, Supervisor

Michele Follen

Calum MacAulay

H. Grady Rylander, III

Konstantin Sokolov

# Reflectance-Based Optical Diagnosis of Epithelial Pre-Cancer: Modeling Spectroscopic Measurements, Fiber-Optic Probe Design Considerations, and Analysis of Tissue Micro-Optical Properties

**by**

**Dizem Arifler, B.S.; M.S.**

**Dissertation**

Presented to the Faculty of the Graduate School of
The University of Texas at Austin
in Partial Fulfillment
of the Requirements
for the Degree of

**Doctor of Philosophy**

**The University of Texas at Austin**
**August 2005**

# Dedication

To my family.

# Acknowledgements

First, I would like to thank my advisor Dr. Rebecca Richards-Kortum for her guidance and invaluable suggestions concerning all aspects of this research project. Rebecca is an exceptional mentor and working with her for the past five years has been a rewarding experience. Her unmatched enthusiasm and unwavering optimism will have an everlasting influence on my research career. I would also like to thank my committee members Dr. Michele Follen, Dr. Calum MacAulay, Dr. H. Grady Rylander, and Dr. Konstantin Sokolov. It was a privilege to have them on my Ph.D. committee. Their feedback on my research was invaluable. In addition, I thank all members of the Optical Spectroscopy and Imaging Lab for providing such a motivating and fun environment to work. Most of all, I thank my parents and my brother for their love and support. I am forever indebted for their continuous encouragement throughout my education.

Dizem Arifler

*Austin, Texas*

*August 2005*

# Reflectance-Based Optical Diagnosis of Epithelial Pre-Cancer: Modeling Spectroscopic Measurements, Fiber-Optic Probe Design Considerations, and Analysis of Tissue Micro-Optical Properties

Publication No._____________

Dizem Arifler, Ph.D.
The University of Texas at Austin, 2005

Supervisor: Rebecca Richards-Kortum

Optical diagnostic techniques have the potential to improve early detection of pre-cancerous changes in tissues. These techniques can be implemented in real time without the need for biopsy removal, and are expected to have major impact in clinical practice. This dissertation describes a series of modeling studies aimed at establishing an improved understanding of reflectance properties of normal and pre-cancerous epithelial tissues, with the ultimate goal of revealing the potential of reflectance-based optical diagnosis of epithelial pre-cancer.

The first part of the dissertation presents Monte Carlo modeling studies to provide a quantitative understanding of contrast observed in reflectance spectra of normal and pre-cancerous epithelial tissues. Simulation results provide important insights into the specific contributions of different epithelial and stromal optical parameters to the overall spectral response. Predictions from simulations agree well with *in vivo* measurements from cervical tissue, and can successfully describe differences in spatially resolved reflectance spectra of normal and pre-cancerous tissue sites. Monte Carlo modeling is also used to evaluate different fiber-optic probe geometries with respect to sampling depth and to propose a probe design that can resolve spectral information from epithelium and stroma. The proposed design can reveal diagnostic features inherent in optical signatures unique to each of the two tissue layers.

The research presented in the rest of the dissertation is targeted towards analyzing the micro-optical properties of epithelial tissues. The Finite-Difference Time-Domain (FDTD) method, a popular computational technique for solution of problems in electromagnetics, is used to model light scattering from epithelial cells and collagen fibers. FDTD simulation results indicate that morphological and structural changes associated with pre-cancer progression lead to significant alterations in light scattering properties of these microscopic tissue constituents.

The modeling studies presented in this dissertation provide a framework to meaningfully interpret optical signals obtained from epithelial tissues and to optimize design of optical sensors for *in vivo* reflectance measurements. The results obtained throughout this research will aid in development and assessment of optical spectroscopic and imaging techniques for early, noninvasive diagnosis of epithelial pre-cancer.

# Table of Contents

# List of Tables

# List of Figures

# Chapter 1: Introduction

## 1.1 OVERVIEW

Optical diagnostic techniques based on detection of reflected light have the potential to improve noninvasive detection of changes associated with dysplasia. Reflectance spectroscopy is one of these techniques and is based on the fact that tissue optical properties, such as absorption and scattering, change as tissue becomes dysplastic. For *in vivo* clinical studies, fiber-optic probes are widely used to illuminate the tissue with a broadband light source and to collect the reflected light emerging at the tissue surface. The wavelength dependence of the collected light is then analyzed to determine spectral differences resulting from dysplastic changes. Multiple source or detector fibers positioned at different distances within the fiber-optic probe can be used to acquire spatially resolved reflectance spectra.

Recent studies demonstrate the promise of reflectance spectroscopy in detecting early pre-cancerous changes in many organ sites, including the bladder [1, 2], intestine [3], breast [4], esophagus [5], oral cavity [6], skin [7], cervix [8-11], and lung [12]. However, observed differences in reflectance spectra of normal and dysplastic tissue are not completely understood. This dissertation presents modeling studies to explain the differences observed in reflectance spectra of normal and dysplastic epithelial tissue, and to suggest new fiber-optic probe designs for the future. Computational analysis of the light scattering properties of microscopic tissue constituents is performed in parallel to provide a better understanding of how pre-cancerous changes alter light propagation in epithelial tissues, giving rise to intrinsic contrast in reflectance-based optical spectroscopy and imaging.

## 1.2 BACKGROUND AND SIGNIFICANCE

### 1.2.1 Reflectance Spectroscopy for Diagnosis of Epithelial Pre-Cancer and Clinical Studies

Diffuse reflectance spectroscopy is sensitive to the absorption and scattering characteristics of tissue. Dysplastic changes in epithelial tissues include increased scattering from epithelial cells, decreased scattering from collagen fibers in the stroma beneath the epithelium, and increased absorption in the stroma due to increase in hemoglobin concentration. Increased scattering from epithelial cells is due to increased nuclear size, increased DNA content, and hyperchromasia with coarse and irregular chromatin clumping [13]. It is believed that morphological structure of the collagen fibers changes and the volume fraction of fibers decreases as dysplasia develops [14-17], leading to decreased scattering in the stroma. Increase in hemoglobin concentration and hence absorption is the result of increased microvessel density and angiogenic activity in dysplastic tissue [18, 19]. Such structural and biochemical changes are critical diagnostic indicators for development of pre-invasive cancer, and diffuse reflectance spectroscopy is capable of providing information about all of these changes noninvasively.

Many clinical studies have been performed to assess the diagnostic potential of reflectance spectroscopy. Koenig et al. [2] used diffuse reflectance measurements in bladder to extract a parameter related to the total amount of blood and determined that this parameter was useful in discriminating normal and neoplastic tissue. Zonios et al. [3] collected diffuse reflectance measurements from the colon and analyzed the data using an analytical model based on diffusion theory. Extracted parameters including the hemoglobin concentration, hemoglobin oxygen saturation, effective scatterer size, and effective scatterer density were different for normal and pre-cancerous sites, indicating the potential of the method to provide information about tissue structure and composition. Mirabal et al. [10] analyzed spatially resolved reflectance spectra of normal and neoplastic cervix measured *in vivo* and statistical classification performed on these spectra discriminated high-grade neoplastic tissue from squamous normal tissue with a sensitivity of 72% and a specificity of 81%.

Other studies focused on evaluating the use of multi-modal spectroscopy for detection of pre-invasive cancer. Nordstrom et al. [8] measured reflectance and fluorescence spectra from cervical sites and analyzed the results using a multivariate statistical algorithm. The results suggest that fluorescence and reflectance techniques provide complementary information and their combined use increases their diagnostic ability. Müller et al. [20] developed a model to analyze simultaneously acquired fluorescence and reflectance spectra. The authors used information from reflectance spectra to disentangle effects of scattering and absorption and to obtain intrinsic fluorescence due to biological chromophores. The resulting intrinsic fluorescence spectra from normal and cancerous oral and esophageal tissue showed significant differences. Possibility of enhanced performance achievable through combination of reflectance and fluorescence measurements was also revealed in more recent clinical studies exploring the use of optical spectroscopy to complement colposcopy [11] or bronchoscopy [12]. Another multi-modal spectroscopy study by Georgakoudi et al. [9] employed light scattering spectroscopy in addition to reflectance and fluorescence spectroscopy. Light scattering spectroscopy has been shown to provide information about the size of epithelial cell nuclei [21, 22], which is an important diagnostic parameter. Using three spectroscopic techniques simultaneously, the authors obtained a sensitivity and a specificity of 92% and 90%, respectively, in detecting cervical squamous intraepithelial lesions. In a similar trimodal spectroscopy study, Müller et al. [6] achieved a sensitivity and a specificity of 96% and 96%, respectively, in distinguishing dysplastic oral tissue from normal oral tissue.

### 1.2.2 Model-Based Analysis of Reflectance Spectroscopy

Modeling studies are necessary to understand and exploit the information contained in the reflectance spectra of tissues. Analytical models developed are usually based on the diffusion theory, which is an approximate solution to the transport equation that describes photon propagation in a scattering and absorbing medium [23]. Another approach is to simulate photon propagation in tissue using Monte Carlo modeling or photon migration.

Analytical models based on diffusion theory are invertible enabling extraction of optical properties from tissue measurements [3, 24]. However, the validity of the diffusion approximation is very limited. The theory can only be applied to cases where tissue is considered to be a homogeneous semi-infinite turbid medium with scattering and absorption coefficients $\mu_s(\lambda)$ and $\mu_a(\lambda)$, respectively, where $\lambda$ is the wavelength of light. The diffusion approximation generally holds for almost isotropic scattering with $\mu_s(1-g) \gg \mu_a$ [23] and $\rho\mu_s(1-g) > 5$ [25], where $\rho$ is the source-detector separation and $g$, usually referred to as the anisotropy factor, is defined to be the mean cosine of the scattering angle and can be calculated from the phase function. This means that the medium needs to be highly scattering and the distance between the source and the detector needs to be large. Chen et al. [26] also showed that diffusion approximation leads to significant errors for an index-mismatched boundary between the tissue and the outside medium. In epithelial tissues, the epithelium and the underlying stroma have different optical properties, and these two layers cannot be collapsed into a single homogeneous medium. Scattering is mostly forward directed, and although stroma is highly scattering in the ultraviolet and visible wavelength range, the condition $\mu_s(1-g) \gg \mu_a$ is not valid for the epithelial layer. The diffusion model recently described by Ripoll et al. [27] is valid for cases where $\mu_s(1-g) \sim \mu_a$ and scattering is mostly forward directed, but the model is only applicable to homogeneous media. In addition, diffuse reflectance spectroscopy usually involves small source-detector separations that do not satisfy $\rho\mu_s(1-g) > 5$.

Monte Carlo modeling provides a flexible approach to study light propagation in biological tissues. This method traces three-dimensional random walk of photons in a medium, and the probability that a photon is scattered or absorbed after a given step size is determined by local optical properties [28]. The implementation can be modified to account for different source-detector geometries. Internal reflection or refraction at the medium boundaries can be simulated. Since the method is statistical in nature, a significant disadvantage of this technique is that a large number of photons need to be propagated to obtain reliable results. Therefore, the method is computationally intensive and is not easily invertible. Monte Carlo simulations have been widely used to generate spectra for comparison to tissue measurements [29-31], and to investigate the efficiency of different source-detector geometries [32-37]. Pfefer et al. [38] and Swartling et al. [39] have recently employed Monte Carlo simulations to model spatially resolved reflectance measurements for different absorption and scattering coefficients. The authors then used the generated datasets in conjunction with statistical or neural network based algorithms to determine tissue optical properties.

Photon migration is another method to analyze photon propagation in tissue. In this approach, photons are considered to follow probabilistic paths with discrete absorption and scattering events. Diffusely reflected photons collected can be described in terms of an escape probability that only depends on the phase function, and the albedo $a$ given by $\mu_s/(\mu_a+\mu_s)$ [40]. Separation of the phase function dependence from the absorption and scattering coefficients enables calculation of reflectance for different optical properties once the escape probability has been determined. An estimate of the escape probability after a given number of scattering events can be obtained using Monte Carlo simulations [20, 40]. Mathematical formulation of photon migration theory allows model inversion and calculation of optical properties from reflectance measurements.

In the research described in this dissertation, Monte Carlo modeling is used as the main computational framework to generate and analyze spatially resolved reflectance spectra from multi-layered epithelial tissues, and to simulate different fiber-optic probe geometries.

### 1.2.3 Computational Electromagnetics to Study Light Scattering Properties of Microscopic Tissue Constituents

The Finite-Difference Time-Domain (FDTD) method produces a full-vector, three-dimensional solution of Maxwell's equations and allows complex, arbitrarily inhomogeneous structures of any shape to be modeled and studied. A scattering object is constructed in a three-dimensional grid by specifying the dielectric properties of each grid cell belonging to the object, and the scattered fields are calculated via time-marching of discretized curl equations [41]. Over the last several decades, it has been successfully applied in many different disciplines including the study of antennas, from simple monopoles and dipoles to complex arrays, microwave devices, absorption of electromagnetic waves by the human body, and human vision [41, 42]. More recently, the FDTD method has provided a flexible approach to study light scattering that arises from biological cells of arbitrary shape and internal structure [43-49].

In this dissertation, FDTD modeling is used to analyze the scattering properties of epithelial cell nuclei and collagen fibers in the stroma, which are important scatterers in epithelial tissues. A detailed analysis of the micro-optical properties of these tissue scatterers can enhance our understanding of light propagation in normal versus dysplastic epithelial tissue.

## 1.3 SPECIFIC AIMS

Specific aims of this dissertation work are:

- To provide a quantitative understanding of the differences observed in spatially resolved reflectance spectra of normal and dysplastic epithelial tissue. Monte Carlo simulations are used to predict reflectance spectra of normal and dysplastic cervical tissue for different source-detector separations, and the results are compared to spectra measured *in vivo* from patients in different diagnostic categories.
- To carry out Monte Carlo modeling studies to evaluate different fiber-optic probe geometries with respect to their potential in providing depth-resolved reflectance measurements from epithelial tissues. The results are used to propose a fiber-optic probe design that can selectively collect scattered light from both the epithelium and the stroma and thus reveal diagnostic features unique to each tissue layer.

- To study light scattering properties of normal and dysplastic cervical cells at different epithelial depths using FDTD modeling. Construction of cervical cells within the FDTD computational grid is based on morphological and chromatin texture features obtained from quantitative histopathology.
- To study light scattering properties of collagen fibers using FDTD modeling. The FDTD method is used to establish a relationship between structural properties of collagen fiber meshes and light scattering. Fluorescence confocal images of normal and cancerous oral cavity biopsy samples are used to create realistic model input for FDTD simulations.

## 1.4 ORGANIZATION OF THE DISSERTATION

The outline of the rest of the dissertation is as follows. *Chapter 2* and *Chapter 3* describe the computational framework employed in this research work. *Chapter 2* gives a brief review of the basic principles of Monte Carlo modeling, whereas *Chapter 3* provides a detailed introduction to FDTD modeling. *Chapter 4* through *Chapter 7* present four studies carried out to tackle the specific aims described in the previous section, with each chapter focusing on a single aim in the order listed. *Chapter 8* gives a brief summary of the work described in this dissertation and discusses some possible future research directions.

# Chapter 2: Monte Carlo Modeling

## 2.1 INTRODUCTION

Monte Carlo modeling provides a flexible approach to study light propagation in multi-layered turbid media. This method traces three-dimensional random walk of photons in a medium, and the rules for photon propagation rely on random sampling from well-defined probability distributions that depend on local optical properties. Internal reflection or refraction at the layer boundaries can be simulated. The implementation can be modified to account for different source-detector geometries. The method is statistical in nature, and a large number of photons need to be propagated in order to obtain rigorous results.

This chapter gives a brief description of the basic principles of Monte Carlo modeling and introduces the terminology that will be used throughout the rest of the dissertation in relation to spatially resolved reflectance spectroscopy. The Monte Carlo method described in this chapter is based on a fixed-weight photon model. This means that the photon is treated as an intact particle and cannot be partially absorbed or reflected. Variable-weight photon models have been introduced to improve the efficiency of Monte Carlo simulations [50], but these models will not be discussed here. Details about theoretical formulation and implementation of fixed-weight or variable-weight modeling schemes can be found in well-established references including [28, 50]. These references also provide information on how to sample random variables from a given probability density function.

## 2.2 MONTE CARLO MODELING

### 2.2.1 Simulation Geometry

The layers of the turbid medium under consideration are assumed to be infinitely wide and parallel to each other. Each layer is described by a thickness *D* and several optical properties including the refractive index *n*, absorption coefficient $\mu_a$, scattering coefficient $\mu_s$, and anisotropy factor *g*. The simulation geometry is illustrated in Fig. 2.1.

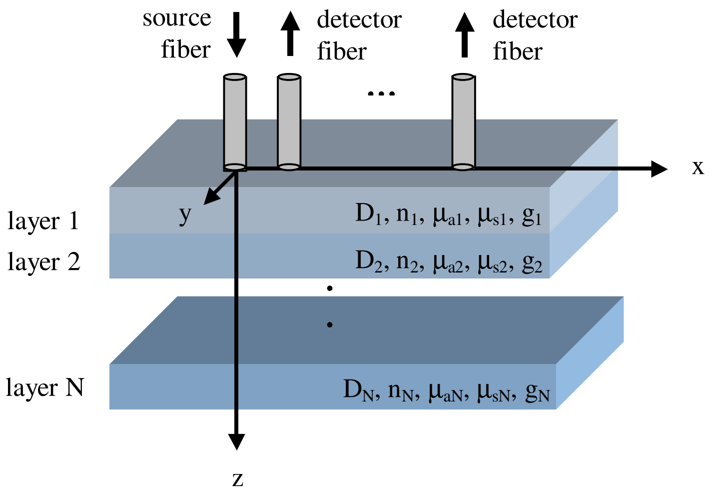

Figure 2.1: Multi-layered Monte Carlo simulation geometry. Each layer is described by five parameters (*D*: layer thickness, *n*: refractive index, $\mu_a$: absorption coefficient, $\mu_s$: scattering coefficient, *g*: anisotropy factor).

The absorption coefficient is defined as the probability of photon absorption per unit infinitesimal pathlength, and the scattering coefficient is defined as the probability of photon scattering per unit infinitesimal pathlength

[28]. The anisotropy factor characterizes the change in direction of propagation upon scattering. As Fig. 2.1 indicates, simulations can be carried out using a source fiber centered at the origin and multiple detector fibers placed along the *x* axis at different distances from the source fiber.

### 2.2.2 Photon Launch

The source fiber is described by its radius, numerical aperture in air (NA), and refractive index. When the source fiber is oriented so that its axis is perpendicular to the medium surface, as shown in Fig. 2.1, the initial position of each photon is uniformly sampled from a circular region defined by the radius of the fiber. The initial propagation angle with respect to the *z* axis is sampled from an illumination cone determined by the fiber NA and refractive index. If the refractive index of the source fiber is denoted by $n_{sf}$, this angle will range from 0 to $\sin^{-1}(\mathrm{NA}/n_{sf})$. The azimuthal entry angle is uniformly distributed between 0 and $2\pi$.

### 2.2.3 Photon Propagation

After the photon is launched, if there is an index mismatch between the source fiber and the first layer of the medium, specular reflection can occur. The probability of specular reflection is determined using the Fresnel relation. If there is no specular reflection, the photon enters the first layer and the direction of photon propagation is updated using Snell's law.

Within the turbid medium, there are two parameters that determine photon propagation profile. The first of these parameters is the step size between each scattering or absorption event. The step size is related to the frequency of photon interaction with the turbid medium, and is sampled from a probability distribution that depends on the sum of the local absorption and scattering coefficients. If the step size is denoted by $\Delta s$, this probability distribution can be expressed as [28]

$$\wp(\Delta s) = (\mu_a + \mu_s)\exp[-(\mu_a + \mu_s)\Delta s]. \tag{2.1}$$

The second parameter of interest is the scattering angle that describes how the direction of propagation changes at each scattering event. The probability distribution for the cosine of the deflection angle, $\cos\theta$, is described by the Henyey-Greenstein phase function. This function approximates the scattering patterns calculated by Mie theory for homogeneous spherical scatterers, and is given by [28]

$$\wp(\cos\theta) = \frac{1-g^2}{2(1+g^2-2g\cos\theta)^{3/2}}, \tag{2.2}$$

where the anisotropy factor, $g$, represents the expected value of $\cos\theta$. A high $g$ value is indicative of mostly forward directed scattering. The deflection angle $\theta$ is sampled from the Henyey-Greenstein phase function. The azimuthal scattering angle is assumed to be uniformly distributed between 0 and 2π.

At each interaction site, the decision of photon absorption or scattering is based on the relative values of the local absorption and scattering coefficients. If the photon attempts to cross a layer boundary, the probability of internal reflection or refraction is determined by the Fresnel reflection coefficient. If layer crossing occurs, the direction of propagation is updated by taking into account the difference in refractive indices. The step size is also adjusted to reflect the changes in absorption and scattering coefficients.

Note that the implementation described here is general enough to simulate clear layers with no scattering or absorption. If the photon encounters a clear layer, it is automatically moved to the boundary of the next layer unless it is internally reflected.

### 2.2.4 Photon Detection

Each detector fiber is described by its radius, NA, refractive index, and a source-detector separation that represents the center-to-center distance between the source fiber and the detector fiber in question. Reflected photons emerging at the surface of the medium are detected when they exit under any of the detector fibers and their propagation direction at the exit point is within the collection cone determined by the NA and refractive index of that detector fiber. If the refractive index of the detector fiber is given by $n_{df}$, the collection cone will span the angular range from 0 to $\sin^{-1}(NA/n_{df})$ with respect to the $z$ axis.

### 2.2.5 Simulation Output

The output of each Monte Carlo simulation includes reflectance intensity detected at each detector fiber. Detected reflectance intensity is obtained by taking the ratio of the number of photons detected at the detector fiber to the total number of photons propagated. In addition to the reflectance intensity, several descriptive parameters can be recorded for every photon detected during each simulation. These parameters include penetration depth of the photon and the number of scattering events the photon undergoes in each layer. Such information on a per-photon basis can be used to provide significant insight into differences in detection profiles of the detector fibers under consideration.

## 2.3 VERIFICATION OF THE IMPLEMENTED MONTE CARLO CODE

The fixed-weight, multi-layered Monte Carlo code used for the simulations presented in this dissertation has been implemented in C/C++. The code has been validated using single and multi-layered tissue geometries and the corresponding reflectance results reported previously in the literature [28, 50-52]. Although most of these results have been obtained for infinitely narrow photon beam perpendicularly incident on tissue surface, they collectively provide a standard to test the basic Monte Carlo implementation. Table 2.1 through Table 2.3 describe some of the tissue geometries tested and compare the reflectance results obtained using the implemented code to those reported in the literature. In all cases, the refractive index of the medium outside the tissue is assumed to be 1.0, and the total number of photons simulated is $10^6$.

Table 2.1: Validation of the implemented Monte Carlo code using a single layer tissue geometry.

| Tissue Geometry | | | | | | Overall Reflectance | |
|---|---|---|---|---|---|---|---|
| Layer | D (cm) | n | $\mu_a$ ($cm^{-1}$) | $\mu_s$ ($cm^{-1}$) | g | Result from [28, 50] | Result from Implemented Code |
| 1 | $\infty$ | 1.50 | 10.0 | 90 | 0.00 | 0.260 | 0.260 |

Table 2.2: Validation of the implemented Monte Carlo code using a two-layer tissue geometry.

| Tissue Geometry | | | | | | Overall Reflectance | |
|---|---|---|---|---|---|---|---|
| Layer | D (cm) | n | $\mu_a$ ($cm^{-1}$) | $\mu_s$ ($cm^{-1}$) | g | Result from [51] | Result from Implemented Code |
| 1 | 0.03 | 1.00 | 7.5 | 240 | 0.85 | 0.289 | 0.288 |
| 2 | $\infty$ | 1.00 | 6.5 | 412 | 0.89 | | |

Table 2.3: Validation of the implemented Monte Carlo code using a three-layer tissue geometry.

| Tissue Geometry | | | | | | Overall Reflectance | |
|---|---|---|---|---|---|---|---|
| Layer | D (cm) | n | $\mu_a$ ($cm^{-1}$) | $\mu_s$ ($cm^{-1}$) | g | Result from [52] | Result from Implemented Code |
| 1 | 0.10 | 1.37 | 1.0 | 100 | 0.90 | 0.262 | 0.262 |
| 2 | 0.10 | 1.37 | 1.0 | 10 | 0.00 | | |
| 3 | 0.20 | 1.37 | 2.0 | 10 | 0.70 | | |

The results shown in Table 2.1 through Table 2.3 demonstrate that the overall reflectance intensities computed using the implemented code agree with those reported previously. Note that $10^6$ photons are sufficient to obtain reliable results for overall reflectance. When specific source-detector geometries are modeled, however, the total number of photons simulated needs to be significantly larger to achieve convergence of results for detected reflectance intensity.

# Chapter 3: Finite-Difference Time-Domain Modeling

## 3.1 INTRODUCTION

The Finite-Difference Time-Domain (FDTD) method is one of the most popular numerical methods for the solution of problems in electromagnetics. The method was first proposed by Yee in 1966, but initially it did not receive much attention. This was due to the high computational costs of the method and also due to its inability to model open-region problems [41, 42]. However, the method quickly gained popularity with considerable increase in computational power and decrease in computational costs. Also, many different boundary conditions have been developed to efficiently truncate computational domains, enabling the solution of electromagnetic wave interaction problems in unbounded regions.

This chapter describes the basic FDTD algorithm in three dimensions and the perfectly matched layer (PML) boundary condition, which is currently considered to be one of the most efficient boundary conditions in truncating computational domains.

## 3.2 THREE-DIMENSIONAL FDTD METHOD

### 3.2.1 The Yee Algorithm

The Yee Algorithm can be used to solve Maxwell's curl equations using the FDTD method. Maxwell's curl equations for an isotropic medium are

$$\nabla\times\vec{E}=-\mu\frac{\partial\vec{H}}{\partial t}, \tag{3.1}$$

and

$$\nabla\times\vec{H}=\sigma\vec{E}+\varepsilon\frac{\partial\vec{E}}{\partial t}. \tag{3.2}$$

In Equations (3.1) and (3.2), $\mu$ is the magnetic permeability, $\sigma$ is the electric conductivity, and $\varepsilon$ is the dielectric permittivity. The Yee Algorithm takes these curl equations and discretizes them in space and time, resulting in a set of six explicit finite-difference equations, one for each electric or magnetic field component. Examples of the finite-difference equations for the *x* component of the magnetic field, $H_x$, and the *y* component of the electric field, $E_y$, are [41, 53]

$$\begin{aligned} H_x^{n+1/2}(i,j+1/2,k+1/2) &= H_x^{n-1/2}(i,j+1/2,k+1/2) \\ &+\left\{\left(\frac{\Delta t}{\delta\mu(i,j+1/2,k+1/2)}\right)\begin{bmatrix} E_y^n(i,j+1/2,k+1)-E_y^n(i,j+1/2,k) \\ +E_z^n(i,j,k+1/2)-E_z^n(i,j+1,k+1/2)\end{bmatrix}\right\}, \end{aligned} \tag{3.3}$$

and

$$\begin{aligned} E_y^{n+1}(i,j+1/2,k) &= \left(1-\frac{\Delta t\sigma(i,j+1/2,k)}{\varepsilon(i,j+1/2,k)}\right)E_y^n(i,j+1/2,k) \\ &+\left\{\left(\frac{\Delta t}{\delta\varepsilon(i,j+1/2,k)}\right)\begin{bmatrix} H_x^{n+1/2}(i,j+1/2,k+1/2)-H_x^{n+1/2}(i,j+1/2,k-1/2) \\ +H_z^{n+1/2}(i-1/2,j+1/2,k)-H_z^{n+1/2}(i+1/2,j+1/2,k)\end{bmatrix}\right\}. \end{aligned} \tag{3.4}$$

Similar equations exist for the remaining electric and magnetic field components [41, 53].

In Equations (3.3) and (3.4), *(i, j, k)* is the location of a grid point, $\Delta t$ is the temporal step size, and $\delta$ is the spatial step size that is assumed to be equal for every direction. The time step is indicated by the superscript $n$. In all of the finite-difference equations, the electric and magnetic field components are located within a single unit cell as shown in Fig. 3.1 below. In Fig. 3.1, the red arrows denote the electric field components and the blue arrows denote the magnetic field components.

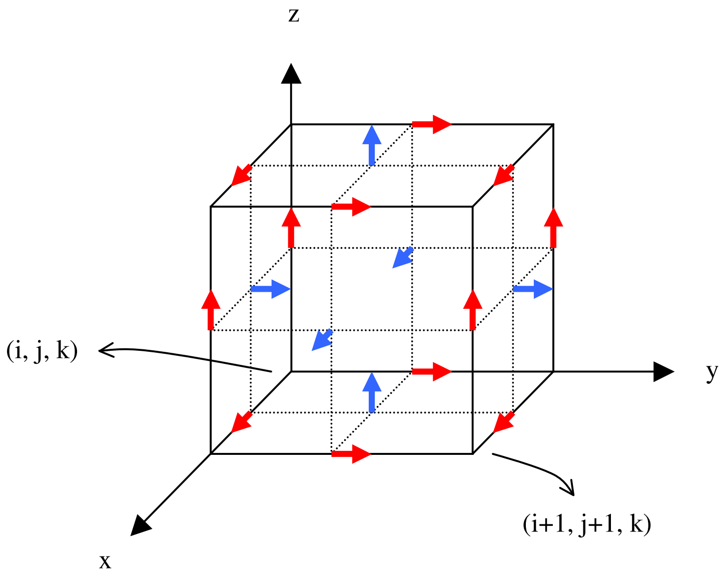

Figure 3.1: Yee cell showing the arrangement of electric field components (as red arrows) and magnetic field components (as blue arrows). The arrows are pointed in the direction of the associated field components.

The electric and magnetic field components are evaluated at alternate half-time steps so that all field components are calculated in each time step $\Delta t$. To obtain stable results, the grid spacing $\delta$ must be less than $\lambda/10$, where $\lambda$ is the wavelength [41]. Also, the time step $\Delta t$ has an upper bound set by the Courant stability condition. The Courant stability condition for three dimensions requires that $\Delta t$ be less than $\delta/(\sqrt{3}\upsilon_{\max})$, where $\upsilon_{max}$ is the maximum wave phase velocity expected within the model [41].

### 3.2.2 Total Field/Scattered Field Formulation

The incident wave is not included in the finite-difference equations, and is therefore applied separately. The total field/scattered field formulation can be used to propagate a variety of excitation waveforms. In this formulation, the computational grid is divided into two regions, the scattered field region and the total field region, as shown in Fig. 3.2 below.

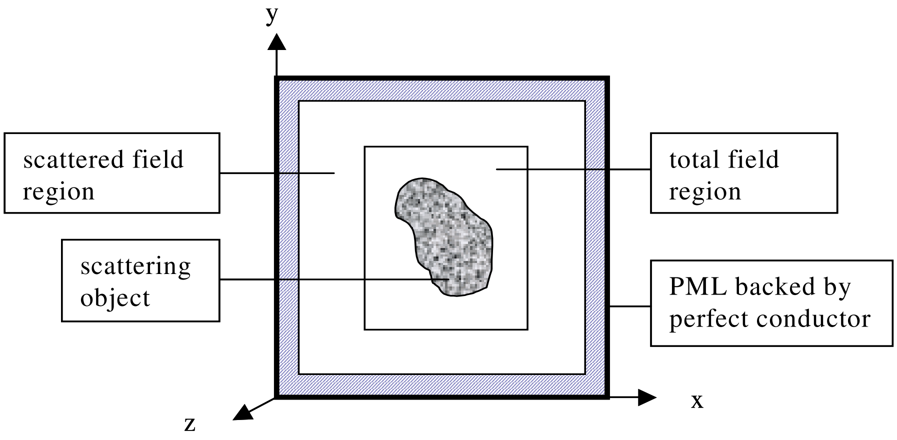

Figure 3.2: Geometry of the FDTD simulation (A section through the xy plane is shown).

At the border between the two regions, special connecting conditions, in which the incident field is either added or subtracted from the total field values, need to be applied. These connecting conditions for the field components are described in detail in [41].

The simulations described in this dissertation will involve a sinusoidal plane wave as the excitation source. Figure 3.2 also shows the PML region backed by perfectly conducting walls. The PML boundary condition is described in the next section.

### 3.2.3 PML Boundary Condition

#### *3.2.3.1 Introduction*

Since the introduction of the FDTD method, there have been numerous attempts to develop absorbing boundary conditions (ABCs) that produce negligible reflections at the outer boundary of the computational domain. Most of the popular ABCs formulated over the years can be grouped into two categories: ABCs derived from differential equations or ABCs employing a material absorber.

Differential-equation-based ABCs allow a solution that permits only outgoing waves. This category includes the boundary conditions formulated by Engquist and Majda, Mur, and Liao [41]. Material-based ABCs are obtained by surrounding the computational domain with a lossy material that dampens the outgoing fields. The perfectly matched layer (PML) technique, introduced by Berenger in 1994, can be considered to employ a material absorber and has been shown to provide significantly better accuracy than most other ABCs [42, 54, 55].

Following Berenger's work, many papers appeared suggesting ways to optimize the performance of PML and to reduce the thickness of the optimum PML. The PML ABC described in this section is based on Berenger's original formulation [42, 54, 55].

### *3.2.3.2 Definition of the PML medium*

To examine the characteristics of a reflectionless interface, let us first consider a plane wave incident from a free space onto a material half-space, as shown in Fig. 3.3.

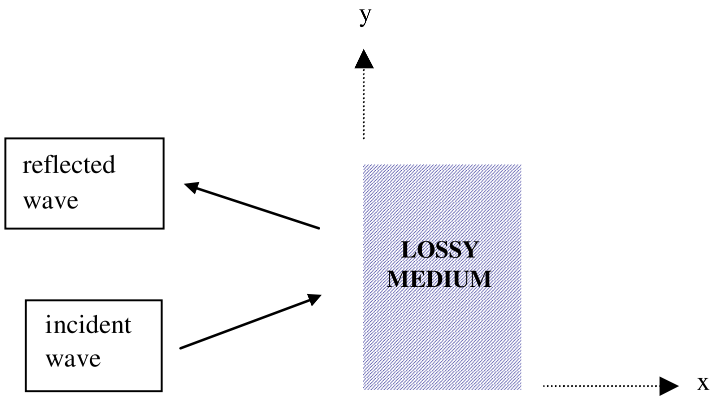

Figure 3.3: Plane wave incident on a lossy half-space.

The material half-space has both an electric conductivity, $\sigma$, and a magnetic conductivity, $\sigma^*$. If, for example, a $TE_z$-polarized uniform plane wave given by

$$\vec{H}^{inc} = \hat{z} H_o \exp(-j\beta_x^i x - j\beta_y^i y) \tag{3.5}$$

is incident upon the interface, the fields in the region x<0 are

$$\vec{H}_1 = \hat{z} H_o (1 + \Gamma e^{2j\beta_x^i x}) e^{-j\beta_x^i x - j\beta_y^i y}, \tag{3.6}$$

$$\vec{E}_1 = \left[ -\hat{x} \frac{\beta_y^i}{\omega \varepsilon_1} \left( 1 + \Gamma e^{2j\beta_x^i x} \right) + \hat{y} \frac{\beta_x^i}{\omega \varepsilon_1} \left( 1 - \Gamma e^{2j\beta_x^i x} \right) \right] H_o e^{-j\beta_x^i x - \beta_y^i y}, \tag{3.7}$$

and the fields in the region x>0 are

$$\vec{H}_2 = \hat{z} H_o \tau e^{-j\beta_x^t x - j\beta_y^t y}, \tag{3.8}$$

$$\vec{E}_2 = \left[ -\hat{x} \frac{\beta_y^t}{\omega \varepsilon_2 \left( 1 + \dfrac{\sigma}{j\omega \varepsilon_2} \right)} + \hat{y} \frac{\beta_x^t}{\omega \varepsilon_2 \left( 1 + \dfrac{\sigma}{j\omega \varepsilon_2} \right)} \right] H_o \tau e^{-j\beta_x^t x - \beta_y^t y}, \tag{3.9}$$

where $\Gamma$ and $\tau$ are the reflection and transmission coefficients, respectively. Note that in Equations (3.5) – (3.9), the superscript *i* refers to the incident wave, the superscript *t* refers to the transmitted wave, and $\beta^i$ and $\beta^t$ are defined by

$$\beta_x^i = k_1 \cos\theta^i, \tag{3.10}$$

$$\beta_y^i = k_1 \sin\theta^i, \tag{3.11}$$

and

$$\beta_x^t = \sqrt{(k_2)^2 \left( 1 + \frac{\sigma}{j\omega \varepsilon_2} \right) \left( 1 + \frac{\sigma^*}{j\omega \mu_2} \right) - \left( \beta_y^t \right)^2}, \tag{3.12}$$

where $\theta^i$ is the incidence angle relative to the interface normal, $k_1=\omega\sqrt{(\varepsilon_1\mu_1)}$, and $k_2=\omega\sqrt{(\varepsilon_2\mu_2)}$. Enforcement of the continuity of the tangential fields across the boundary interface at x=0 gives

$$\Gamma=\frac{\dfrac{\beta_x^i}{\omega\varepsilon_1}-\dfrac{\beta_x^t}{\omega\varepsilon_2\left(1+\dfrac{\sigma}{j\omega\varepsilon_2}\right)}}{\dfrac{\beta_x^i}{\omega\varepsilon_1}+\dfrac{\beta_x^t}{\omega\varepsilon_2\left(1+\dfrac{\sigma}{j\omega\varepsilon_2}\right)}}, \tag{3.13}$$

$$\tau=1+\Gamma, \tag{3.14}$$

and

$$\beta_y^t=\beta_y^i=k_1\sin\theta^i. \tag{3.15}$$

For a normally incident wave ($\theta^i=0$), Equation (3.13) simplifies to

$$\Gamma=\frac{\eta_1-\eta_2}{\eta_1+\eta_2}, \tag{3.16}$$

where $\eta_1$ and $\eta_2$ are the characteristic impedances of the free space and the lossy medium, respectively, and are given by

$$\eta_1=\sqrt{\frac{\mu_1}{\varepsilon_1}}, \tag{3.17}$$

$$\eta_2 = \sqrt{\frac{\mu_2\left(1+\dfrac{\sigma^*}{j\omega\mu_2}\right)}{\varepsilon_2\left(1+\dfrac{\sigma}{j\omega\varepsilon_2}\right)}}. \tag{3.18}$$

Additionally, if $\mu_1=\mu_2$, $\varepsilon_1=\varepsilon_2$, and

$$\frac{\sigma^*}{\mu_1} = \frac{\sigma}{\varepsilon_1}, \tag{3.19}$$

then $\Gamma=0$. Also, Equation (3.12) becomes

$$\beta_x^t = \left(1+\frac{\sigma}{j\omega\varepsilon_1}\right)k_1 = k_1 - j\sigma\eta_1. \tag{3.20}$$

The real part of Equation (3.20) represents the propagating component of the wave, and the imaginary part represents the attenuating component. The equation shows that the wave speed in the lossy medium is identical to that in free space and that the wave is dispersionless, that is the wave speed is independent of frequency for an axially propagating wave. Equations (3.8) and (3.9) can then be expressed as

$$\vec{H}_2 = \hat{z}H_o \exp(-jk_1x)\exp(-\sigma\eta_1x), \tag{3.21}$$

$$\vec{E}_2 = \hat{y}\eta_1H_o \exp(-jk_1x)\exp(-\sigma\eta_1x). \tag{3.22}$$

Therefore, a medium with electric and magnetic conductivity defined by Equation (3.19) is matched across a planar boundary for all normally incident waves. The wave propagating in this medium has the same propagation characteristics as the incident wave, but attenuates along the normal direction. The fact that the medium is matched for only normally incident waves, however, puts a limitation on the use of such an absorbing medium since obliquely incident waves partially reflect back into the computational domain giving rise to inaccurate solutions.

Berenger proposed that by splitting each component of the electromagnetic field into two orthogonal subcomponents, the medium could be matched even at oblique incidence. In three dimensions, the six field components yield twelve subcomponents denoted as $E_{xy}$, $E_{xz}$, $E_{yx}$, $E_{yz}$, $E_{zx}$, $E_{zy}$, $H_{xy}$, $H_{xz}$, $H_{yx}$, $H_{yz}$, $H_{zx}$, $H_{zy}$. Examples of the resulting Maxwell's time-dependent curl equations are [55, 56]

$$\mu\frac{\partial H_{xy}}{\partial t}+\sigma_y^* H_{xy}=-\frac{\partial\left(E_{zx}+E_{zy}\right)}{\partial y}, \tag{3.23}$$

$$\mu\frac{\partial H_{xz}}{\partial t}+\sigma_z^* H_{xz}=\frac{\partial\left(E_{yz}+E_{yx}\right)}{\partial z}, \tag{3.24}$$

$$\varepsilon\frac{\partial E_{yz}}{\partial t}+\sigma_z E_{yz}=\frac{\partial\left(H_{xy}+H_{xz}\right)}{\partial z}, \tag{3.25}$$

$$\varepsilon\frac{\partial E_{yx}}{\partial t}+\sigma_x E_{yx}=-\frac{\partial\left(H_{zx}+H_{zy}\right)}{\partial x}, \tag{3.26}$$

where $(\sigma_x, \sigma_x^*, \sigma_y, \sigma_y^*, \sigma_z, \sigma_z^*)$ are the electric and magnetic conductivities in the associated direction. The equations for the remaining split field components can be found in [55, 56]. Following an analysis similar to one described above, Berenger shows in [55] that for both $TE_z$- and $TM_z$-polarized waves incident at an interface normal to $x$, there will be no reflection at any angle of incidence and at any frequency if

- $\mu_1=\mu_2$ and $\varepsilon_1=\varepsilon_2$,
- the transverse conductivities $(\sigma_y, \sigma_y^*, \sigma_z, \sigma_z^*)$ for both media are equal, and
- all couples of conductivities satisfy the matching impedance condition given by Equation (3.19).

These properties are also valid at interfaces normal to $y$ and normal to $z$, the transverse conductivities being $(\sigma_x, \sigma_x^*, \sigma_z, \sigma_z^*)$ and $(\sigma_x, \sigma_x^*, \sigma_y, \sigma_y^*)$, respectively.

Since any wave can be split into TE and TM polarizations, any propagating wave of arbitrary incidence, polarization, and frequency is matched at the boundary. Berenger called this absorbing medium the perfectly matched layer (PML) for the absorption of electromagnetic waves.

#### *3.2.3.3 Numerical implementation of the PML boundary condition*

When implementing the PML ABC within the FDTD method, the attenuation of the waves in the PML medium can be so rapid that standard Yee time stepping described in *Section 3.2.1* cannot be used. A suitable alternative is exponential time stepping [41]. The exponentially discretized equations corresponding to (3.23) – (3.26) are

$$\begin{aligned}
H_{xy}^{n+\frac{1}{2}}(i, j+\tfrac{1}{2}, k+\tfrac{1}{2}) &= \exp\left(\frac{-\eta^{2}\sigma_{y}(j+\frac{1}{2})\Delta t}{\mu}\right) H_{xy}^{n-\frac{1}{2}}(i, j+\tfrac{1}{2}, k+\tfrac{1}{2}) \\
&- \left\{ \left( \frac{1-\exp\left(\dfrac{-\eta^{2}\sigma_{y}(j+\frac{1}{2})\Delta t}{\mu}\right)}{\eta^{2}\sigma_{y}(j+\frac{1}{2})\delta} \right) \times \begin{bmatrix} E_{zx}^{n}(i, j+1, k+\frac{1}{2}) + E_{zy}^{n}(i, j+1, k+\frac{1}{2}) \\ -E_{zx}^{n}(i, j, k+\frac{1}{2}) - E_{zy}^{n}(i, j, k+\frac{1}{2}) \end{bmatrix} \right\},
\end{aligned} \tag{3.27}$$

$$\begin{aligned}
H_{xz}^{n+\frac{1}{2}}(i, j+\tfrac{1}{2}, k+\tfrac{1}{2}) &= \exp\left(\frac{-\eta^{2}\sigma_{z}(k+\frac{1}{2})\Delta t}{\mu}\right) H_{xz}^{n-\frac{1}{2}}(i, j+\tfrac{1}{2}, k+\tfrac{1}{2}) \\
&+ \left\{ \left( \frac{1-\exp\left(\dfrac{-\eta^{2}\sigma_{z}(k+\frac{1}{2})\Delta t}{\mu}\right)}{\eta^{2}\sigma_{z}(k+\frac{1}{2})\delta} \right) \times \begin{bmatrix} E_{yx}^{n}(i, j+\frac{1}{2}, k+1) + E_{yz}^{n}(i, j+\frac{1}{2}, k+1) \\ -E_{yx}^{n}(i, j+\frac{1}{2}, k) - E_{yz}^{n}(i, j+\frac{1}{2}, k) \end{bmatrix} \right\},
\end{aligned} \tag{3.28}$$

$$\begin{aligned}
E_{yz}^{n+1}(i, j+\tfrac{1}{2}, k) &= \exp\left(\frac{-\sigma_{z}(k)\Delta t}{\varepsilon}\right) E_{yz}^{n}(i, j+\tfrac{1}{2}, k) \\
&+ \left\{ \left( \frac{1-\exp\left(\dfrac{-\sigma_{z}(k)\Delta t}{\varepsilon}\right)}{\sigma_{z}(k)\delta} \right) \times \begin{bmatrix} H_{xy}^{n+\frac{1}{2}}(i, j+\frac{1}{2}, k+\frac{1}{2}) + H_{xz}^{n+\frac{1}{2}}(i, j+\frac{1}{2}, k+\frac{1}{2}) \\ -H_{xy}^{n+\frac{1}{2}}(i, j+\frac{1}{2}, k-\frac{1}{2}) - H_{xz}^{n+\frac{1}{2}}(i, j+\frac{1}{2}, k-\frac{1}{2}) \end{bmatrix} \right\},
\end{aligned} \tag{3.29}$$

and

$$E_{yx}^{n+1}(i,j+\tfrac{1}{2},k)=\exp\left(\frac{-\sigma_x(i)\Delta t}{\varepsilon}\right)E_{yx}^{n}(i,j+\tfrac{1}{2},k)$$
$$-\left\{\begin{array}{l}\left(\dfrac{1-\exp\left(\dfrac{-\sigma_x(i)\Delta t}{\varepsilon}\right)}{\sigma_x(i)\delta}\right)\times \\ \left[\begin{array}{l}H_{zx}^{n+\frac{1}{2}}(i+\tfrac{1}{2},j+\tfrac{1}{2},k)+H_{zy}^{n+\frac{1}{2}}(i+\tfrac{1}{2},j+\tfrac{1}{2},k)\\ -H_{zx}^{n+\frac{1}{2}}(i-\tfrac{1}{2},j+\tfrac{1}{2},k)-H_{zy}^{n+\frac{1}{2}}(i-\tfrac{1}{2},j+\tfrac{1}{2},k)\end{array}\right]\end{array}\right\}. \tag{3.30}$$

Note that the magnetic conductivities $\sigma_i^*$ (i=x, y, z) of Equations (3.23) – (3.24) have been substituted by $\sigma_i^*=(\sigma_i\mu)/\varepsilon=\sigma_i\eta^2$ in Equations (3.27) – (3.28) using the matching condition given by Equation (3.19).

When used to truncate a computational domain, the PML must have a finite thickness and be terminated by a boundary. This boundary can be a perfectly conducting (PEC) wall, as shown in Fig. 3.2. Waves then reflect back into the interior FDTD domain. This reflection has an amplitude of [42]

$$R(\theta)=\exp(-2\sigma\eta\varepsilon_r d\cos\theta), \tag{3.31}$$

where $\theta$ is the angle of incidence, $d$ is the thickness of the PML medium, $\eta$ is the characteristic impedance of the medium to be terminated by the PML, $\sigma$ is the conductivity of the PML, $\varepsilon_r$ is the relative permittivity, and $R(\theta)$ is referred to as the reflection error.

Figure 3.4 below illustrates how a six-sided domain can be terminated by the PML. The figure shows the upper right corner of the computational domain and the conductivities associated with three sides, three edges and a corner.

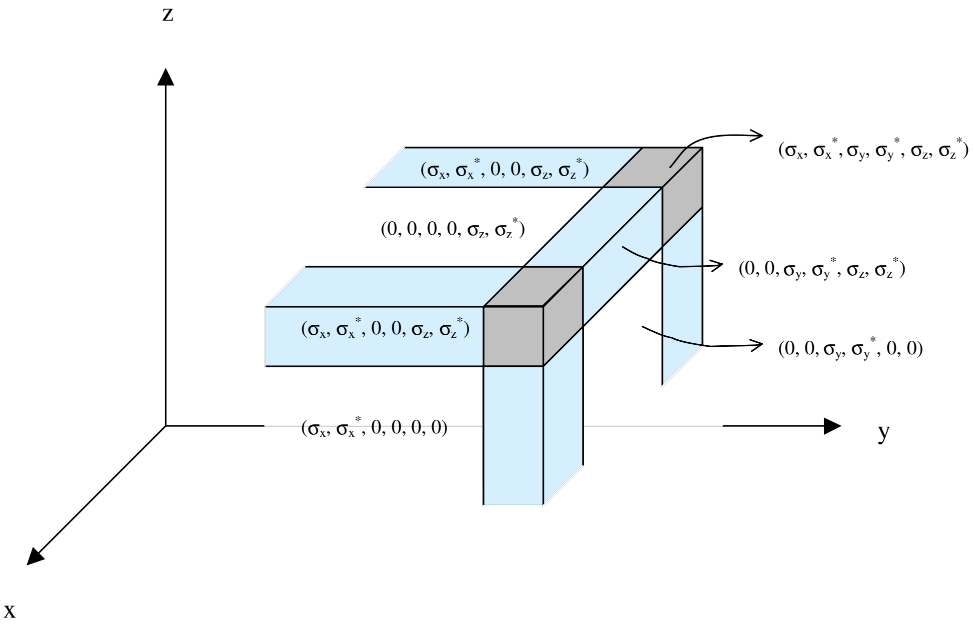

Figure 3.4: Upper right corner of a computational domain terminated by the PML.

In the six sides of the domain, the absorbing media to terminate non-conductive medium are matched PML media of transverse conductivities equal to zero, for instance, $(0, 0, 0, 0, \sigma_z, \sigma_z^*)$ medium in the upper side of the domain. As a result, outgoing waves from the inner domain can penetrate into these absorbing media without reflection. In the twelve edges, the conductivities are selected such that the transverse conductivities are equal at the interfaces located between the edge media and the side media. In Fig. 3.4 for example, $(\sigma_x, \sigma_x^*, 0, 0, \sigma_z, \sigma_z^*)$

medium is used to connect $(0, 0, 0, 0, \sigma_z, \sigma_z^*)$ and $(\sigma_x, \sigma_x^*, 0, 0, 0, 0)$ media. This ensures that there is theoretically no reflection from the side-edge interfaces. Finally, in the eight corners of the domain, the conductivities are chosen equal to those of adjacent edges, so that the transverse conductivities are equal at the interfaces between the edge layers and the corners, as illustrated in Fig. 3.4. Therefore, the reflection equals zero from all edge-corner interfaces [55].

In the inner domain, the finite-difference equations are the usual Yee time stepping equations. In the PML, the split field components need to be updated using exponential time stepping. Evaluation of the field components at the interface requires the field values from both regions. This, in fact, ensures the continuity of tangential components at the interface. The presence of the PEC wall at the outer PML boundary can be simulated numerically by setting the tangential electric field component values to zero.

In discrete-space representation of the FDTD method, the PML interface presents a discontinuity in both the electric and magnetic conductivity. These discontinuities can lead to significant discretization errors resulting in spurious reflections. To reduce these reflections, the conductivity profile can be scaled along the normal axis. A suitable profile of conductivity when solving wave-structure interaction problems is a geometric progression of ratio $g$ that can be expressed as [57, 58]

$$\sigma(\rho) = \sigma_o g^{\rho/\delta}, \tag{3.32}$$

where $\sigma_o$ is the conductivity at the interface between the PML and the inner domain, $\rho$ is the distance from the interface, and $\delta$ is the FDTD space increment as indicated before. The modified version of Equation (3.31) is

$$R(\theta) = \exp\left[ -2\eta\varepsilon_r \cos\theta \int_0^d \sigma(\rho) d\rho \right], \tag{3.33}$$

and substituting (3.32) into (3.33) gives

$$R(\theta) = \exp\left[ \frac{-2\eta\varepsilon_r\sigma_o\delta\left(g^N - 1\right)\cos\theta}{\ln g} \right], \tag{3.34}$$

where *N* is the number of cells in the PML. Normally, the parameters *g*, *d*, and *R(0)* are predetermined, and the conductivity profile is then expressed as [42, 57, 58]

$$\sigma(\rho) = -\frac{\ln\left[R(0)\right]\ln g}{2\eta\varepsilon_r\delta(g^N - 1)} g^{\rho/\delta}. \tag{3.35}$$

Theoretically, the conductivity should be scaled from a small value at the interface between the PML and the inner domain to a very large value at the PEC interface to minimize the reflection error *R(θ)*. This, however, can lead to numerical discretization errors if the PML thickness is small. Therefore, the design of an effective PML requires balancing *R(θ)* and the numerical discretization error by trying to select optimal values for *g*, *N*, and *R(0)* for the specific domain size under study.

### 3.2.4 Far-Field Transform

The FDTD method computes the near field values in a region around the scattering structure. To compute the far-field values, frequency-domain near-field to far-field transformation (FD-NFFFT) is used [42]. First, a transformation surface *S* enclosing the total field region is defined. In three dimensions, this surface consists of six rectangular faces. Figure 3.5 below shows a two-dimensional section of *S*.

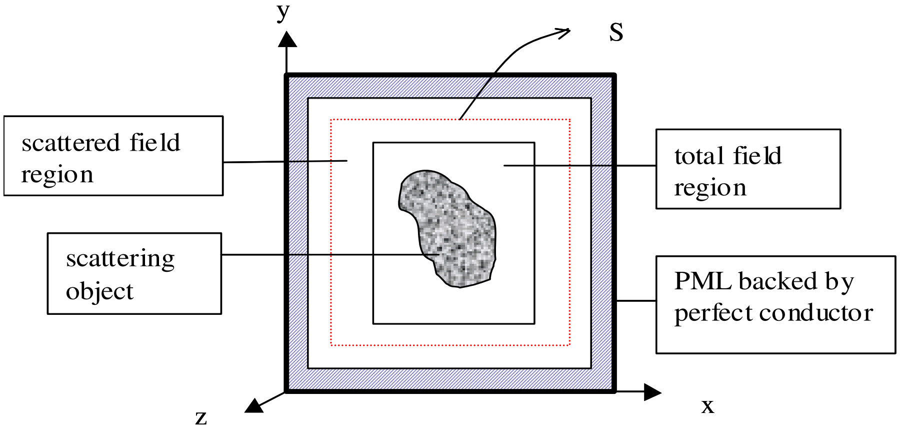

Figure 3.5: Near-field to far-field transformation (NFFFT) geometry.

The rectangular faces of the transformation surface are chosen to coincide with individual Yee cells, and each of the six faces is naturally subdivided into a rectangular array of patches by the faces of the Yee cells. The time-domain tangential field values on *S* are then converted to frequency-domain values using a running-sum implementation of Discrete Fourier Transform (DFT). The DFT is given by [42]

$$F(\omega) = \sum_{n} F^{n} \exp\left(-j\omega n\Delta t\right), \tag{3.36}$$

where $F^n$ denotes the tangential time-domain field component, either electric or magnetic, at time step *n*, and the summation is usually computed on-the-fly in step with the FDTD update equations. For a sinusoidal incident wave, the summation is computed only over the last period of the wave.

In the equations implementing the running-sum DFT, the tangential time-domain field values used are the field values at the center of each surface patch on each Yee cell on *S*. The tangential components of the electric field at the center of the patch are found from the average of the two nearest neighboring values, whereas the tangential components of the magnetic field at the center of the patch are found from the average of the four nearest neighboring values.

The next step is to define equivalent electric and magnetic surface current densities on *S* using Huygen's equivalence principle [59]. These equivalent current sources must be defined in such a way that the resulting fields outside *S* will be equal to the fields produced by the actual sources inside *S*. The electric surface current density is given by

$$\vec{J}_s = \hat{n} \times \vec{H}, \tag{3.37}$$

and the magnetic surface current density is given by

$$\bar{M}_s = -\hat{n} \times \bar{E}, \tag{3.38}$$

where $\hat{n}$ is the local unit vector normal to *S*. The far fields can then be calculated using these current sources as described below.

Let us specify the origin of the far field transform to be the center of the scattering structure. The spatial Fourier Transforms of the current densities $J_x$ and $M_y$ are calculated as [59]

$$\tilde{J}_x = \iiint_S J_x \exp\left[ j\left(k_x x' + k_y y' + k_z z'\right)\right] dx'dy'dz', \tag{3.39}$$

$$\tilde{M}_y = \iiint_S M_y \exp\left[ j\left(k_x x' + k_y y' + k_z z'\right)\right] dx'dy'dz', \tag{3.40}$$

where $k_x$=k sinθ cosϕ, $k_y$=k sinθ sinϕ, $k_z$=k cosθ, and k=ω√(εμ). Similar equations exist for $\tilde{J}_y, \tilde{J}_z, \tilde{M}_x, \tilde{M}_z$.

The far field components $E_\theta$, $E_\phi$, $H_\theta$, $H_\phi$ are then given by [59]

$$\begin{aligned} E_\theta = &-jk\eta\left(\frac{e^{-jkr}}{4\pi r}\right)\left[\cos\theta\cos\phi\tilde{J}_x + \cos\theta\sin\phi\tilde{J}_y - \sin\theta\tilde{J}_z\right] \\ &- jk\left(\frac{e^{-jkr}}{4\pi r}\right)\left[-\sin\phi\tilde{M}_x + \cos\phi\tilde{M}_y\right], \end{aligned} \tag{3.41}$$

$$E_\phi = -jk\eta\left(\frac{e^{-jkr}}{4\pi r}\right)\left[-\sin\phi\tilde{J}_x + \cos\phi\tilde{J}_y\right]$$
$$- jk\left(\frac{e^{-jkr}}{4\pi r}\right)\left[-\cos\theta\cos\phi\tilde{M}_x - \cos\theta\sin\phi\tilde{M}_y + \sin\theta\tilde{M}_z\right], \tag{3.42}$$

$$H_\theta = -\frac{E_\phi}{\eta} = jk\left(\frac{e^{-jkr}}{4\pi r}\right)\left[-\sin\phi\tilde{J}_x + \cos\phi\tilde{J}_y\right]$$
$$- j\frac{k}{\eta}\left(\frac{e^{-jkr}}{4\pi r}\right)\left[\cos\theta\cos\phi\tilde{M}_x + \cos\theta\sin\phi\tilde{M}_y + \sin\theta\tilde{M}_z\right], \tag{3.43}$$

$$H_\phi = \frac{E_\theta}{\eta} = jk\left(\frac{e^{-jkr}}{4\pi r}\right)\left[-\cos\theta\cos\phi\tilde{J}_x - \cos\theta\sin\phi\tilde{J}_y + \sin\theta\tilde{J}_z\right]$$
$$- j\frac{k}{\eta}\left(\frac{e^{-jkr}}{4\pi r}\right)\left[-\sin\phi\tilde{M}_x + \cos\phi\tilde{M}_y\right]. \tag{3.44}$$

In Equations (3.41) through (3.44), $r$ denotes the radial distance of the far field point from the origin of the far field transform.

The scattering pattern $F_s(\theta,\phi)$ gives the scattered intensity in the far field as a function of the polar angle $\theta$ and the azimuthal angle $\phi$ such that for an incident wave traveling in the $z$ direction, $\theta$ is the scattering angle. The scattering pattern can be calculated from Equations (3.41) – (3.44) as

$$F_s(\theta,\phi) = \mathrm{Re}[\vec{E}\times\vec{H}^*] = \mathrm{Re}[E_\theta H_\phi^* - E_\phi H_\theta^*], \tag{3.45}$$

where $^*$ denotes the complex conjugate. Note that the field components in Equation (3.45) include the $r$ dependence, therefore $F_s$ can be considered to represent the distribution of scattered intensity at different angles at a specific point in the far field. The scattering phase function $\wp(\theta,\phi)$ is the normalized form of $F_s(\theta,\phi)$ such that its integral over the solid angle $\Omega$ is

$$\int \wp(\theta,\phi)\, d\Omega = 1. \tag{3.46}$$

All the parameters describing the scattering characteristics such as the scattering cross-section or the anisotropy factor can then be calculated using $F_s(\theta,\phi)$ or $\wp(\theta,\phi)$ [60, 61].

### 3.3 VERIFICATION OF THE IMPLEMENTED FDTD CODE

The FDTD-PML code used for the simulations presented in this dissertation has been implemented in C/C++. The Yee Algorithm and the total field/scattered field formulation have been validated by testing convergence of a sinusoidal waveform to the steady state in an empty computational domain. The results showed that a propagating incident wave was regenerated in the total field region, whereas the field values in the scattered field region were reduced to negligible values, which was the expected result for a computational domain that did not contain a scattering structure. Details about these verification tests and other validation procedures involving observation of scattered field components at the PML interface have been previously described [62].

The ultimate verification of the implemented code has been carried out by computing the far field scattering patterns of homogeneous spheres and comparing the results to Mie theory. Figures 3.6 and 3.7 show the scattering patterns of four homogeneous spheres for an incident plane wave with a vacuum wavelength of $\lambda$=1 μm. The spheres have a refractive index of 1.02 relative to the outside medium, and the diameters are 1 μm, 3 μm, 5 μm, and 10 μm. These parameters were specifically chosen to create approximate models for biologically relevant scatterers. The computational domain was surrounded by a 10-cell PML, and the FDTD grid spacing used in these simulations was $\delta=\lambda/20$. The time step $\Delta t$ was specified to be $\delta/(2c)$, where $c$ is the speed of light in vacuum, and the number of time steps used was 1000. The PML parameters were given by $R(0)=10^{-3}$ and g=1.3. The figures also show the scattering patterns obtained with a different boundary condition employed in the previous FDTD implementation by our group [63]. This boundary condition was based on Liao extrapolation. The FDTD results with Liao extrapolation were obtained for a grid spacing of $\delta=\lambda/20$ and a time step of $\delta/(2c)$, similar to the PML case. The scattering patterns shown in Figs. 3.6 and 3.7 were first averaged over the azimuthal angle so that they were functions of the scattering angle only. All results are normalized to the scattering intensity at $0^{o}$, and the angular resolution for the scattering angle is $1^{o}$.

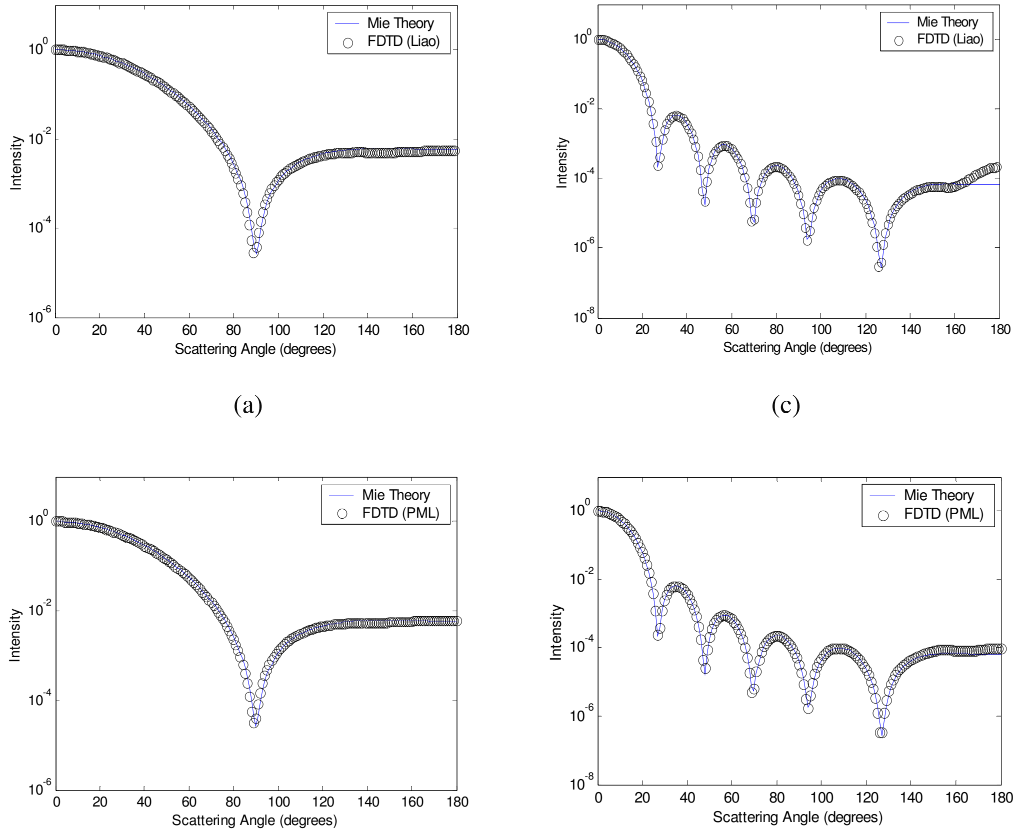

(a) (c)

(b) (d)

Figure 3.6: Comparison of FDTD results with Liao extrapolation and PML to Mie theory for (a, b) spheres with 1 μm diameter, and (c, d) spheres with 3 μm diameter. In all cases, the spheres have a refractive index of 1.02 relative to the outside medium. The scattering patterns are normalized to the scattering intensity at $0^{o}$.

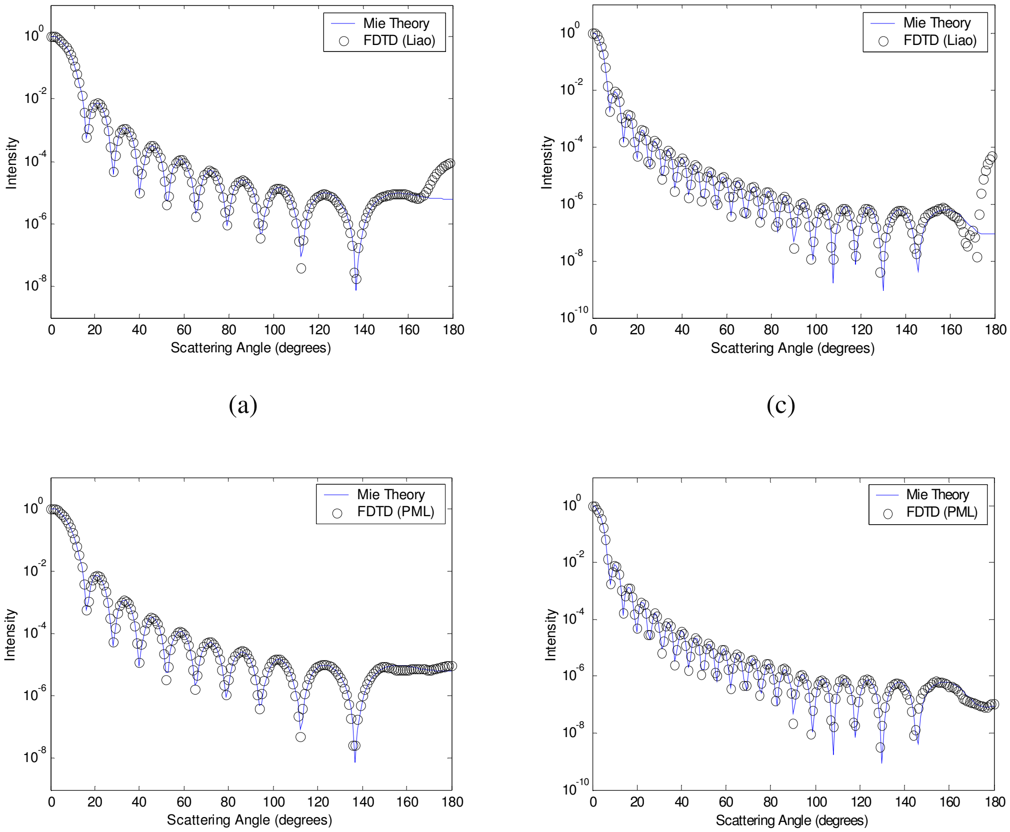

(a) (c)

(b) (d)

Figure 3.7: Comparison of FDTD results with Liao extrapolation and PML to Mie theory for (a, b) spheres with 5 μm diameter, and (c, d) spheres with 10 μm diameter. In all cases, the spheres have a refractive index of 1.02 relative to the outside medium. The scattering patterns are normalized to the scattering intensity at $0^{o}$.

Figure 3.6 shows that for the 1-μm sphere, the PML boundary condition and Liao extrapolation give comparable results. However, as the sphere size and the dynamic range of the simulation increase, the results obtained with Liao extrapolation do not agree with Mie theory for angles greater than $160^{o}$. This is especially evident in Fig. 3.7, which shows the scattering patterns of 5-μm and

10-μm spheres. The FDTD results with Liao extrapolation overestimate scattering at high angles, and the discrepancy can be up to three orders of magnitude as shown in Fig. 3.7(c). This is due to artificial reflections resulting from the instability of Liao extrapolation. These artificial reflections limit the accuracy of FDTD modeling, mainly for scattering angles close to $180^{o}$, where the scattering intensity is orders of magnitude smaller compared to the intensity of forward-scattered light and is thus more sensitive to numerical artifacts.

The scattering patterns obtained with PML, on the other hand, demonstrate excellent agreement with Mie theory at all angles for all of the spheres. The results in Figs. 3.7(b) and 3.7(d) show that there is actually a slight over-prediction of backscattering intensity for 5-μm and 10-μm spheres, but it should be pointed out that the PML boundary condition cannot eliminate artificial reflections completely. As described in *Section 3.2.3.3*, PML provides 'perfect matching' only in the continuous space, but some reflections can occur in the discrete-space representation of the FDTD method. The PML results, however, are consistently superior to those obtained with Liao extrapolation, indicating that the PML boundary condition is more effective in reducing artificial reflections to negligible levels. The maximum deviation from Mie theory for angles greater than $160^{o}$ occurs at $180^{o}$ for the 10-μm sphere, and this deviation is about 25%.

Another factor that can affect the results is the grid spacing used, since using a coarse FDTD grid can lead to staircasing errors. This is especially important in simulations involving perfect spheres, and finer grid spacing can be used to obtain better results. For the simulations described here, $\lambda/20$ represents a good balance between accuracy and computational requirements.

# Chapter 4: Model-Based Analysis of Spatially Resolved Reflectance Spectroscopy for Diagnosis of Cervical Pre-Cancer and Comparison to Clinical Measurements

## 4.1 INTRODUCTION

Numerous clinical studies present sound evidence that reflectance spectroscopy is sensitive to the morphological, structural, and biochemical changes associated with development of epithelial pre-cancer [1-12]. However, observed differences in reflectance spectra of normal and dysplastic tissue are not completely understood. Modeling studies are necessary to analyze the effect of dysplastic changes on the optical properties of epithelial tissues, and to provide a quantitative understanding of the specific contributions of each of the dysplastic changes to the overall spectral response.

Monte Carlo modeling provides the most flexible approach to study photon propagation in tissues. While analytical models generally put limitations on the tissue parameters and the source-detector geometry to be simulated [23, 25, 26], Monte Carlo based models can accurately describe photon propagation in multi-layered tissue geometries and can account for sophisticated fiber-optic probe designs used in *in vivo* clinical studies. Monte Carlo modeling has been widely employed to analyze tissue reflectance from a number of different organ sites [30, 31, 64, 65]. These studies have significant importance in understanding reflectance properties of tissues. For reflectance spectroscopy to be adopted as a tool for diagnosis of epithelial pre-cancer, however, there is a need for thorough analysis targeted towards establishing a connection between dysplastic changes leading to alterations in optical properties of different tissue layers and the resulting changes in reflectance signals.

Epithelial tissues, such as the intestine, oral cavity, and cervix, are generally described as two-layer media consisting of a thin epithelium on top of an underlying stroma. As described in *Chapter 1*, dysplastic changes in epithelial tissues include increased scattering from epithelial cells and increased absorption in the stroma. Increased scattering from epithelial cells is due to increased nuclear size, increased DNA content, and hyperchromasia with coarse and irregular chromatin clumping [13]. Increased absorption in the stroma arises from elevated hemoglobin concentration due to increased microvessel density and angiogenic activity in dysplastic tissue [18, 19]. Recent evidence suggests that dysplastic progression also leads to decreased scattering in the stroma [6, 9], possibly due to decomposition and reorganization of the collagen matrix [14-17]. Monte Carlo modeling can be used to investigate the influence of all of these changes on reflectance signals and to identify key features that can aid in interpretation of reflectance spectra with the ultimate goal of distinguishing normal and pre-cancerous tissues.

Another benefit of Monte Carlo modeling is the ability to assess the significance of acquiring spatially resolved reflectance spectra using multiple source-detector separations. It is known that as the distance between the source and the detector fiber is increased, sampling depth of detected photons increases [32, 35, 66]. Therefore, spatially resolved reflectance spectroscopy can be used to sample different depths in epithelial tissues [10, 67-70]. Analysis of the spectral response and the sampling depth characteristics of different source-detector fiber pairs can provide a guideline for selection of diagnostically significant source-detector separations.

Recently, there have been many attempts to develop mathematical or computational models that enable inverse estimation of optical parameters from *in vivo* fluorescence and/or reflectance measurements [3, 20, 71-75]. A basic premise of these studies is that direct information about diagnostically relevant optical parameters will result in more effective classification algorithms. Progress in this respect is only possible through investigation and identification of differences in spectral characteristics of normal and pre-cancerous tissues within the framework of a forward modeling scheme. Such an approach based on Monte Carlo simulations is likely to facilitate development of inverse models and help devise inverse estimation strategies.

The goal of the research described in this chapter is to develop a forward model that provides a quantitative understanding of the differences observed in spatially resolved reflectance spectra of normal and dysplastic cervical tissue. Our group has collected a significant amount of clinical reflectance data as part of a large diagnostic trial of *in vivo* fluorescence and reflectance spectroscopy for cervical pre-cancer detection. I have used the Monte Carlo implementation described in *Chapter 2* to simulate the clinical fiber-optic probe that acquires reflectance measurements at six different source-detector separations. Simulations have been carried out to analyze the sensitivity of spectral measurements to various possible dysplastic changes in epithelial and stromal optical properties, and to predict reflectance spectra of normal and dysplastic cervical tissue for different source-detector separations. Predictions from the simulations are compared to spectra measured *in vivo* from patients in different diagnostic categories. Monte Carlo simulation results and the clinical measurements available provide a basis to establish trends for spectral changes that accompany dysplastic progression. Penetration depth statistics of photons detected at the six source-detector separations are also presented to reveal the sampling depth profile of the clinical fiber-optic probe.

## 4.2 METHODS

### 4.2.1 Clinical Measurements of Reflectance Spectra from Cervical Tissue

Clinical reflectance spectroscopy data available have been collected over the past several years at The University of Texas M. D. Anderson Cancer Center (Houston, Texas), Lyndon B. Johnson Hospital (Houston, Texas), and the British Columbia Cancer Agency (Vancouver, Canada) as part of a large ongoing diagnostic trial of *in vivo* fluorescence and reflectance spectroscopy for cervical pre-cancer detection. Reflectance measurements presented in this chapter represent the subset of data obtained at the British Columbia Cancer Agency. The fiber-optic probe used in this clinic had a 5 mm outer diameter, and reflectance spectra were obtained at six different source-detector separations. A schematic diagram of the tip of the probe is shown in Fig. 4.1.

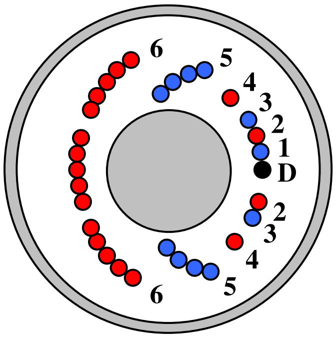

Figure 4.1: Schematic diagram of the tip of the fiber-optic probe used to acquire clinical measurements presented in this chapter. The central portion of the probe was used for fluorescence measurements, whereas the fibers shown were used to obtain spatially resolved reflectance spectra. In the figure, *D* is the detector fiber, and the labels 1-6 represent different sets of source fibers located at specified distances from the detector fiber.

The central portion of the probe was utilized for fluorescence excitation and collection. The fibers shown in Fig. 4.1 were used to acquire spatially resolved reflectance spectra. All of the fibers had a 200 µm diameter and a numerical aperture of 0.22. In Fig. 4.1, *D* indicates the detector fiber, and the fibers labeled 1-6 represent the source fibers delivering broadband excitation light from a xenon lamp. The labels 1-6 are used to distinguish the source fibers belonging to different groups corresponding to six different source-detector separations. The source-detector geometry is detailed in Table 4.1, which lists the center-to-center source-detector separations and the total number of source fibers present for each source-detector separation.

Table 4.1: Source-detector geometry used to acquire spatially resolved reflectance spectra from cervical tissue.

| Fiber group | Source-Detector Separation (mm) | Number of Source Fibers |
|---|---|---|
| 1 | 0.25 | 1 |
| 2 | 0.50 | 2 |
| 3 | 0.75 | 2 |
| 4 | 1.10 | 2 |
| 5 | 2.10 | 8 |
| 6 | 3.00 | 15 |

Note that the number of source fibers increases with increasing source-detector separation. Since reflectance signals are expected to be lower for large source-detector separations, using a larger number of source fibers allows satisfactory signal to noise ratios to be obtained. As part of pre-processing, spectra measured from cervical tissue sites were normalized by standard spectra measured from an integrating sphere made out of spectralon. This normalization corrected for the wavelength dependent response of the optical system and scaled the tissue measurements to factor out the number of source fibers.

Tissue spectra for each of the six source-detector separations consisted of 113 intensity measurements corresponding to wavelengths from 370 nm to 650 nm with 2.5 nm increments. Following spectroscopic measurements, cervical tissue sites were biopsied and submitted for histopathologic analysis. A group of pathologists classified the biopsied sites into different diagnostic categories including normal (negative for dysplasia), atypia, human papilloma virus (HPV) associated changes, CIN (cervical intraepithelial neoplasia), and CIS (carcinoma *in situ*). The CIN biopsies were further subclassified as CIN 1 (mild dysplasia), CIN 2 (moderate dysplasia), and CIN 3 (severe dysplasia). Since the main focus of the research described in this chapter is to analyze reflectance spectra of normal and highly dysplastic cervical tissue, the clinical data set presented hereafter consists solely of reflectance measurements obtained from sites that were classified as normal, CIN 3, or CIS.

### 4.2.2 Input for Monte Carlo Modeling

Monte Carlo simulations have been carried out for every 20 nm between 360 nm and 640 nm. These fifteen wavelengths were sufficient to provide a reasonable characterization of spectral reflectance. Each simulation has been performed using $10^8$ photons.

#### *4.2.2.1 Tissue Parameters*

Cervical tissue was considered to be a two-layer medium with the epithelium on the top and the stroma underneath. The thickness of the normal cervical squamous epithelium was assumed to be 300 µm [76], and the stroma was modeled as a semi-infinite medium. Use of realistic and relevant optical properties is a crucial part of modeling. The values used in this paper to model normal cervical tissue have been collected from various sources. These were mostly based on measurements from cervical tissue or other tissues having a similar architecture. Epithelial scattering coefficients were obtained from confocal measurements of *ex vivo* cervical tissue samples [77]. Epithelial absorption coefficients and stromal scattering coefficients were based on a study by Qu et al.

[78] reporting integrating sphere measurements of bronchial tissue. Absorption in the stroma can be attributed to hemoglobin and collagen. Absorption coefficients of both of these components were calculated separately and summed to characterize stromal absorption. Hemoglobin absorption coefficients were computed using the extinction coefficients compiled by Prahl [79]. Hemoglobin oxygen saturation was assumed to be 60% [3, 30, 31, 80], and the volume fraction of the blood in the stroma was estimated to be 0.3% [3, 31, 80, 81]. Collagen absorption coefficients were based on results reported for bloodless skin samples [81]. Figure 4.2 shows the scattering and absorption coefficients used in this chapter to model squamous normal cervical tissue. The wavelength resolution in the plots is 20 nm.

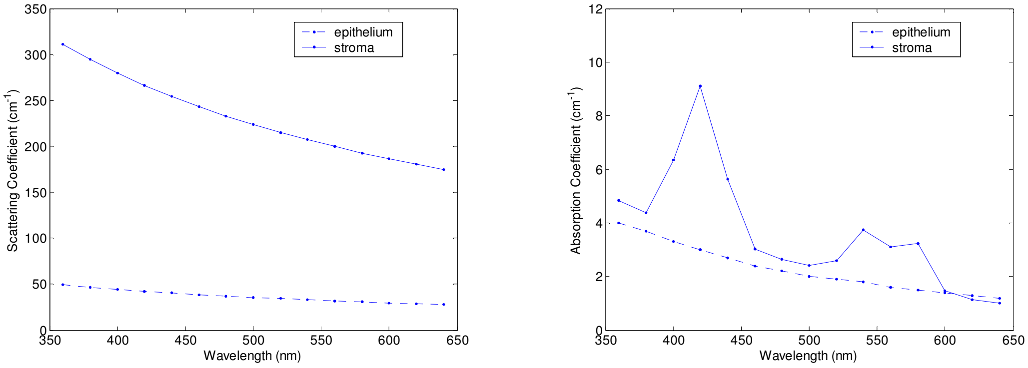

(a) (b)

Figure 4.2: (a) Scattering, and (b) absorption coefficients for squamous normal cervical tissue.

In the simulations, the refractive indices of both the epithelium and the stroma were set to 1.4. The epithelial anisotropy factor was assigned a value of

0.95, and the stromal anisotropy factor was assumed to be 0.88, independent of wavelength [29].

In modeling epithelial pre-cancer, I only considered changes in epithelial scattering coefficient, stromal absorption coefficient, and stromal scattering coefficient. Increase in epithelial scattering coefficient for highly dysplastic cervical tissue has been reported by Collier et al. [77]. Increase in stromal absorption coefficient is also expected since angiogenesis associated with progression of dysplasia has been well documented [18, 19]. It has also been reported that collagen matrix in the stroma degrades with progression of dysplasia [14-17], and degradation of collagen matrix may lead to a decrease in stromal scattering coefficient [6, 9]. Therefore, the main focus of the modeling studies presented in this chapter was on assessing the contribution of alterations in these three optical parameters to dysplasia associated changes in spectral response. The epithelial absorption coefficient, the refractive indices and the anisotropy factors were kept the same as in the case of normal tissue. Epithelial thickness for dysplastic tissue was again assumed to be 300 μm [76].

#### *4.2.2.2 Fiber-Optic Probe Parameters*

Fiber parameters were selected to match the geometry of the clinical fiber-optic probe and to simulate the six source-detector separations given in Table 4.1. The refractive indices of both the source and the detector fibers were set to 1.5. I also assumed that the material in between the fiber tips was highly absorptive to prevent any internal reflection off the probe surface.

### 4.2.3 Output from Monte Carlo Modeling

The output of each simulation includes detected reflectance intensity for each of the six source-detector separations. Three simulations have been carried out for each set of optical properties considered, and the spectra presented for each source-detector separation correspond to the averages over three simulations. To make the computed spectra appear smoother and more continuous, intensities at the fifteen wavelengths simulated have been interpolated in Matlab using piecewise cubic Hermite polynomials, increasing the wavelength resolution of the spectral Monte Carlo modeling plots to 2.5 nm.

Penetration depths of all the photons collected at each source-detector separation have also been recorded during the Monte Carlo simulations. Note that penetration depth as used here is defined to be the maximum depth in tissue at which a photon undergoes a scattering event. Mean penetration depth corresponds to the penetration depth averaged over all detected photons, and analysis of this parameter as a function of wavelength can provide a better understanding of the differences in reflectance spectra for different source-detector separations and can reveal the sampling depth characteristics of different source-detector fiber pairs.

## 4.3 RESULTS

### 4.3.1 Sensitivity of Spectral Reflectance to Possible Dysplastic Changes

As an initial step to better understand the spectral changes associated with pre-cancer progression, each of the dysplastic changes first needs to be considered separately. The following subsections present Monte Carlo modeling results that demonstrate the sensitivity of spectral reflectance to increased epithelial scattering, increased stromal absorption, and decreased stromal scattering.

### *4.3.1.1 Epithelial Scattering*

Figure 4.3 shows the effect of varying the epithelial scattering coefficient, $\mu_{s,epithelium}$, on reflectance spectra for the six different source-detector separations. The blue spectra correspond to the results obtained with the base optical properties shown in Fig. 4.2. The solid black spectra have been obtained by increasing $\mu_{s,epithelium}$ by a factor of two, and the dashed black spectra have been obtained by increasing $\mu_{s,epithelium}$ by a factor of three. All the other optical parameters were held constant. For each source-detector separation, the base spectrum designated as normal has been normalized such that the reflectance intensity at 640 nm equals one. The same scaling factor has been applied to the other two spectra shown in each plot. Simulation results show that the difference in intensity levels for the smallest and the largest source-detector separation is about two orders of magnitude. Note, however, that the normalization scheme described allows all the spectra to be plotted on the same scale and enables direct comparison of spectral shapes for different source-detector separations.

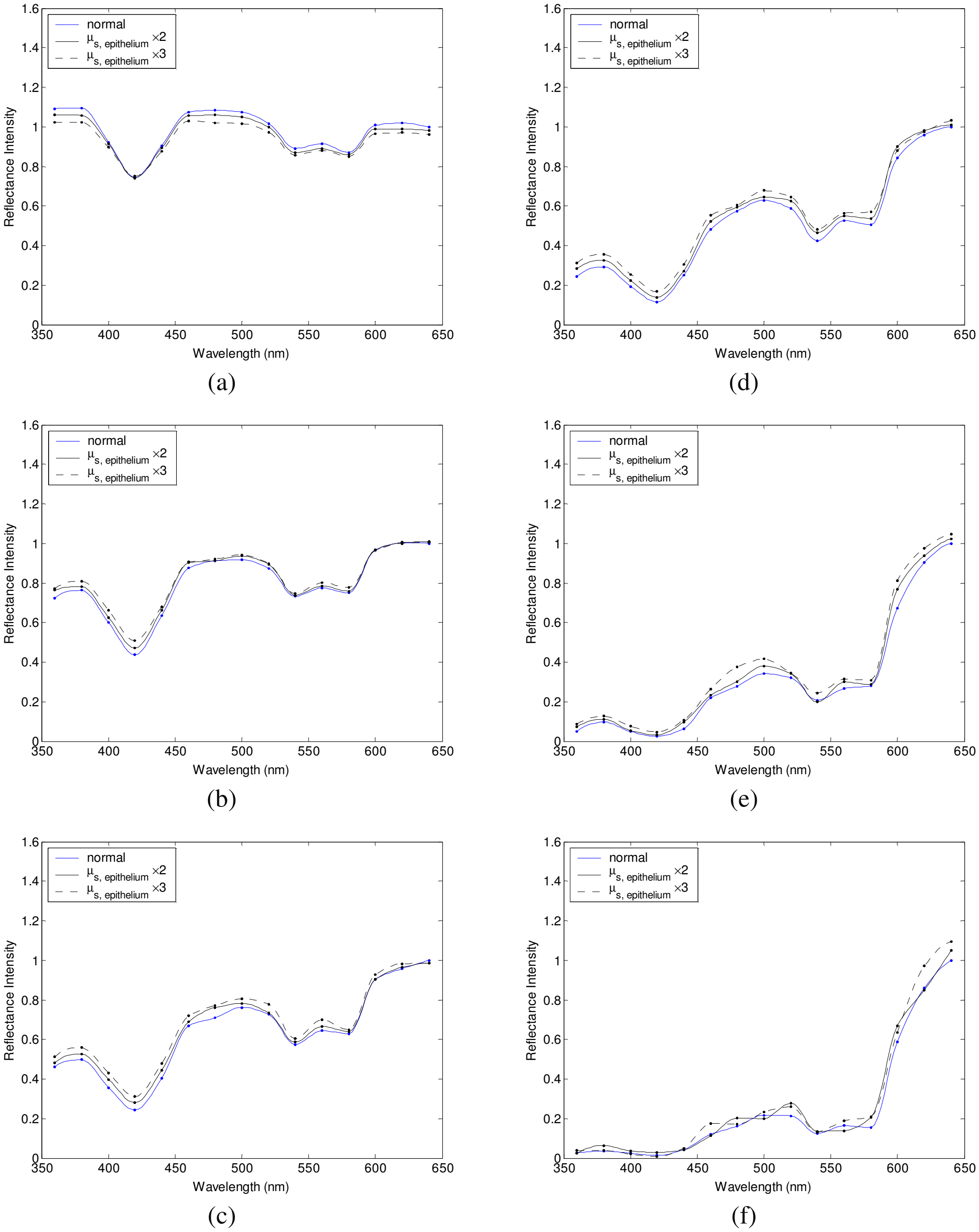

(a) (d) (b) (e) (c) (f)

Figure 4.3: Sensitivity of spectral reflectance to epithelial scattering coefficient at a source-detector separation of (a) 0.25 mm, (b) 0.50 mm, (c) 0.75 mm, (d) 1.10 mm, (e) 2.10 mm, and (f) 3.00 mm.

The spectra in Fig. 4.3 illustrate typical characteristics associated with tissue reflectance. The valleys in the spectra due to hemoglobin absorption maxima at around 420 nm, 540 nm, and 580 nm are evident for all source-detector separations, and these valleys tend to widen as the source-detector separation is increased. Note also that the spectra for smaller source-detector separations are flatter, whereas the relative rate of wavelength dependent increase in reflectance intensity is higher for larger source-detector separations.

The results in Fig. 4.3 demonstrate that changing the epithelial scattering coefficient does not have a significant effect on either the reflectance intensity or the spectral shape for any of the source-detector separations. For the smallest source-detector separation that represents the case where the source fiber and the detector fiber are placed next to each other, increasing $\mu_{s,epithelium}$ results in a slight decrease in reflectance intensity [Fig. 4.3(a)]. For the other five source-detector separations, increasing $\mu_{s,epithelium}$ leads to a slight increase in reflectance intensity [Fig. 4.3(b)-(f)].

#### *4.3.1.2 Stromal Absorption*

Figure 4.4 shows the effect of varying the stromal absorption coefficient, $\mu_{a,stroma}$, on reflectance spectra for the six different source-detector separations. As in Fig. 4.3, the blue spectra correspond to the results obtained with the base optical properties. The solid black spectra and the dashed black spectra have been obtained by increasing $\mu_{a,stroma}$ by a factor of two and three, respectively, while keeping all the other parameters constant. These results have also been normalized such that the reflectance intensity at 640 nm equals one for the base case.

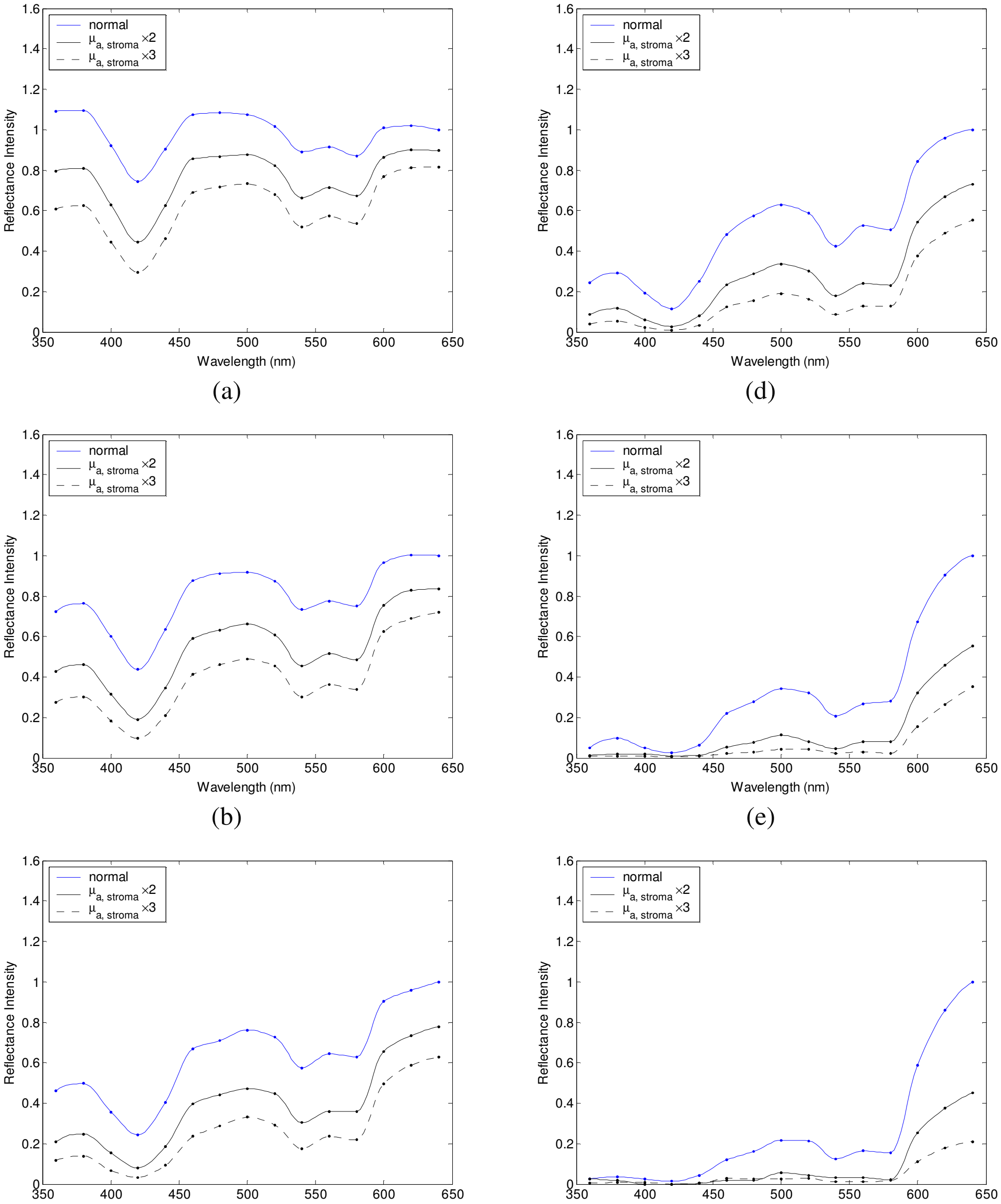

(a)

(b)

(c)

(d)

(e)

(f)

Figure 4.4: Sensitivity of spectral reflectance to stromal absorption coefficient at a source-detector separation of (a) 0.25 mm, (b) 0.50 mm, (c) 0.75 mm, (d) 1.10 mm, (e) 2.10 mm, and (f) 3.00 mm.

Figure 4.4 shows that increasing $\mu_{a,stroma}$ significantly decreases the reflectance intensity for all source-detector separations. Increasing the stromal absorption coefficient also results in broadening of the hemoglobin absorption valleys, which is particularly evident for source-detector separations of 0.50 mm, 0.75 mm, 1.10 mm, and 2.10 mm [Fig. 4.4(b)-(e)]. Note that for the source-detector separation of 3.00 mm [Fig. 4.4(f)], increasing $\mu_{a,stroma}$ almost entirely flattens out spectral features associated with hemoglobin absorption.

### *4.3.1.3 Stromal Scattering*

The effect of varying the stromal scattering coefficient, $\mu_{s,stroma}$, is shown in Fig. 4.5. The solid black spectra have been obtained by decreasing $\mu_{s,stroma}$ by 25% relative to that used for the blue spectra, and the dashed black spectra have been obtained by decreasing $\mu_{s,stroma}$ by 50%. All the other optical parameters were held constant. The results have been normalized using the same scheme described for Figs. 4.3 and 4.4.

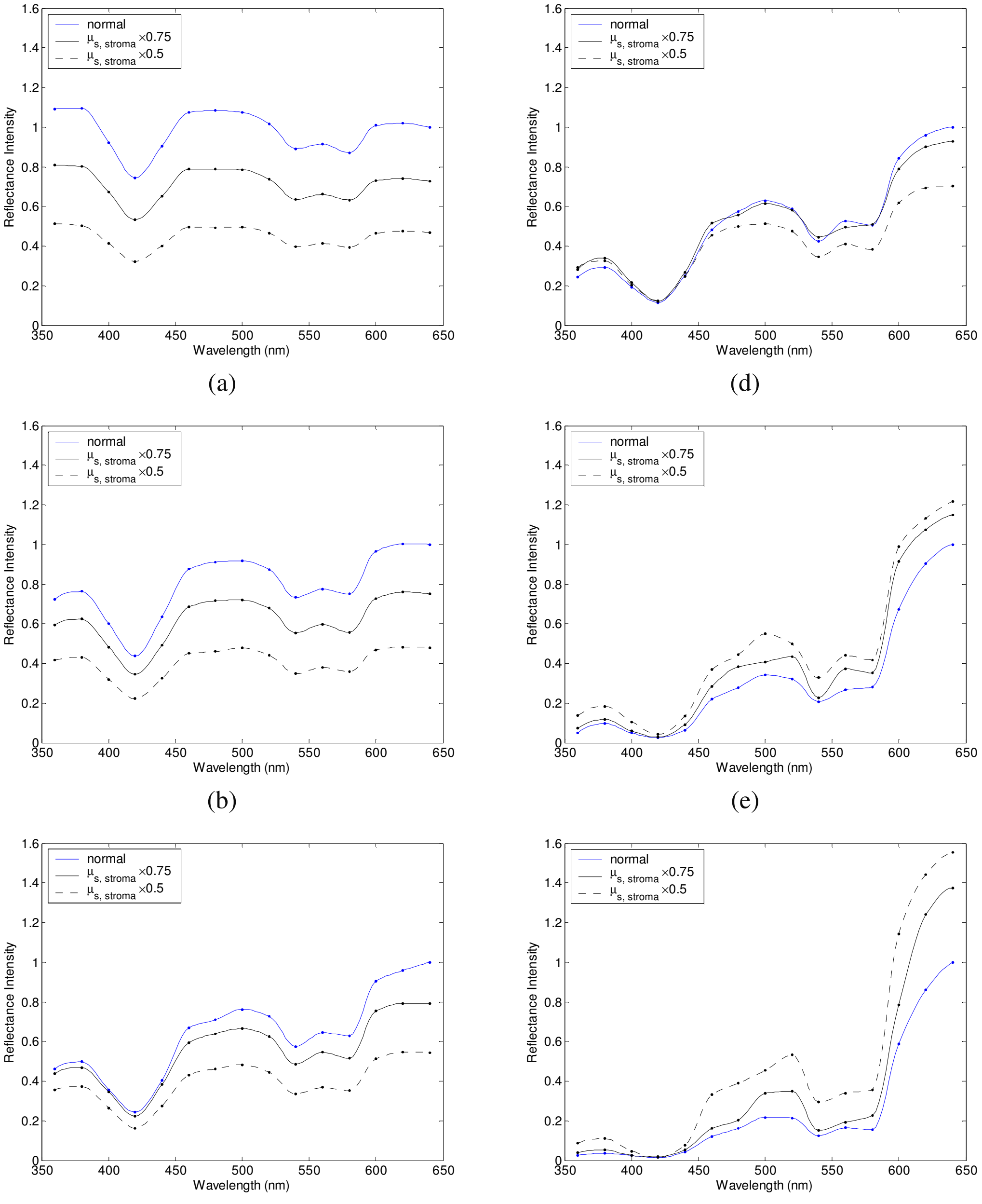

(a) (d)

(b) (e)

(c) (f)

Figure 4.5: Sensitivity of spectral reflectance to stromal scattering coefficient at a source-detector separation of (a) 0.25 mm, (b) 0.50 mm, (c) 0.75 mm, (d) 1.10 mm, (e) 2.10 mm, and (f) 3.00 mm.

Results in Fig. 4.5 illustrate that changing the stromal scattering coefficient has considerable influence on spectral profiles. Decreasing $\mu_{s,stroma}$ decreases the reflectance intensity and flattens out the spectra for the four smallest source-detector separations [Fig. 4.5(a)-(d)], with 1.10 mm separation being least sensitive to changes in $\mu_{s,stroma}$ [Fig. 4.5(d)]. Interestingly, the trend reverses for source-detector separations greater than 1.10 mm, and decreasing $\mu_{s,stroma}$ actually increases the reflectance intensity for the two largest source-detector separations [Fig. 4.5(e)-(f)]. In these cases, decreasing $\mu_{s,stroma}$ increases the relative rate of wavelength dependent increase in reflectance intensity and reduces the width of the hemoglobin absorption valleys.

### 4.3.2 Predictions for Spectral Reflectance of Dysplastic Cervical Tissue

To predict spectral changes associated with dysplastic progression, we need to consider the effects of increased epithelial scattering, increased stromal absorption, and decreased stromal scattering simultaneously. Measurements by Collier et al. [77] using confocal microscopy indicate that there is a three-fold increase in epithelial scattering coefficient in highly dysplastic cervical tissue compared to normal tissue. It has been shown that the microvessel density in the stroma increases by approximately a factor of two in the case of severe cervical dysplasia [18, 19]. Therefore, in modeling reflectance spectra for dysplastic cervical tissue, I increased the epithelial scattering coefficient, $\mu_{s,epithelium}$, by a factor of three and the stromal absorption coefficient, $\mu_{a,stroma}$, by a factor of two. Since there is no quantitative information about changes in stromal scattering, three different cases have been considered. In the first case, the stromal scattering coefficient, $\mu_{s,stroma}$, was kept the same as in normal tissue. In the second case, $\mu_{s,stroma}$ was decreased by 25% compared to the normal tissue, and in the third case, $\mu_{s,stroma}$ was decreased by 50%. Figure 4.6 shows the simulation results corresponding to different combinations of optical properties. The blue spectra represent the results for normal tissue, and the remaining three spectra represent the results corresponding to different stromal scattering coefficients. For each source-detector separation, the spectrum for normal tissue has been normalized such that the reflectance intensity at 640 nm equals one. The same scaling factor has been applied to the other spectra shown in each plot.

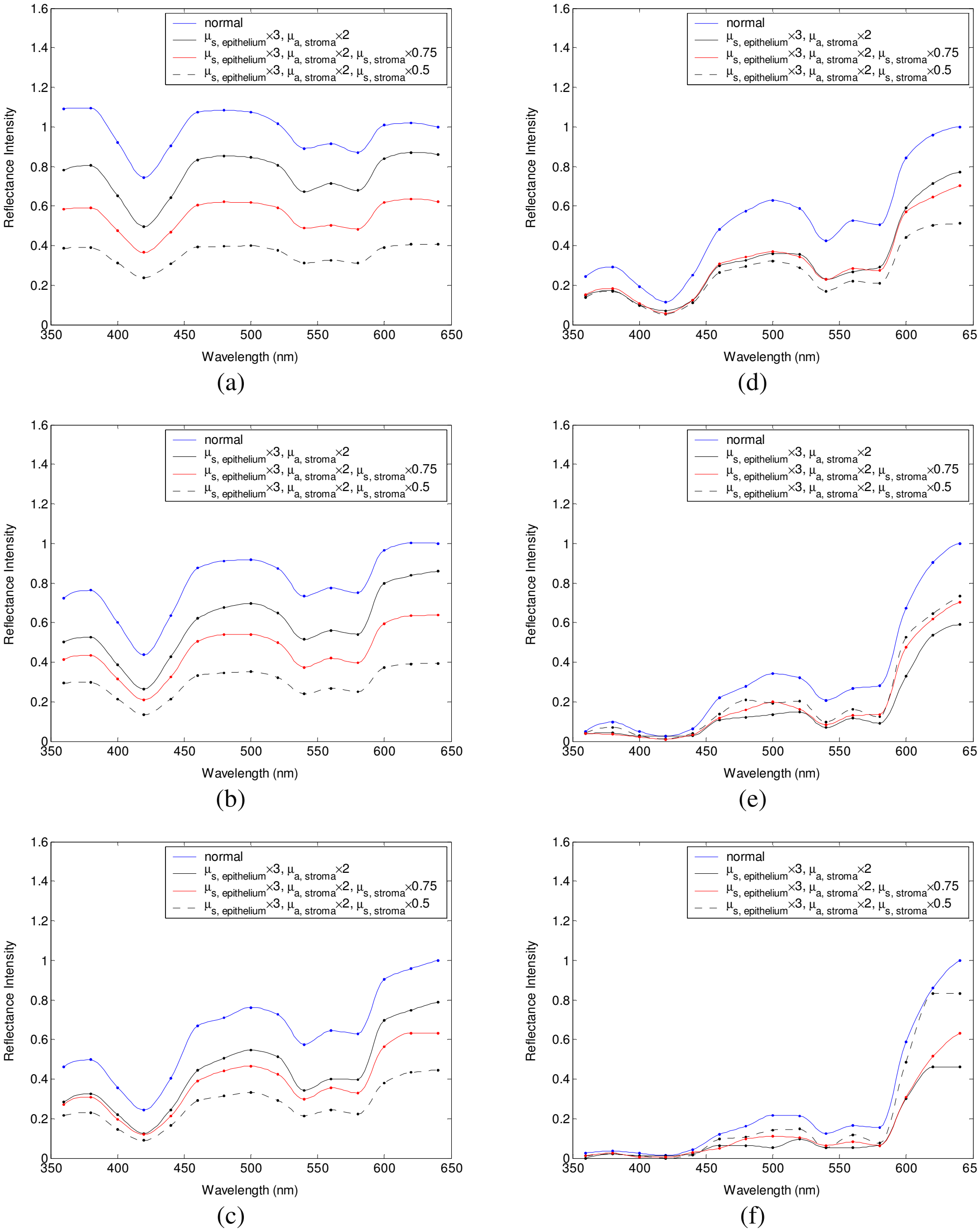

(a) (d)

(b) (e)

(c) (f)

Figure 4.6: Model predictions for spectral reflectance of dysplastic cervical tissue at a source-detector separation of (a) 0.25 mm, (b) 0.50 mm, (c) 0.75 mm, (d) 1.10 mm, (e) 2.10 mm, and (f) 3.00 mm.

The results shown in Fig. 4.6 illustrate that decreasing $\mu_{s,stroma}$ in addition to other dysplastic changes simulated decreases the reflectance intensity for the first four source-detector separations [Fig. 4.6(a)-(d)]. For the remaining two source-detector separations, decreasing $\mu_{s,stroma}$ increases the reflectance intensity. These results are consistent with those presented in Fig. 4.5.

### 4.3.3 Comparison of Monte Carlo Modeling Results to Clinical Measurements

The clinical data set available consisted of reflectance spectra measured *in vivo* from 176 cervical tissue sites in 136 patients. The mean age of the patients was 35 with a standard deviation of 10. Table 4.2 shows the breakdown of measurements according to histopathologic diagnosis as well as age. The high-grade dysplasia category involves sites that were classified as CIN 3 or CIS.

Table 4.2: Description of the clinical data set used for comparison to Monte Carlo simulation results.

| Diagnostic Category | Number of Patients | Number of Sites |
|---|---|---|
| Squamous normal | | |
| Age>35 | 50 | 60 |
| Age<=35 | 65 | 69 |
| High-grade dysplasia | | |
| Age>35 | 10 | 11 |
| Age<=35 | 32 | 36 |

Figure 4.7 shows the averaged reflectance spectra for the two diagnostic categories. Two different age groups are plotted separately to illustrate any age-related differences in reflectance measurements, as have been observed in autofluorescence measurements [29, 82]. For each source-detector separation, the averaged spectrum corresponding to normal tissue sites obtained from patients older than 35 has been normalized such that the reflectance intensity at 640 nm equals one. The same scaling factor has been applied to the remaining three averaged spectra. The figure also shows the standard deviations corresponding to the averages for each group.

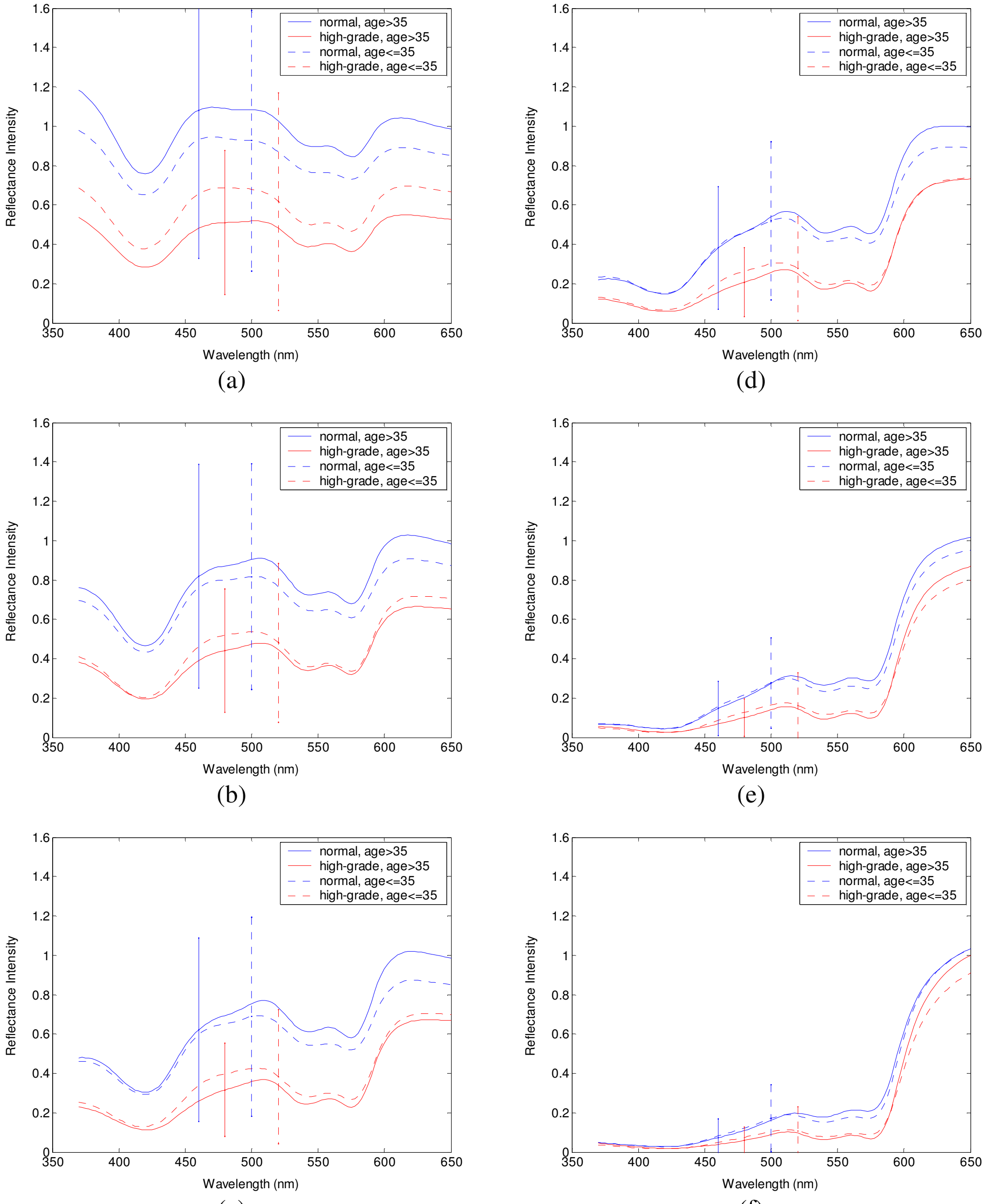

(a) (d)

(b) (e)

(c) (f)

Figure 4.7: Averaged clinical reflectance spectra for different diagnostic categories at a source-detector separation of (a) 0.25 mm, (b) 0.50 mm, (c) 0.75 mm, (d) 1.10 mm, (e) 2.10 mm, and (f) 3.00 mm.

The averaged clinical reflectance spectra shown in Fig. 4.7 indicate that high-grade dysplasia leads to an overall decrease in reflectance intensity for all source-detector separations. The hemoglobin absorption valleys at around 420 nm, 540 nm, and 580 nm tend to be broader for the case of high-grade dysplasia. Age-related differences are most pronounced for the smallest source-detector separation [Fig. 4.7(a)]. The relative intensity differences between normal and highly dysplastic tissue sites tend to be larger for patients older than 35. For patients 35 years old or younger, the intensity differences are smaller. Note that as the source-detector separation increases, age-related differences in the averaged spectra diminish. Figure 4.7 also demonstrates that there can be extensive variability in the measured reflectance spectra, as evidenced by the large standard deviations characterizing the averages.

Figure 4.8 compares the averaged clinical reflectance spectra for different diagnostic categories to predictions from Monte Carlo simulations. In comparing clinical measurements to model predictions, I combined the two age groups and computed the averages for normal and highly dysplastic sites over the entire data set. Visual inspection of these averages and model predictions from Fig. 4.6 revealed that the simulation results that best matched the dysplastic changes observed in averaged clinical data corresponded to the case with $\mu_{s,epithelium}\times3$, $\mu_{a,stroma}\times2$, and $\mu_{s,stroma}\times0.75$. Therefore, the modeled spectra shown in Fig. 4.8 for high-grade dysplasia represent this particular case. For each source-detector separation, the modeled spectrum for normal tissue has been normalized such that the reflectance intensity at 640 nm equals one. The same scaling factor has been used to normalize the modeled spectrum for highly dysplastic tissue. A similar normalization scheme has been applied to the averaged clinical data, enabling comparison of modeled and measured spectra on the same scale. Also shown in Fig. 4.8 are the standard deviations of Monte Carlo modeling results over three different simulations. These standard deviations provide some insight into the variability of simulation results and are included for only three wavelengths to maintain clarity of the plots.

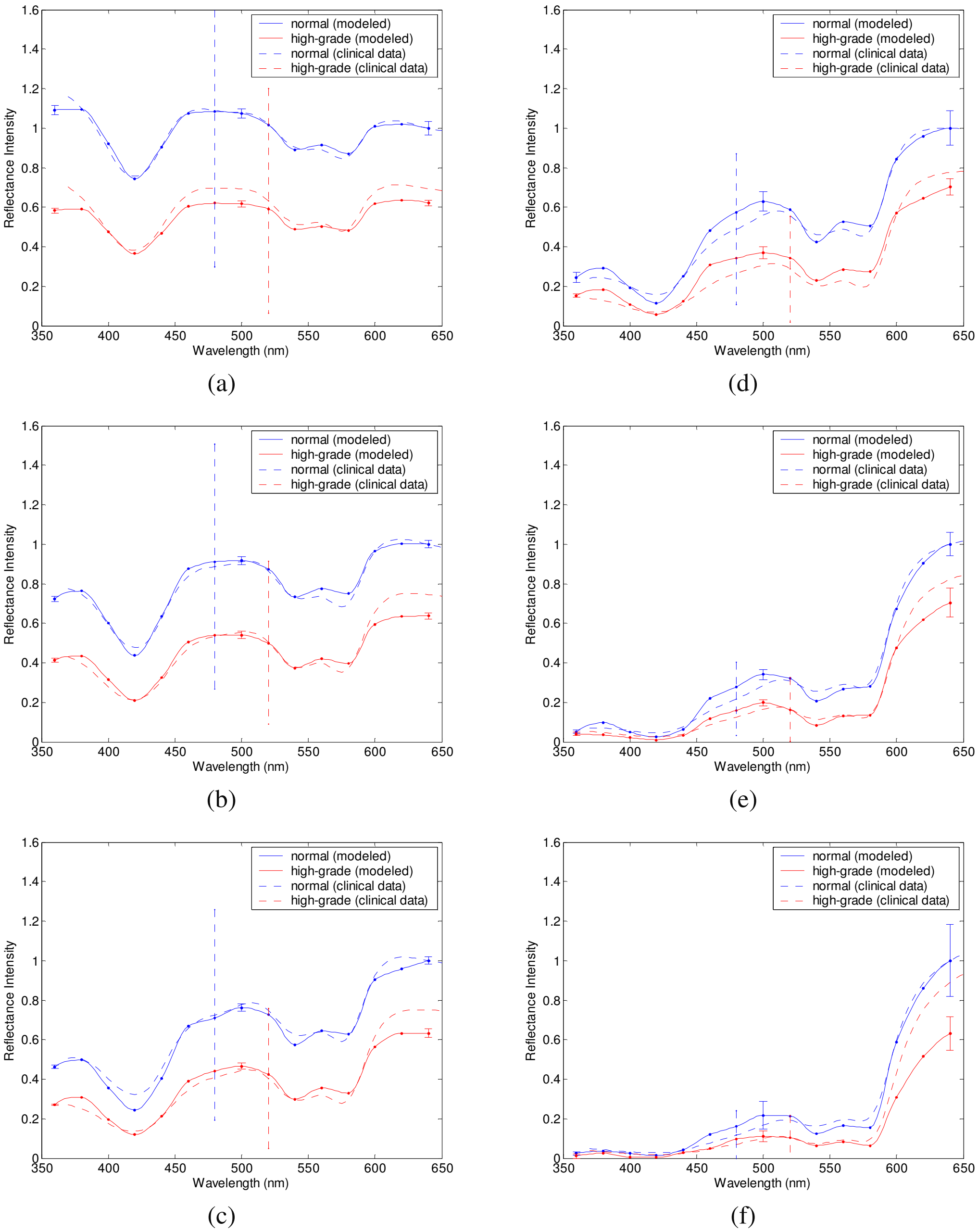

(a) (d)

(b) (e)

(c) (f)

Figure 4.8: Comparison of averaged clinical reflectance spectra to model predictions at a source-detector separation of (a) 0.25 mm, (b) 0.50 mm, (c) 0.75 mm, (d) 1.10 mm, (e) 2.10 mm, and (f) 3.00 mm.

Figure 4.8 shows that there is extremely good agreement between modeled and measured reflectance spectra for all source-detector separations. We can conclude that the base optical properties from Fig. 4.2 that have been used to model squamous normal tissue can adequately reproduce spectral features observed in clinical measurements. The modeled spectra accurately predict the relative rate of wavelength dependent increase in reflectance intensity for different source-detector separations. It is also evident in Fig. 4.8 that increasing the epithelial scattering coefficient by a factor of three, increasing the stromal absorption coefficient by a factor of two, and decreasing the stromal scattering coefficient by 25% can very well describe the average dysplastic changes observed in clinical data. Simulation results based on these assumptions can accurately predict the relative decrease in reflectance intensity for dysplastic tissue sites. Broadening of hemoglobin absorption valleys in spectra measured from highly dysplastic tissue sites is also well captured in the modeled spectra. The most significant intensity discrepancies between averaged clinical measurements and modeling results for dysplastic tissue tend to occur for wavelengths greater than 600 nm, especially for the largest source-detector separation [Fig. 4.8(f)]. Note that for large source-detector separations, there is increased variability in Monte Carlo modeling results, which is evidenced by large standard deviations. This is due to the fact that the relative number of detected photons is smaller for larger source-detector separations.

### 4.3.4 Analysis of Depth Sensitivity

Figure 4.9 shows the mean penetration depths computed for two sets of optical properties. The first set corresponds to the optical properties for normal tissue, and the second set corresponds to the case with $\mu_{s,epithelium}\times 3$, $\mu_{a,stroma}\times 2$, and $\mu_{s,stroma}\times 0.5$. These two particular sets were chosen since they represent the two extreme cases presented in Fig. 4.6. The standard deviations over three different simulation results are shown for three wavelengths.

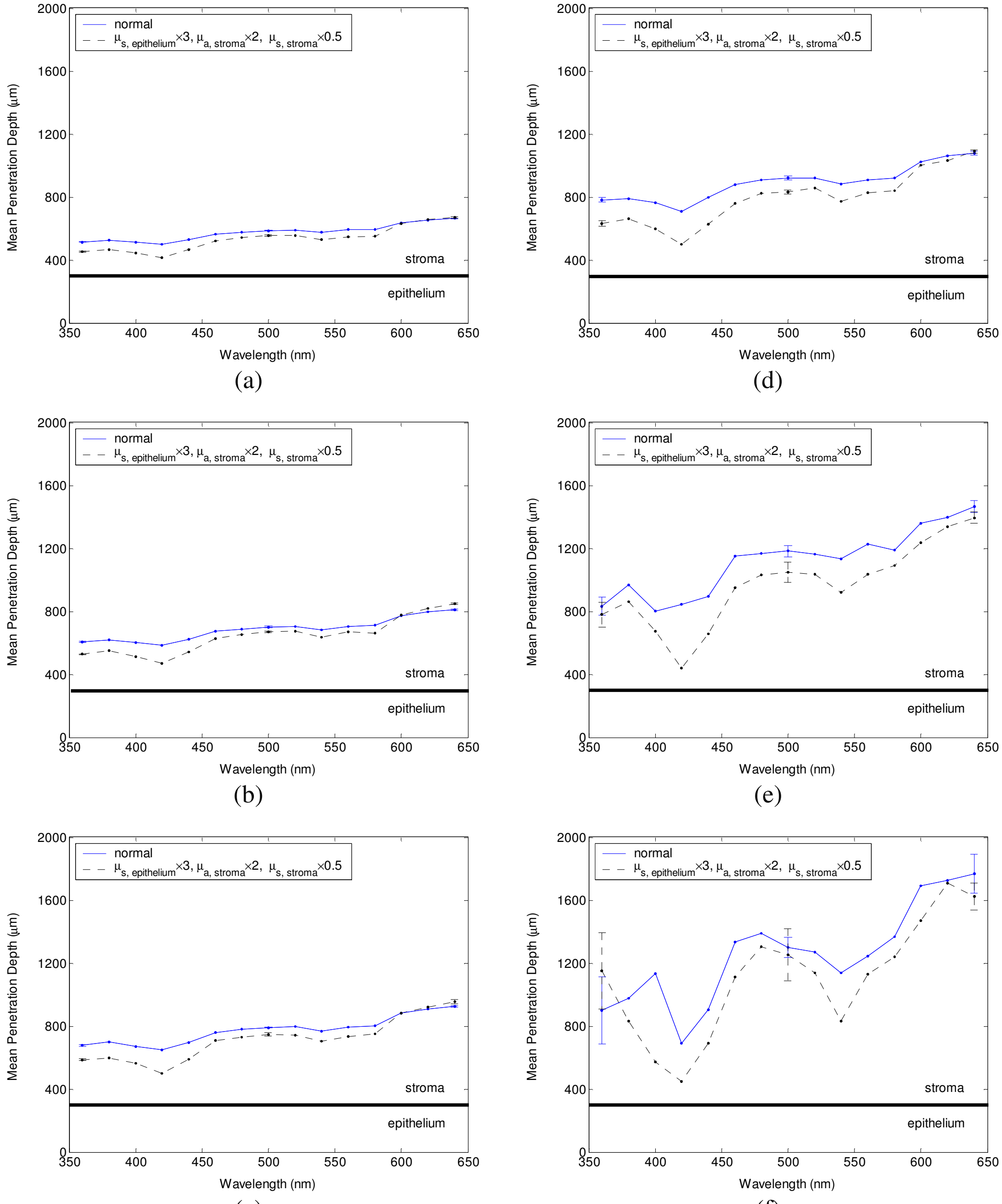

(a) (d)

(b) (e)

(c) (f)

Figure 4.9: Mean penetration depths computed for a source-detector separation of (a) 0.25 mm, (b) 0.50 mm, (c) 0.75 mm, (d) 1.10 mm, (e) 2.10 mm, and (f) 3.00 mm.

The results shown in Fig. 4.9 demonstrate that as the distance between the source and the detector increases, photons penetrate deeper into the tissue before they reach the detector fiber. The wavelength dependent increase in mean penetration depth is greater for larger source-detector separations. Note also that as the source-detector separation increases, hemoglobin absorption appears to have a more profound effect on the penetration depth profiles. The mean penetration depths are almost always smaller for the case with $\mu_{s,epithelium}\times3$, $\mu_{a,stroma}\times2$, and $\mu_{s,stroma}\times0.5$.

An important point to note is that even for the smallest source-detector separation, the mean penetration depth is greater than the epithelial thickness over the entire spectral range. This means that almost all of the photons collected penetrate into the stroma, and this source-detector geometry cannot exclusively probe the epithelial layer. In fact, the simulation results for the smallest source-detector separation indicate that the fraction of detected photons that only scatter in the epithelium and do not enter the stroma is as small as 0.2-0.6% for normal tissue. For the case with $\mu_{s,epithelium}\times3$, $\mu_{a,stroma}\times2$, and $\mu_{s,stroma}\times0.5$, this fraction increases to only about 5-17%. In both cases, the high end of the percentages corresponds to results computed at 420 nm.

## 4.4 DISCUSSION

Monte Carlo simulations presented in this chapter provide a quantitative understanding of the relationship between tissue optical properties and spatially resolved reflectance spectra. Increase in epithelial scattering, increase in stromal absorption, and decrease in stromal scattering are all likely to accompany dysplastic progression, but the results of the sensitivity analysis presented in Fig. 4.3 through Fig. 4.6 indicate that for the simulated fiber-optic probe geometry, increasing epithelial scattering has minimal effect on detected reflectance. The slight differences brought on by varying the epithelial scattering coefficient are mostly within the uncertainty limits of the simulation results. Increasing stromal absorption and decreasing stromal scattering, on the other hand, profoundly affect spectral reflectance. It is also important to note that changing a given optical parameter can lead to different trends in spectral response depending on the source-detector separation. This is best illustrated in Fig. 4.5, which shows that decreasing the stromal scattering coefficient decreases the reflectance intensity for small source-detector separations. For large source-detector separations, decreasing the stromal scattering coefficient tends to increase the reflectance intensity. This result is consistent with the diffusive characteristics of a highly scattering medium such as the stroma. A decrease in stromal scattering coefficient allows photons to penetrate deeper into the tissue and reduces the probability of reflection close to the source fiber. Thus, the number of photons detected at small source-detector separations decreases. Photons that penetrate deep into the stroma exit the tissue at larger distances from the source fiber, resulting in enhanced probability of detection at large source-detector separations.

In predicting reflectance spectra for dysplastic tissue, three different combinations of optical properties were tested. These different combinations focused on analyzing the effect of changing the stromal scattering coefficient. Simulation results indicate that increasing the epithelial scattering coefficient by a factor of three, increasing the stromal absorption coefficient by a factor of two, and decreasing the stromal scattering coefficient by 25% resulted in generation of spectra that were consistent with dysplastic changes observed in averaged clinical measurements. An important question is whether the dysplastic changes observed in averaged reflectance measurements can be explained through alternative combinations of optical properties. For example, intensity level differences can be accounted for by assuming no reduction in stromal scattering coefficient but by further elevating the stromal absorption coefficient. Note, however, that, as evidenced in Fig. 4.4, further elevation of stromal absorption would flatten out spectral features to an extent not consistent with clinical measurements. More importantly, visual inspection of the modeled spectra presented in Fig. 4.6 reveals that incorporation of reduced stromal scattering plays an integral role in characterizing the rate of wavelength dependent increase in reflectance intensity, especially for larger source-detector separations. Averaged reflectance spectra measured from highly dysplastic cervical sites illustrate that reflectance intensity for wavelengths greater than 600 nm tends to increase sharply for the three largest source-detector separations. Monte Carlo modeling results shown in Fig. 4.6 provide strong evidence that this behavior is most consistent with decreased scattering coefficient.

It should be emphasized that although the modeling results demonstrate good agreement with measured spectra on the average, Fig. 4.8 illustrates that there can be significant variability among clinical spectra from the same diagnostic category. Currently, there is no satisfactory understanding of the influence of biographical variables on biochemical, architectural or structural properties of cervical tissue. Hence, alterations in optical parameters due to differences in variables such as age, race, or hormonal status cannot be adequately quantified. If these variables influence the intensity of optical signals acquired from cervical tissue, significant interpatient variation is inevitable. It is also evident from Fig. 4.7 that even when patients from different age groups are considered separately, there can still be significant variability in reflectance intensity. This observation suggests that age alone cannot explain the variability in clinical measurements. On the average, however, the intensity differences between spectra from normal and highly dysplastic cervical sites tend to be larger for patients older than 35. It has been reported that collagen cross-linking increases with age [83], and differences in stromal scattering properties resulting from alterations in collagen matrix may provide a possible explanation for this trend.

The main benefit of acquiring spatially resolved reflectance spectra is the ability to probe different depths within the tissue. Penetration depth statistics presented in Fig. 4.9 indicate that larger source-detector separations sample deeper tissue regions, consistent with the results previously reported [32, 35, 66]. Figure 4.9 also illustrates that the wavelength dependent increase in mean penetration depth is much greater for large source-detector separations, leading to a more significant increase in the number of scattering events a photon undergoes before getting detected. This trend explains why the relative rate of wavelength dependent increase in reflectance intensity is higher for larger source-detector separations. Increasing the epithelial scattering coefficient and increasing the stromal absorption coefficient lead to a decrease in mean penetration depth, whereas decreasing the stromal scattering coefficient results in an increase in mean penetration depth. Figure 4.9 indicates that the combined effect of these changes is an overall decrease in mean penetration depth. This suggests that the same probe geometry can sample more superficial tissue depths when dysplasia is present.

Perhaps the most important aspect of the penetration depth analysis is the observation that the mean penetration depths calculated are always greater than the epithelial thickness. Simulation results indicate that almost all of the photons collected penetrate deep into the stroma and scatter many times before reaching the detector fibers. This is due to the fact that scattering in the epithelial layer is relatively low and mostly forward directed, and stroma is highly scattering. Even for the case where the source and the detector fibers are closely spaced, the number of detected photons that scatter only in the epithelium without penetrating into the stroma is negligibly small. This is consistent with the results shown in Fig. 4.3 where changes in epithelial scattering coefficient do not seem to have a significant effect on spectral reflectance even for the smallest source-detector separation.

Epithelial scattering is sensitive to changes in nuclear morphology and chromatin texture, which are important indicators of dysplastic progression [84]. Hence, collection of photons that only scatter in the epithelium without penetrating into the stroma is likely to improve the diagnostic potential of reflectance spectroscopy. Based on the simulation results presented in this chapter, we can conclude that the clinical fiber-optic probe geometry used in this study cannot resolve spectral information from the epithelial layer and is mainly sensitive to stromal optical properties. More creative fiber-optic probe designs are required to achieve a depth resolution that is sufficient to acquire spectral information unique to the weakly scattering epithelial layer.

### 4.5 CONCLUSIONS

The goal of the research presented in this chapter was to carry out modeling studies to explain the differences observed in spatially resolved reflectance spectra of normal and dysplastic cervical tissue. Monte Carlo modeling results provide a quantitative understanding of the specific contributions of different epithelial and stromal optical parameters to the overall spectral response. Predictions from simulations agree well with *in vivo* clinical measurements, and can successfully describe differences in intensity and shape of reflectance spectra obtained from normal and dysplastic tissue sites. The results from this study are expected to provide a basis to better interpret tissue spectra.

The diagnostic potential of reflectance spectroscopy can be optimized by designing fiber-optic probes that can reveal information about dysplastic changes in both the epithelium and the stroma. Probe design strategies to achieve selective sampling of these two tissue layers will be the focus of the next chapter.

# Chapter 5: Model-Based Analysis of Fiber-Optic Probe Designs to Resolve Spectral Information from Epithelium and Stroma

## 5.1 INTRODUCTION

For *in vivo* clinical studies, fiber-optic probes are widely used to deliver light to the tissue site of interest and to collect the reflected light [67]. The probability that photons reach a certain depth in the tissue before they are reflected back and detected is highly dependent on the source-detector geometry, indicating that the effective volume of the tissue visited by the detected photons depends on the specific arrangement of the source and detector fibers in the probe in addition to the tissue optical properties. Therefore, fiber-optic probe design plays a crucial role in obtaining depth-resolved spectroscopic information.

Depth resolution is clinically important since spatial localization of information obtained during *in vivo* measurements aids in interpretation of tissue spectra. This is particularly important when multi-layered tissues are being investigated. If different layers are selectively targeted, spectral information unique to each layer can reveal various aspects of dysplastic progression, increasing the diagnostic potential of optical spectroscopy.

Epithelial tissues, such as the intestine, oral cavity, and cervix, are generally described as two-layer media consisting of a thin epithelium on top of an underlying stroma. These two layers have significantly different optical properties and undergo different changes as dysplasia develops. As described in *Chapter 1* and *Chapter 4*, dysplastic changes include increased scattering from epithelial cells, decreased scattering from collagen fibers in the stroma beneath the epithelium, and increased absorption in the stroma due to increase in hemoglobin concentration. Increased scattering from epithelial cells is due to increased nuclear size, increased DNA content, and hyperchromasia with coarse and irregular chromatin clumping [13]. It is believed that the morphological structure of collagen fibers changes and the volume fraction of fibers decreases as dysplasia develops [14-17], leading to decreased scattering in the stroma. Increase in hemoglobin concentration and hence absorption is the result of increased microvessel density and angiogenic activity in dysplastic tissue [18, 19]. Such structural and biochemical changes are critical diagnostic indicators for development of pre-invasive cancer. Reflectance spectroscopy is capable of providing information about all of these changes noninvasively, and fiber-optic probe designs that can selectively collect light from the epithelium and the stroma are necessary to exploit the diagnostic information inherent in optical signatures specific to each layer.

Recent computational and experimental studies analyzing the influence of fiber-optic probe design parameters on depth sensitivity have mostly focused on fluorescence measurements. Results reported by Pfefer et al. [33, 34, 85] provide extensive insight into the effect of numerical aperture, fiber diameter, source-detector separation, or probe-to-tissue distance on the origin of detected fluorescence. Zhu et al. [36] and Skala et al. [37] have proposed probe designs that can provide enhanced sensitivity to epithelial fluorescence. The number of similar studies focusing on reflectance measurements is relatively limited.

Patterson et al. [66], Meglinskii and Matcher [32], and Larsson et al. [35] have investigated the relationship between the source-detector separation and the sampling depth. The results of these studies show that as the source-detector separation is increased, mean penetration depth of detected photons increases. Use of multiple source-detector separations is a common way to acquire depth-resolved reflectance signals [10, 67-70]. In epithelial tissues, however, scattering from epithelial cells is relatively low and mostly forward directed, and most of the reflected photons detected come from the highly scattering stroma beneath the epithelium. Even when the source and detector fibers are closely spaced, photons penetrate into the stroma and scatter many times before reaching the detector. As demonstrated in *Chapter 4*, depth resolution that can be achieved with minimal source-detector separation is not sufficient to selectively target the epithelial layer. Note that using a single fiber for both light delivery and collection as suggested by Papaioannou et al. [86] is not likely to provide enhanced sensitivity to the weakly scattering epithelial layer either. Further, such a single-fiber probe geometry is difficult to implement since special care needs to be taken in order to eliminate the possibility of detecting photons that are specularly reflected off the fiber tip. Specular reflection can, in principle, be accounted for by adopting a calibration scheme [87]. For tissue measurements, however, specular reflection at the fiber-tissue interface constitutes a dominant portion of the total detected reflectance [86]. More importantly, it is not possible to accurately assess the exact contribution of specularly reflected light to total reflectance signals for *in vivo* applications.

Collecting photons that only scatter in the epithelium and do not penetrate into the stroma is a challenging but nontrivial problem. Changes in the nuclei of epithelial cells are important indicators of pre-invasive cancer [84]. The fact that these changes alter the scattering properties of the epithelium indicates that epithelial scattering contains significant diagnostic information. In addition, pathologists have traditionally used atypical nuclear features in the epithelium as one of the major diagnostic criteria for dysplasia. Thus, isolation of epithelial scattering from stromal scattering is likely to prove invaluable in correlating optical signatures with the corresponding tissue histopathology, which is currently the gold standard in assessment of the sensitivity and the specificity of optical technologies targeting noninvasive detection of pre-cancerous changes.

In this chapter, I model two different fiber-optic probe designs to evaluate their potential in providing depth-resolved reflectance measurements from epithelial tissues. In the first design, the source and detector fibers are tilted with respect to the tissue surface, and the fiber tips are polished parallel to the surface. This geometry is based on a recent study by Nieman et al. [88] that suggests the use of obliquely oriented fibers to control the penetration depth of detected photons more precisely. In the second design, the source and detector fibers are coupled to a half-ball lens such that the flat surface of the lens faces the tissue. I have modified the multi-layered Monte Carlo code described in *Chapter 2* to be able to model tilted fibers and to incorporate photon propagation through the spherical lens interface. Simulations have been carried out to characterize the penetration depth of detected photons and to evaluate each probe with respect to the sampling depth. The emphasis of this work is on determining the potential of these two probe geometries in resolving spectral information from the epithelium and the stroma. I then use the simulation results to propose a probe design that can be used to acquire reflectance spectra unique to each tissue layer.

## 5.2 METHODS

### 5.2.1 Monte Carlo Modeling

Modifications have been made to the basic Monte Carlo implementation described in *Chapter 2* to simulate two different fiber-optic probe geometries. In the first case, the source and detector fibers are tilted at an angle with respect to the tissue surface. In the second case, the fibers are coupled to a half-ball lens, and the rules of photon propagation need to be changed to simulate refraction and reflection that take place at the curved surface of the lens. These two probe geometries are depicted in Fig. 5.1 and Fig. 5.2, respectively. The modifications that are necessary to account for tilted fibers or lens coupled fibers are explained below.

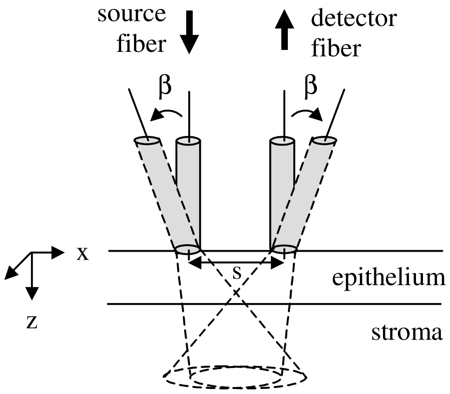

Figure 5.1: Fiber-optic probe geometry with tilted source and detector fibers. The fiber tips are polished parallel to the tissue surface.

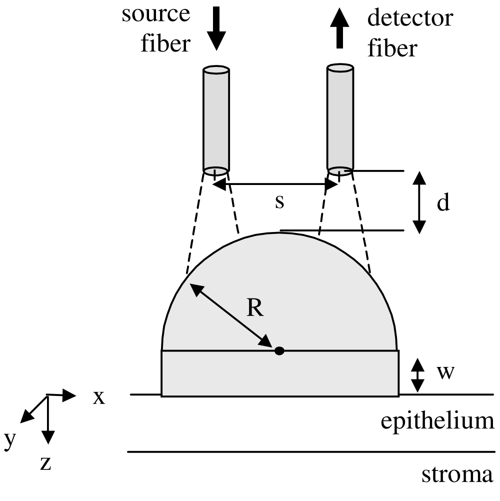

Figure 5.2: Fiber-optic probe geometry with half-ball lens coupled source and detector fibers. The fibers are symmetrically oriented around the central axis of the lens.

#### *5.2.1.1 Modeling Tilted Source and Detector Fibers*

As described in *Chapter 2*, each source or detector fiber is described by its radius, numerical aperture (NA), and refractive index. When the source fiber is oriented so that its axis is perpendicular to the tissue surface, the initial position of each photon is sampled from a circular region defined by the radius of the source fiber, and its initial trajectory is within the limits of a symmetric circular illumination cone determined by the fiber NA and refractive index. Reflected photons are detected when they exit under the detector fiber and within a circular collection cone determined by the NA and refractive index of the detector fiber.

Figure 5.1 illustrates the probe geometry where the source and detector fibers are tilted towards each other and are polished parallel to the tissue surface. The tilt angle for both fibers is denoted by $\beta$, and $s$ represents the center-to-center source-detector separation. In this case, the initial position of each photon needs to be sampled from an elliptical contact area. Also, when the source fiber is tilted, the illumination cone is no longer symmetric around the $z$ axis. Photon launch from a tilted source fiber can be implemented in Monte Carlo modeling by assuming circular symmetry around the fiber axis, and then by transforming the direction cosines describing the initial photon trajectory through three-dimensional matrix rotation about the y axis. The rotation matrix $M(\beta)$ is given by

$$M(\beta) = \begin{pmatrix} \cos\beta & 0 & \sin\beta \\ 0 & 1 & 0 \\ -\sin\beta & 0 & \cos\beta \end{pmatrix}. \tag{5.1}$$

Rotating the direction cosines of each launched photon through $\beta$ results in generation of an asymmetric elliptical illumination cone. Photons can then be propagated in the usual coordinate system where the $z$ axis is perpendicular to the tissue surface. Reflected photons are detected if their exit position falls under the elliptical contact area of the tilted detector fiber and their trajectory is within the limits of an asymmetric elliptical collection cone defined by the fiber NA, refractive index, and the tilt angle $\beta$. To determine whether a reflected photon is within the limits of the asymmetric collection cone, the direction cosines at the exit point are again rotated through $\beta$ about the $y$ axis. This three-dimensional matrix rotation, also performed using $M(\beta)$ defined in Equation (5.1), transforms the direction cosines to a coordinate system with circular symmetry around the detector fiber axis. Transformation among different coordinate systems using matrix rotation provides the easiest and the most direct way to generate asymmetric elliptical illumination and collection cones consistent with geometric optics principles.

#### *5.2.1.2 Modeling Half-Ball Lens Coupled Source and Detector Fibers*

Figure 5.2 illustrates the probe geometry where the source and detector fibers are positioned over a half-ball lens of radius $R$. The fibers are symmetrically oriented around the central axis of the lens, and the center-to-center source-detector separation is again denoted by $s$. The thickness of the air gap between the fiber tips and the top of the lens is represented by $d$. The figure also shows a window of thickness $w$ placed between the flat surface of the lens and the tissue surface.

I have modified the basic Monte Carlo implementation originally developed for infinitely wide and parallel layers to account for light propagation through the spherical lens surface. I have adopted a modeling scheme where the first two layers are allowed to have variable thickness. The first layer represents the air gap between the fibers and the half-ball lens, and the second layer represents the lens. Assignment of layer thickness is carried out reiteratively whenever a photon is about to encounter the spherical interface. Figure 5.3 shows a two-dimensional view of the case where a photon is incident on the lens from above. The refractive index of the lens is $n_2$, and the refractive indices of the layers above and below the lens are $n_1$ and $n_3$, respectively.

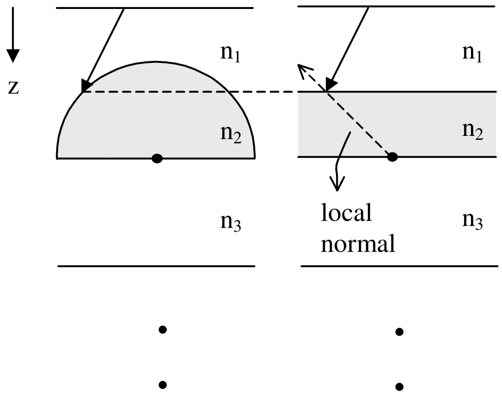

Figure 5.3: Modeling light propagation across the spherical lens interface through creation of a simulation geometry with infinitely wide and parallel layers.

The first step is to compute the coordinates where the photon will intersect the lens surface. The $z$ coordinate of the intersection point is then used to adjust the thickness of the first two layers and to create a simulation geometry with infinitely wide and parallel layers. Once the photon is moved to the boundary representing the lens interface, the decision of refraction or reflection needs to be based on the angle of incidence with respect to a local normal that characterizes the degree of curvature at the intersection point. As Fig. 5.3 demonstrates, the local normal is defined to be the vector pointing from the lens center to the intersection point. Direction of propagation after reflection or refraction is also determined with reference to the local normal.

A similar technique is applied when a photon approaches the spherical interface from within the lens. When the photon undergoes reflection and encounters the spherical boundary for a second time, however, the parallel layer geometry may no longer be valid. Depending on the $z$ component of the propagation vector after an occurrence of internal reflection, problems may arise as to whether the parallel layer formulation can be used to accurately describe the lens boundary. An example of such a situation is depicted in Fig. 5.4.

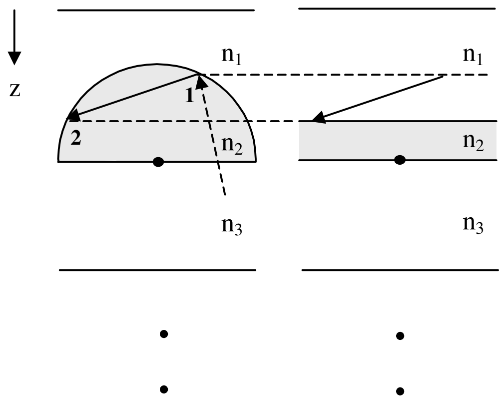

Figure 5.4: A situation where the parallel layer formulation fails to accurately describe the spherical lens boundary. When the photon encounters the spherical boundary for a second time, it should be considered to be incident from a medium with refractive index $n_2$ to a medium with refractive index $n_1$, but the parallel layer geometry assumption incorrectly suggests just the contrary.

In this case, even though the photon should be considered to be incident from a medium with refractive index $n_2$ to a medium with refractive index $n_1$, the parallel layer geometry assumption would incorrectly suggest just the contrary, as shown on the right side of the figure. Since the simulations described in this paper involve a high index lens, the photon is likely to get trapped within the lens due to total internal reflection. It will undergo successive internal reflections and will bounce across different parts of the spherical interface until it hits the flat surface of the lens. The model accounts for these multiple reflection cases by assigning the photon a random location on the flat surface of the lens and a random propagation vector with a positive $z$ component. Note that random sampling of photon position and propagation direction fits well within the context of Monte Carlo modeling. If a significant number of photons are simulated, such a statistical formulation for propagating multiply reflected photons provides a close approximation to spatial and directional randomization caused by successive occurrences of internal reflection off the spherical boundary.

In the modeling scheme described, I only consider photons that enter and exit the tissue through the flat surface of the lens. Photons that cross the interface representing this surface outside the circular contact area are terminated. Since the diameter of the half-ball lens determines the effective contact area of the probe, further propagation of photons exiting outside this region will not be relevant. In addition, photons impinging on the lens from above can reflect off the spherical surface and travel sideways and downwards away from the lens. On a few occasions, photons hitting the spherical interface from within the lens can refract and also travel sideways and downwards away from the lens. Further scattering of these stray photons can be avoided by shielding the inside wall of the probe with an absorptive material. Therefore, termination of such photons in Monte Carlo simulations does not lead to information loss.

In order to verify the part of the code related to light propagation through the spherical interface, I traced the path of a number of photons impinging on a half-ball lens with a given diameter and refractive index. In all cases, the computed trajectory was consistent with geometric optics.

### 5.2.2 Input for Monte Carlo Modeling

Simulations have been carried out at two different wavelengths, namely $\lambda$=450 nm and $\lambda$=650 nm. Each simulation has been performed using $10^8$ photons.

### *5.2.2.1 Tissue Parameters*

Epithelial tissue was considered to be a two-layer medium with the epithelium on the top and the stroma underneath. In accordance with Monte Carlo modeling presented in *Chapter 4*, the thickness of the normal epithelium was assumed to be 300 μm, which is an approximate average for epithelial tissues [76, 89], and the stroma was modeled as a semi-infinite medium. Use of realistic and relevant optical properties is a crucial part of modeling. The values used here to model normal epithelial tissue have already been reported in *Chapter 4*. These are mostly based on measurements from cervical tissue or other tissues having a similar architecture, and are assumed to provide a reasonable characterization of epithelial tissues in general. For convenience, the optical properties for the epithelium and the stroma at $\lambda$=450 nm and $\lambda$=650 nm are summarized in Table 5.1. Note that the two layers are index-matched with n=1.40. The refractive indices and the anisotropy factors are assumed to be independent of wavelength.

Table 5.1: Optical properties of normal epithelial tissue.

| Layer | n | $\mu_a$ (cm$^{-1}$) | $\mu_s$ (cm$^{-1}$) | g |
|---|---|---|---|---|
| $\lambda$=450 nm | | | | |
| Epithelium | 1.40 | 2.5 | 39.6 | 0.95 |
| Stroma | 1.40 | 4.3 | 248.5 | 0.88 |
| $\lambda$=650 nm | | | | |
| Epithelium | 1.40 | 1.2 | 27.4 | 0.95 |
| Stroma | 1.40 | 0.9 | 172.0 | 0.88 |

The assumptions I used in this chapter to model epithelial pre-cancer were consistent with those from *Chapter 4*. Briefly, I increased the epithelial scattering coefficient by a factor of three and the absorption coefficient in the stroma by a factor of two. I also decreased the stromal scattering coefficient by 50%. Even though simulation results from *Chapter 4* suggest that a decrease in stromal scattering coefficient by 25% is more consistent with spectral changes observed in *in vivo* measurements from highly dysplastic tissue sites, the main reason for incorporating a 50% decrease was to examine the sampling depth characteristics of different probe designs over a broader range of optical properties. The epithelial absorption coefficient, the refractive indices and the anisotropy factors were kept the same as in the case of normal tissue. Epithelial thickness was again assumed to be 300 μm [76].

#### *5.2.2.2 Fiber-Optic Probe Parameters*

For all the simulations, both the source fiber and the detector fiber were assigned a 100 μm diameter and a numerical aperture of 0.11 (in air). The refractive indices of the fibers were set to 1.50. I also assumed that the material in between the fiber tips was highly absorptive to prevent internal reflection of photons.

I chose sapphire as the high index material for the half-ball lens. The refractive index of sapphire is 1.78 for $\lambda$=450 nm and 1.76 for $\lambda$=650 nm. In all the simulations described in this paper, the radius $R$ of the half-ball lens was set to 0.5 mm, and the thickness of the air gap $d$ was 200 μm. Any window placed between the lens and the tissue was also made of sapphire. In addition to having significant refractive power, sapphire is extremely hard and resistant to scratching and abrasion. These characteristics make this substrate a suitable choice for optical applications in a clinical environment.

### 5.2.3 Output from Monte Carlo Modeling

Penetration depths of all the photons collected using each fiber-optic probe geometry have been recorded during the Monte Carlo simulations. Note that penetration depth as used here is defined to be the maximum $z$ depth in tissue at which a photon undergoes a scattering event. To illustrate the depth resolving characteristics of a given probe geometry, I present the penetration depth statistics in the form of histograms with a bin size of 10 μm up to a depth of 1000 μm. I also calculate the mean penetration depth for each simulation, which corresponds to the penetration depth averaged over all detected photons. Since the major goal of this paper is to evaluate the potential of each probe design in resolving spectral information from epithelium and stroma, another parameter of interest is the percentage of photons that only scatter in the epithelium without penetrating into the stroma. To provide better insight into the detection profiles of different probe geometries, I also recorded the number of scattering events each photon undergoes before reaching the detector fiber. For photons collected from the epithelium, I report the mean number of scattering events in the epithelial layer. For photons collected from the stroma, I report the mean number of scattering events in the epithelial layer and the stromal layer separately.

To establish model reliability, three simulations have been carried out for every case of probe geometry considered. The histograms shown represent the averages over three simulations. All the parameters calculated have also been averaged and the standard deviations have been determined based on the results from the three simulations. Since I simulate rather subtle source-detector geometries, I report these standard deviations to provide strong evidence for convergence of Monte Carlo modeling results.

## 5.3 RESULTS

### 5.3.1 Penetration Depth Statistics for Tilted Source and Detector Fibers

Figure 5.5 shows the penetration depth histograms obtained using the optical properties corresponding to those of normal tissue. The center-to-center source-detector separation $s$ is set to 150 μm for all cases. This separation represents the minimum distance between the fibers that allows enough spacing for fiber cladding as well as for extended fiber contact area resulting from tilting the fibers. The figure shows the penetration depth histograms for tilt angles of $\beta$=15° and $\beta$=30°. Results for $\beta$=0° are also included for comparison purposes. Histograms for $\lambda$=450 nm are shown in Fig. 5.5(a), and the histograms for $\lambda$=650 nm are shown in Fig. 5.5(b). The corresponding results for the mean penetration depth, percentage of photons collected from the epithelium, and the mean number of scattering events are given in Table 5.2.

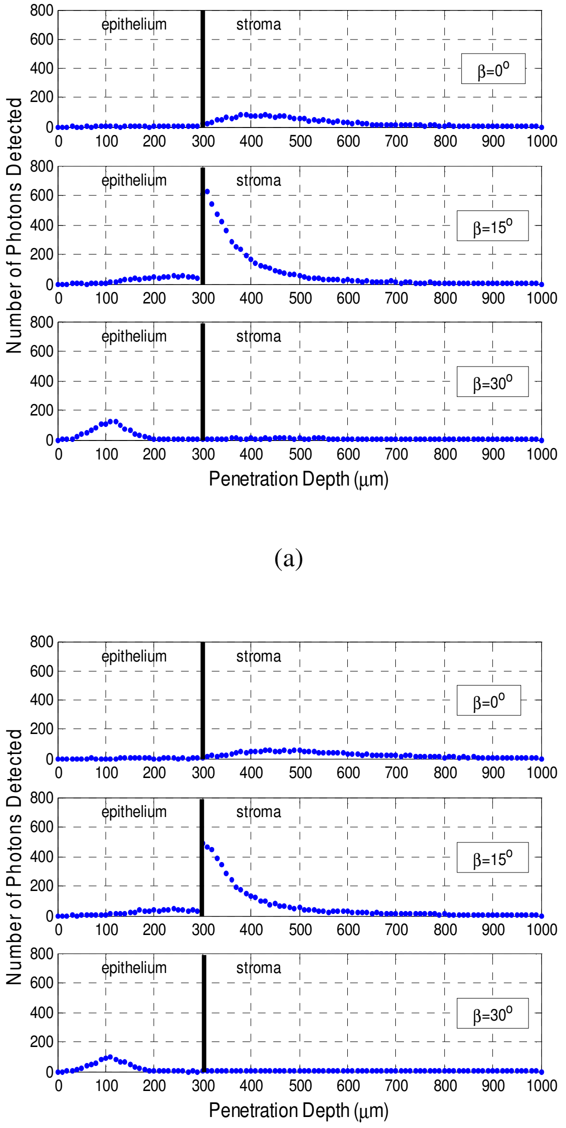

(a)

(b)

Figure 5.5: Penetration depth histograms for normal epithelial tissue at (a) λ=450 nm and (b) λ=650 nm, obtained using tilted source and detector fibers.

Table 5.2: Penetration depth statistics for normal epithelial tissue, obtained using tilted source and detector fibers.

| Case | Mean Penetration Depth (μm) | % Photons Collected from Epithelium | Mean Number of Scattering Events for Photons Collected from Epithelium | Mean Number of Scattering Events for Photons Collected from Stroma | |
|---|---|---|---|---|---|
| | | | | Epithelium | Stroma |
| λ=450 nm | | | | | |
| β=0° | 503 ± 3 | 0.7 ± 0.2 | 3.8 ± 0.4 | 2.4 ± 0.0 | 16.1 ± 0.3 |
| β=15° | 375 ± 0 | 11.4 ± 0.3 | 2.7 ± 0.1 | 2.2 ± 0.0 | 7.5 ± 0.0 |
| β=30° | 232 ± 2 | 74.9 ± 0.8 | 2.1 ± 0.0 | 3.0 ± 0.2 | 28.9 ± 0.4 |
| λ=650 nm | | | | | |
| β=0° | 608 ± 4 | 0.4 ± 0.0 | 3.2 ± 0.4 | 1.6 ± 0.0 | 17.5 ± 0.5 |
| β=15° | 410 ± 3 | 10.5 ± 0.1 | 2.2 ± 0.0 | 1.5 ± 0.0 | 7.8 ± 0.3 |
| β=30° | 330 ± 12 | 69.4 ± 1.4 | 1.7 ± 0.0 | 2.0 ± 0.0 | 39.1 ± 0.8 |

When β=0°, the penetration depth distributions are very broad and flat. Almost all of the photons collected come from the stroma. The fraction of detected photons that do not penetrate into the stroma is as small as 0.7% for λ=450 nm and 0.4% for λ=650 nm. Tilting both fibers towards each other by 15° results in narrower distributions with peaks shifted to the left. In this case, the penetration depth distributions peak at the junction of the epithelium and the stroma, and this geometry probes the superficial regions of the stroma. When β=30°, the majority of photons do not enter into the stroma and only scatter in the epithelium, but even though the peaks of the penetration depth distributions occur at about 100 μm into the epithelium for both wavelengths, there is still considerable contribution from the stroma. The fraction of photons collected from the epithelium is only 74.9% for λ=450 nm, and this fraction drops to 69.4% for

$\lambda$=650 nm. In fact, the mean penetration depth for $\lambda$=650 nm is greater than the epithelial thickness.

Note that the mean number of scattering events for photons collected from the epithelium decreases with increasing tilt angle. In the case of tilted fibers, photons undergo fewer scattering events in the epithelium before they reach the detector fiber. For photons collected from the stroma, the mean number of scattering events in both layers decreases in going from $\beta=0^o$ to $\beta=15^o$, but then increases for $\beta=30^o$.

Figure 5.6 and Table 5.3 show the results obtained using the optical properties corresponding to those of dysplastic tissue. The center-to-center source-detector separation $s$ is again 150 µm for all cases.

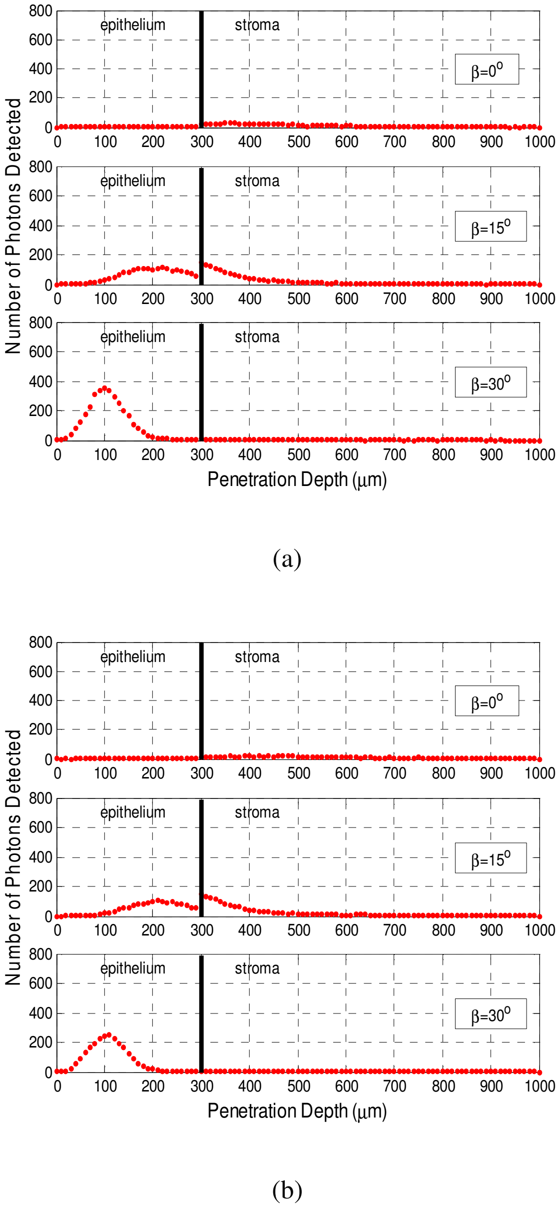

Figure 5.6: Penetration depth histograms for dysplastic epithelial tissue at (a) $\lambda$=450 nm and (b) $\lambda$=650 nm, obtained using tilted source and detector fibers.

Table 5.3: Penetration depth statistics for dysplastic epithelial tissue, obtained using tilted source and detector fibers.

| Case | Mean Penetration Depth (μm) | % Photons Collected from Epithelium | Mean Number of Scattering Events for Photons Collected from Epithelium | Mean Number of Scattering Events for Photons Collected from Stroma | |
|---|---|---|---|---|---|
| | | | | Epithelium | Stroma |
| $\lambda=450$ nm | | | | | |
| $\beta=0^{\circ}$ | 442 ± 4 | 14.1 ± 0.1 | 7.9 ± 0.5 | 7.2 ± 0.1 | 6.8 ± 0.1 |
| $\beta=15^{\circ}$ | 291 ± 3 | 55.9 ± 1.4 | 5.8 ± 0.1 | 6.8 ± 0.1 | 4.3 ± 0.1 |
| $\beta=30^{\circ}$ | 126 ± 1 | 96.4 ± 0.1 | 4.2 ± 0.0 | 9.2 ± 0.4 | 8.7 ± 0.8 |
| $\lambda=650$ nm | | | | | |
| $\beta=0^{\circ}$ | 597 ± 6 | 7.6 ± 1.2 | 6.0 ± 0.2 | 4.9 ± 0.1 | 8.3 ± 0.2 |
| $\beta=15^{\circ}$ | 342 ± 4 | 47.8 ± 1.0 | 4.4 ± 0.0 | 4.7 ± 0.1 | 4.7 ± 0.2 |
| $\beta=30^{\circ}$ | 147 ± 5 | 94.6 ± 0.3 | 3.2 ± 0.1 | 6.5 ± 0.1 | 14.5 ± 2.1 |

In the case of dysplasia, the mean penetration depths are smaller, and the percentage of photons collected from the epithelium increases for all tilt angles. Photons tend to undergo more scattering events in the dysplastic epithelium compared to the normal epithelium and fewer scattering events in the dysplastic stroma compared to the normal stroma. For $\beta=30^{\circ}$, the mean penetration depths for both wavelengths are well below the epithelial thickness, and the percentage of photons collected from the epithelium is 96.4% for $\lambda=450$ nm and 94.6% for $\lambda=650$ nm.

### 5.3.2 Penetration Depth Statistics for Half-Ball Lens Coupled Source and Detector Fibers

#### *5.3.2.1 Using Half-Ball Lens Coupled Fibers for Improved Depth Resolution*

Figure 5.7 shows the penetration depth histograms obtained for window thickness w=0 µm that represents the case where the flat surface of the half-ball lens is in direct contact with the tissue. The optical properties used correspond to those of normal epithelial tissue. The figure shows the penetration depth histograms for three different source-detector separations, namely s=500 µm, s=700 µm, and s=900 µm. Table 5.4 lists the results for the mean penetration depth, percentage of photons collected from the epithelium, and the mean number of scattering events.

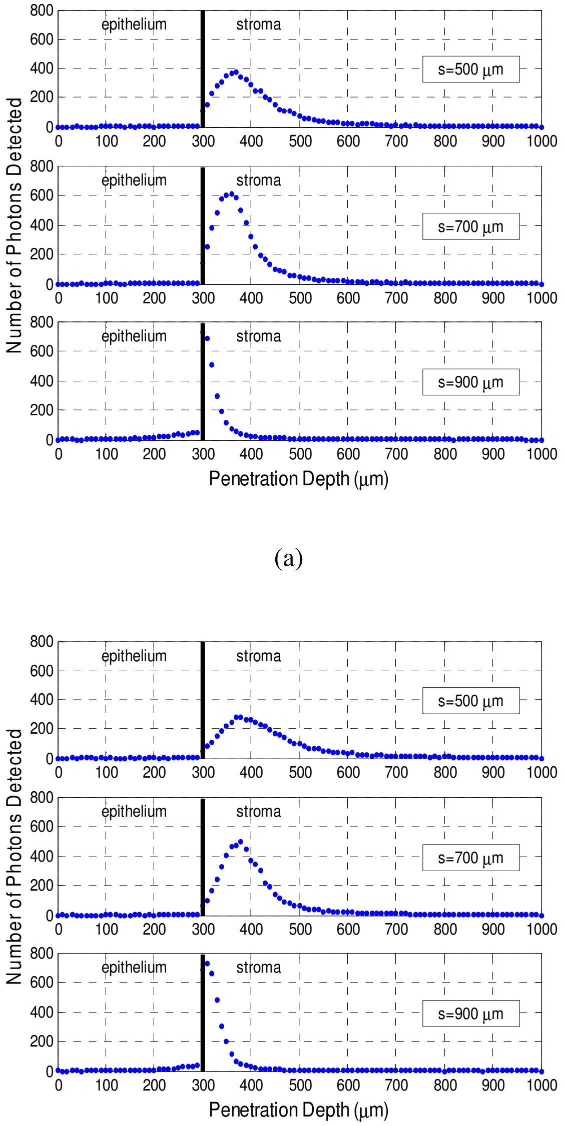

(a)

(b)

Figure 5.7: Penetration depth histograms for normal epithelial tissue at (a) λ=450 nm and (b) λ=650 nm, obtained using half-ball lens coupled source and detector fibers (w=0 μm).

Table 5.4: Penetration depth statistics for normal epithelial tissue, obtained using half-ball lens coupled source and detector fibers (w=0 μm).

| Case | Mean Penetration Depth (μm) | % Photons Collected from Epithelium | Mean Number of Scattering Events for Photons Collected from Epithelium | Mean Number of Scattering Events for Photons Collected from Stroma | |
|---|---|---|---|---|---|
| | | | | Epithelium | Stroma |
| λ=450 nm | | | | | |
| s=500 μm | 422 ± 2 | 0.6 ± 0.0 | 4.3 ± 0.3 | 2.2 ± 0.0 | 9.2 ± 0.1 |
| s=700 μm | 395 ± 1 | 0.5 ± 0.1 | 4.5 ± 0.4 | 2.3 ± 0.0 | 7.7 ± 0.0 |
| s=900 μm | 329 ± 1 | 11.4 ± 0.5 | 3.9 ± 0.0 | 2.7 ± 0.0 | 4.6 ± 0.1 |
| λ=650 nm | | | | | |
| s=500 μm | 467 ± 1 | 0.3 ± 0.0 | 3.3 ± 0.4 | 1.5 ± 0.0 | 8.8 ± 0.1 |
| s=700 μm | 429 ± 2 | 0.2 ± 0.0 | 3.6 ± 0.6 | 1.6 ± 0.0 | 7.2 ± 0.2 |
| s=900 μm | 346 ± 1 | 6.1 ± 0.1 | 3.2 ± 0.0 | 1.8 ± 0.0 | 4.3 ± 0.1 |

Increasing the source-detector separation and thus moving the fibers farther to the opposite edges of the lens results in narrower distributions. As *s* increases, the histogram peaks shift to the left and become more localized within superficial depths in the stromal layer. Photons tend to undergo fewer scattering events in the stroma before reaching the detector fiber, which is well correlated with increased depth localization.

The results for w=0 μm demonstrate that coupling the source and detector fibers to a half-ball lens significantly improves depth resolution for photons detected from the stroma. When the lens is in direct contact with the tissue, however, this probe geometry cannot exclusively probe the epithelial layer. Even for s=900 μm, the percentage of photons collected from the epithelium is negligibly small.

Simulation results indicate that incident photons that are specularly reflected at the lens-tissue interface account for approximately 3-4% of total detected reflectance for s=500 µm and s=700 µm, and 1% for s=900 µm. Penetration depth of these photons is not defined since they do not undergo scattering in the tissue. In calculating the parameters given in Table 5.4, I have excluded specularly reflected photons from consideration.

#### *5.3.2.2 Using Half-Ball Lens Coupled Fibers to Selectively Target the Epithelial Layer*

Simulations have been carried out to analyze the effect of placing a window between the flat surface of the lens and the tissue surface. Figure 5.8 and Table 5.5 show the results for w=300 µm, obtained using optical properties that characterize normal epithelial tissue.

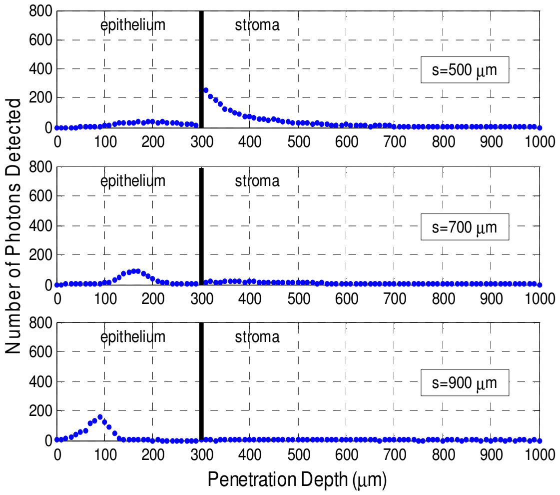

(a)

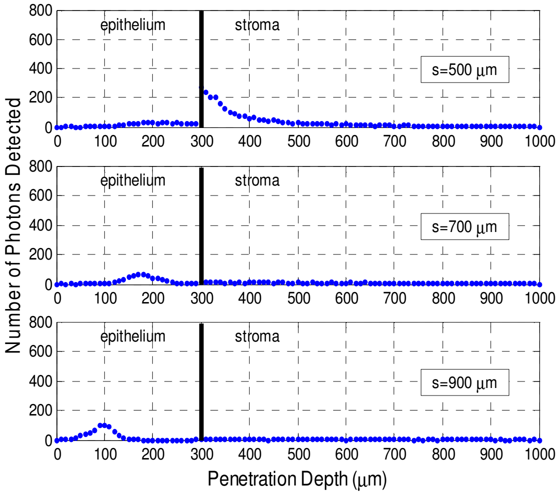

(b)

Figure 5.8: Penetration depth histograms for normal epithelial tissue at (a) λ=450 nm and (b) λ=650 nm, obtained using half-ball lens coupled source and detector fibers (w=300 μm).

Table 5.5: Penetration depth statistics for normal epithelial tissue, obtained using half-ball lens coupled source and detector fibers (w=300 μm).

| Case | Mean Penetration Depth (μm) | % Photons Collected from Epithelium | Mean Number of Scattering Events for Photons Collected from Epithelium | Mean Number of Scattering Events for Photons Collected from Stroma | |
|---|---|---|---|---|---|
| | | | | Epithelium | Stroma |
| λ=450 nm | | | | | |
| s=500 μm | 379 ± 0 | 18.4 ± 0.4 | 2.5 ± 0.1 | 2.4 ± 0.0 | 9.8 ± 0.2 |
| s=700 μm | 330 ± 5 | 55.4 ± 1.0 | 2.5 ± 0.0 | 2.9 ± 0.1 | 22.0 ± 0.8 |
| s=900 μm | 119 ± 2 | 93.8 ± 0.2 | 2.1 ± 0.0 | 3.5 ± 0.1 | 33.1 ± 4.6 |
| λ=650 nm | | | | | |
| s=500 μm | 427 ± 1 | 14.2 ± 0.2 | 2.1 ± 0.1 | 1.7 ± 0.0 | 9.9 ± 0.2 |
| s=700 μm | 417 ± 9 | 50.3 ± 0.7 | 2.1 ± 0.1 | 2.1 ± 0.1 | 25.0 ± 1.4 |
| s=900 μm | 187 ± 12 | 87.7 ± 1.0 | 1.7 ± 0.0 | 2.6 ± 0.1 | 44.0 ± 5.4 |

It is apparent that the presence of the window decreases the mean penetration depth of detected photons and increases the percentage of photons collected from the epithelium. When s=900 μm, the mean penetration depth is 119 μm for λ=450 nm and 187 μm for λ=650 nm, both values being well within the limits of the epithelial thickness. For λ=450 nm, 93.8% of photons collected do not enter the stroma and scatter only in the epithelium. This percentage for λ=650 nm is 87.7%.

Photons collected from the epithelium tend to undergo fewer scattering events with increasing *s*. In contrast, photons collected from the stroma undergo a greater number of scattering events in both layers as *s* is increased.

The penetration depth histograms and the penetration depth statistics corresponding to dysplastic epithelial tissue for w=300 µm are shown in Fig. 5.9 and Table 5.6, respectively.

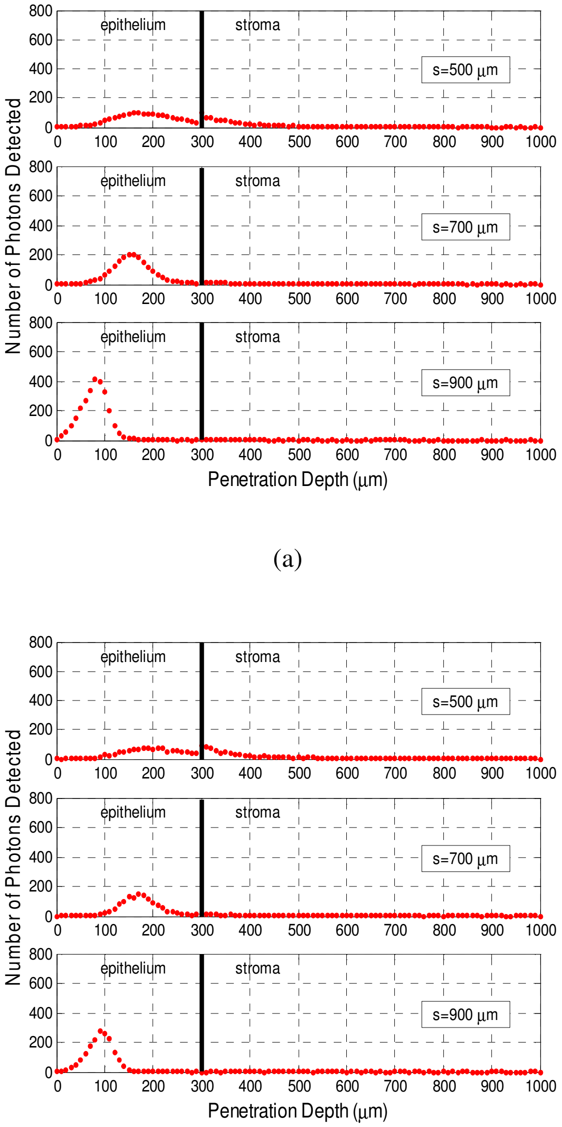

(a)

(b)

Figure 5.9: Penetration depth histograms for dysplastic epithelial tissue at (a) λ=450 nm and (b) λ=650 nm, obtained using half-ball lens coupled source and detector fibers (w=300 μm).

Table 5.6: Penetration depth statistics for dysplastic epithelial tissue, obtained using half-ball lens coupled source and detector fibers (w=300 µm).

| Case | Mean Penetration Depth (µm) | % Photons Collected from Epithelium | Mean Number of Scattering Events for Photons Collected from Epithelium | Mean Number of Scattering Events for Photons Collected from Stroma | |
|---|---|---|---|---|---|
| | | | | Epithelium | Stroma |
| λ=450 nm | | | | | |
| s=500 µm | 256 ± 5 | 67.6 ± 1.0 | 5.6 ± 0.1 | 7.2 ± 0.1 | 4.4 ± 0.3 |
| s=700 µm | 190 ± 2 | 90.3 ± 0.2 | 5.4 ± 0.0 | 8.3 ± 0.0 | 6.7 ± 0.6 |
| s=900 µm | 87 ± 1 | 99.1 ± 0.1 | 4.1 ± 0.0 | 10.6 ± 1.4 | 10.4 ± 1.3 |
| λ=650 nm | | | | | |
| s=500 µm | 322 ± 4 | 55.1 ± 1.0 | 4.3 ± 0.1 | 4.9 ± 0.0 | 5.0 ± 0.2 |
| s=700 µm | 236 ± 3 | 85.5 ± 0.8 | 4.2 ± 0.0 | 6.0 ± 0.1 | 8.9 ± 0.3 |
| s=900 µm | 108 ± 3 | 98.2 ± 0.3 | 3.3 ± 0.1 | 7.1 ± 0.4 | 18.8 ± 4.7 |

Comparison of these results to those for normal epithelial tissue reveals significant changes in mean penetration depth and percentage of photons collected from the epithelium for all source-detector separations. When s=700 µm or s=900 µm, there is a prominent increase in sensitivity to the epithelial layer. Especially for s=900 µm, almost all of the photons collected do not penetrate into the stroma and only scatter in the epithelium. The percentage of photons collected from the epithelium is 99.1% for λ=450 nm and 98.2% for λ=650 nm.

An important observation to make is that with w=300 µm, no specular reflection is detected. All the photons detected scatter in the tissue and the detected reflectance is entirely diffuse.

### 5.3.3 Probe Design to Selectively Target the Epithelial and Stromal Layers

Based on the simulation results for tilted and half-ball lens coupled fibers presented in previous sections, I propose a probe design that can be used to selectively target both the epithelium and the stroma. The proposed probe design is based on the geometry involving the sapphire half-ball lens. The design consists of two pairs of source and detector fibers positioned over the lens, and the window thickness is 300 μm. The fibers belonging to the first pair are oriented perpendicular to the tissue surface, and are characterized by a source-detector separation of 900 μm. The fibers belonging to the second pair are characterized by a source-detector separation of 500 μm, but instead of being positioned perpendicular to the tissue surface, they are tilted slightly away from each other, in a direction opposite to that shown in Fig. 5.1. The tilt angle for both the source and the detector fiber is specified to be $-5^{o}$, the negative sign being a reminder of the direction in which the fibers are tilted. The fiber tips are polished parallel to the tissue surface.

The penetration depth histograms and the penetration depth statistics for the proposed probe design are shown in Fig. 5.10 and Table 5.7, respectively. Although the results for the first fiber pair with s=900 μm and $\beta=0^{o}$ have already been presented in the previous section, I include those results as well to facilitate assessment of the depth selectivity characteristics of the probe.

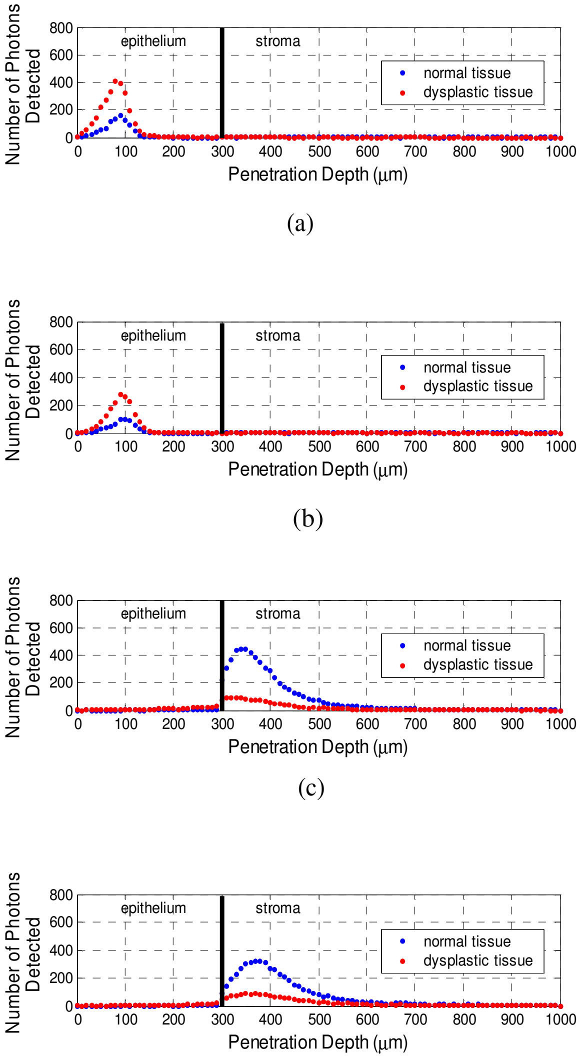

(a)

(b)

(c)

(d)

Figure 5.10: Penetration depth histograms for the proposed probe design with two pairs of half-ball lens coupled source and detector fibers, and a window with w=300 μm. The fiber pair with s=900 μm and $\beta=0^o$ can selectively target the epithelium at (a) $\lambda$=450 nm and (b) $\lambda$=650 nm, and the fiber pair with s=500 μm and $\beta=-5^o$ can selectively target the stroma at (c) $\lambda$=450 nm and (d) $\lambda$=650 nm.

Table 5.7: Penetration depth statistics for the proposed probe design.

| Target | Mean Penetration Depth (μm) | % Photons Collected from Epithelium | Mean Number of Scattering Events for Photons Collected from Epithelium | Mean Number of Scattering Events for Photons Collected from Stroma | |
|---|---|---|---|---|---|
| | | | | Epithelium | Stroma |
| Epithelium[1] | | | | | |
| $\lambda$=450 nm | | | | | |
| Normal | 119 ± 2 | 93.8 ± 0.2 | 2.1 ± 0.0 | 3.5 ± 0.1 | 33.1 ± 4.6 |
| Dysplastic | 87 ± 1 | 99.1 ± 0.1 | 4.1 ± 0.0 | 10.6 ± 1.4 | 10.4 ± 1.3 |
| $\lambda$=650 nm | | | | | |
| Normal | 187 ± 12 | 87.7 ± 1.0 | 1.7 ± 0.0 | 2.6 ± 0.1 | 44.0 ± 5.4 |
| Dysplastic | 108 ± 3 | 98.2 ± 0.3 | 3.3 ± 0.1 | 7.1 ± 0.4 | 18.8 ± 4.7 |
| Stroma[2] | | | | | |
| $\lambda$=450 nm | | | | | |
| Normal | 406 ± 1 | 0.8 ± 0.1 | 3.9 ± 0.4 | 2.2 ± 0.0 | 7.9 ± 0.1 |
| Dysplastic | 384 ± 2 | 15.7 ± 0.1 | 8.1 ± 0.0 | 6.8 ± 0.1 | 4.4 ± 0.1 |
| $\lambda$=650 nm | | | | | |
| Normal | 452 ± 0 | 0.4 ± 0.1 | 3.2 ± 0.1 | 1.5 ± 0.0 | 8.0 ± 0.2 |
| Dysplastic | 452 ± 1 | 7.6 ± 0.7 | 6.1 ± 0.3 | 4.5 ± 0.0 | 4.6 ± 0.1 |

[1] Epithelium is targeted using the fiber pair with s=900 μm and $\beta=0^{\circ}$.

[2] Stroma is targeted using the fiber pair with s=500 μm and $\beta=-5^{\circ}$.

The first fiber pair can selectively target the epithelium both at $\lambda$=450 nm [Fig. 5.10(a)] and at $\lambda$=650 nm [Fig. 5.10(b)]. The second fiber pair with s=500 μm and $\beta=-5^{\circ}$ is sensitive to the superficial stroma both for $\lambda$=450 nm [Fig. 5.10(c)] and for $\lambda$=650 nm [Fig. 5.10(d)]. Note that the number photons detected from the epithelium increases with progression of dysplasia, whereas the number of photons detected from the stroma decreases.

## 5.4 DISCUSSION

The depth range in the tissue to which a given probe geometry is most sensitive and the corresponding depth resolution can be estimated by considering the location and extent of the geometric overlap between the illumination and collection cones. It is important to remember though that the specific penetration depth profile of detected photons not only depends on this geometrical overlap but also on the optical properties of the tissue under consideration. With this fact in mind, I have carried out simulations at $\lambda$=450 nm and $\lambda$=650 nm to reveal wavelength dependent changes in penetration depth profiles. I have also tried to simulate changes in optical properties associated with severe dysplasia, and I have incorporated these changes to our modeling in order to provide some insight into differences in penetration profiles caused by dysplastic progression.

### 5.4.1 Tilted Source and Detector Fibers

When the source and detector fibers are oriented perpendicular to the tissue surface, the overlapping region of the illumination and collection cones extends to large depths within the tissue. In this case, photons detected exhibit a wide range of penetration depths, as demonstrated in Fig. 5.5 and Fig. 5.6. When the fibers are tilted, however, the illumination and the collection cones are slanted towards each other, and the overlapping region moves closer to the surface and is more localized. This trend results in improved depth selectivity and collection of photons from more superficial depths within the tissue.

For $\beta=15^{o}$, the simulation results for normal epithelial tissue imply that the illumination and collection cones overlap over the superficial stroma and then diverge from each other, leading to increased sensitivity to this region. The fact that photons undergo fewer scattering events in the stroma before reaching the detector fiber is also consistent with this localization. Photons collected from the epithelium undergo fewer scattering events as well. Since the fibers are tilted towards each other, photons no longer need to backscatter through large angles to reach the detector. Since they enter the tissue at an angle, there is increased probability that they can reverse their path through fewer number of scattering events and travel towards the detector. The detector, which is also oriented at an angle, favors collection of photons that backscatter through smaller angles.

The results for $\beta=30^{o}$ indicate that the illumination and collection cones overlap over the epithelial layer and then diverge from each other more rapidly with little or no overlap over the stromal layer. The probe geometry is mostly sensitive to epithelial scattering. Photons collected from the epithelium undergo fewer scattering events, again consistent with even higher probability of backscattering towards the detector. It is important to note that photons collected from the stroma undergo a greater number of scattering events in the stromal layer compared to the $\beta=15^{o}$ case. Due to the increased tilt angle and more rapidly diverging illumination and collection cones over the stromal layer, photons from the stroma need to scatter more in order to alter their path and enter the collection cone where there is increased probability of detection.

Comparison of Fig. 5.6 to Fig. 5.5 and Table 5.3 to Table 5.2 reveals significant differences between penetration depth profiles of normal and dysplastic epithelial tissue. There is a noticeable increase in sensitivity to the epithelial layer for dysplastic tissue, and this trend is consistent with increased epithelial scattering, decreased stromal scattering, and increased stromal absorption that accompany dysplasia. Increase in epithelial scattering and decrease in stromal scattering associated with dysplastic progression are also reflected in statistics regarding the number of scattering events.

There are practical limits on the maximum tilt angle that can be achieved. If the overall dimension of the fiber-optic probe is to be kept small, the fibers cannot be tilted extensively. There is also an upper limit on the extent of bending that a fiber can tolerate. Tilt angles greater than $30^o$ are difficult to construct in a compact package and have not been considered in this work. The results shown in Table 5.2 for normal epithelial tissue indicate that even when the fibers are placed close to each other and are tilted to the maximum extent compatible with design limitations, a significant percentage of detected photons still comes from the stroma. Even though the illumination and collection cones overlap over the epithelium, the angle at which the cones diverge from each other is not sufficient to eliminate detection of photons from the highly scattering stroma. Therefore, we can conclude that this probe geometry does not have the potential to provide adequate separation of epithelial scattering from stromal scattering in the case of normal tissue. On the other hand, the results for $\beta=30^o$ given in Table 5.3 demonstrate that the same probe geometry provides significant separation of epithelial scattering from stromal scattering in the case of dysplastic tissue. Such a contrast in penetration depth profiles of normal and dysplastic tissue is not desirable since we would like to be able to compare spectra unique to each of the two layers. We need a probe design that demonstrates comparable performance in isolating epithelial scattering from stromal scattering for both normal and dysplastic tissue.

### 5.4.2 Half-Ball Lens Coupled Source and Detector Fibers

Instead of physically tilting the fibers, we can make use of the refractive power of a high-index spherical lens to obtain slanted illumination and collection cones. Figure 5.7 illustrates the depth selectivity potential of a sapphire half-ball lens in direct contact with normal epithelial tissue. As the source and detector fibers are moved to the outer edges over the lens, the angle at which the illumination and collection cones intersect within the tissue increases. The cones overlap over more superficial tissue depths and then diverge rapidly in opposite directions, giving rise to increased depth selectivity.

When the lens is in direct contact with the tissue, however, the overlapping region of the illumination and collection cones occurs in the stroma. Simulation results also indicate that for w=0 µm, specular reflection accounts for a few percent of the total detected reflectance. For the three source-detector separations used in the simulations, the illumination and collection paths do not intersect on the flat surface of the lens. Therefore, incident photons that are specularly reflected at the lens-tissue interface are not directed towards the detector. Detected specular reflection is attributable to incident photons undergoing internal reflection at the flat surface of the lens, bouncing back from around the central part of the spherical interface, and undergoing reflection at the flat surface of the lens a second time. Due to spherical symmetry, some of these photons reach the detector fiber within the limits of the numerical aperture.

The epithelial layer can selectively be targeted by inserting a sapphire window between the flat surface of the lens and the tissue surface. The extended pathlength within the window brings the illumination and collection cones closer together on the surface of the tissue. Comparison of Fig. 5.8 to Fig. 5.7 suggests how the penetration depth profiles are affected by the presence of the window. Table 5.5 shows that photons collected from the epithelium tend to undergo fewer scattering events as the source-detector separation increases, similar to the effect caused by increasing the tilt angle of the fibers. Also, photons collected from the stroma undergo a greater number of scattering events in the stromal layer. This is again due to more rapidly diverging illumination and collection cones over the stromal layer, and photons need to scatter more in order to alter their path and reach the detector. Table 5.5 indicates that with s=900 μm, which represents the case where the source and detector fibers are placed at the very edges of the lens, a significant percentage of detected photons comes from the epithelium at both wavelengths. It can be concluded that placing the fibers far apart over the lens is an effective way of creating illumination and collection cones that are steep enough to eliminate collection of photons from the stroma. Simulation results in Fig. 5.9 and Table 5.6 imply that s=900 μm also provides excellent sensitivity to the epithelial layer in the case of dysplastic tissue. Therefore, this probe geometry is capable of providing sufficient separation of epithelial scattering from stromal scattering for both normal and dysplastic tissue.

Placement of a sapphire window between the flat surface of the lens and the tissue surface not only enables selective targeting of the epithelial layer but also eliminates detection of specularly reflected photons. With the window in place, the incident photons reach the base of the window at a location closer to the central axis of the lens. If these photons are reflected, they will no longer hit the region around the tip of the spherical interface. This will effectively break the spherical symmetry that has led to collection of specular reflection in the w=0 µm case. Note that the window thickness needs to be adjusted carefully in order to avoid overlap of illumination and collection paths over the base of the window. As long as the source-detector separation is not smaller than 500 µm, an upper limit of 300 µm on the window thickness ensures that no such overlap will occur and photons that are specularly reflected at this interface will not travel directly towards the detector.

I have observed that the penetration depth profiles are not strongly dependent on the thickness of the air gap between the tip of the fibers and the top of the lens. Changing the thickness of the air gap to 100 µm or to 300 µm has minimal effect on parameters such as the mean penetration depth or the percentage of photons collected from the epithelium.

### 5.4.3 Proposed Probe Design

While the epithelial layer can selectively be targeted using half-ball lens coupled fibers that are oriented perpendicular to the tissue, and a window with w=300 µm, the ability to selectively target the stromal layer has been compromised. Even though s=500 µm can be used to selectively probe the stroma in the case of normal epithelial tissue, the results given in Table 5.6 indicate that the same is not true for dysplastic epithelial tissue. With w=300 µm, a source-detector separation which is smaller than 500 µm leads to collection of specularly reflected photons and cannot be used to obtain increased sensitivity to the stromal layer.

It is possible to overcome this problem by keeping the source-detector separation at 500 µm but by using tilted source and detector fibers. Tilting the fibers slightly away from each other brings the overlapping region of the illumination and collection cones over to the superficial stroma. The proposed tilt angle is only $5^o$ and such a small tilt angle can easily be implemented within the 500 µm space.

The results compiled in Fig. 5.10 and Table 5.7 show that the depth selectivity achieved by the two fiber pairs is sufficient to selectively target both the epithelium and the stroma. Note that the penetration depth profiles for both fiber pairs are consistent across the two diagnostic categories, evidenced by histogram peaks localized within similar tissue depths. The mean penetration depths and the percentages listed in Table 5.7 for normal and dysplastic tissue are also comparable for all four cases. This consistency in depth selectivity is a crucial advantage that can benefit interpretation of tissue spectra.

An important consideration in the design of a fiber-optic probe is the efficiency of the optical setup. Since the fibers are in contact with air, specular reflection off the fiber tips is on the order of 5%. Also, sapphire has a high refractive index, and specular reflection off the spherical interface is likely to degrade the efficiency of the proposed probe. Monte Carlo simulation results indicate that for the tilted fiber pair with s=500 µm, the fraction of incident photons lost to specular reflection off the lens surface is about 10% for d=200 µm. For the fiber pair with s=900 µm, this loss increases to about 15%. At the same time, the edges of the fibers separated by 900 µm are aligned with the edges of the spherical lens. Some of the photons leaving the source fiber will miss the lens and hit the inside wall of the probe. Since the numerical aperture of the source fiber is only 0.11, the fraction of incident photons that will miss the lens is about 10% for d=200 µm. Similarly, the full numerical aperture of the detector will not be utilized to collect photons exiting the tissue. Simulation results show that signal levels obtained using lens coupled fibers are indeed lower compared to those obtained using tilted fibers in contact with the tissue. Note, however, that the collection efficiency of a given source-detector geometry cannot be characterized simply by the total number of photons detected. A more appropriate way of assessing collection efficiency in the context of this work is to consider signal magnitude in conjunction with depth selectivity. To give a specific example, results for normal epithelial tissue at $\lambda$=450 nm indicate that the total number of photons detected using lens coupled fibers with s=900 µm is about 30% less than the total number of photons detected using tilted fibers with $\beta=30^o$. Approximately 20% of this decrease in signal magnitude is in fact due to the ability of the lens coupled fiber pair to limit the sampling depth and to successfully eliminate detection of photons from the highly scattering stroma. Hence, coupling the source and detector fibers to a sapphire lens does not lead to considerable reduction in number of photons collected from the epithelium, which, in this particular case, is the target layer. Comparison of the penetration depth histograms for the proposed probe design and to those for tilted fibers in contact with the tissue also reveals comparable signal levels from respective tissue layers. Therefore, we can conclude that the focusing power of the lens compensates for a significant portion of optical losses associated with fiber-lens coupling. Specularly reflected photons or incident photons that miss the lens surface are sources of stray light within the probe. If the inside wall of the probe is shielded with an absorbing material, further scattering of these stray photons will be avoided.

### 5.4.4 Implications

Many different techniques have recently been employed to selectively target the epithelial layer and isolate epithelial scattering from stromal scattering. Light scattering spectroscopy or polarized reflectance spectroscopy have been shown to be sensitive to pre-cancerous changes in the epithelium [6, 9, 21, 22, 88]. Other methods proposed to target the most superficial depths within epithelial tissues include differential path-length spectroscopy [90] and low-coherent backscattering spectroscopy [91, 92]. The approach presented in this chapter is based on improvement of depth selectivity simply through optimization of the fiber-optic probe design.

Ball or half-ball lens coupled fibers have been widely used for medical applications including laser surgery or photodynamic therapy [93]. The purpose of using a lens element in these applications is to increase light intensity at the tip of the probe. Motz et al. [94] have recently described a probe design for biomedical Raman spectroscopy, where a sapphire ball lens inserted to the tip of the probe provides signal enhancement and increased collection efficiency. In this work, I have shown that a sapphire half-ball lens is capable of providing depth selectivity and improved depth resolution. Specifically, the simulation results for epithelial tissues indicate that it is possible to use lens coupled source and detector fibers to isolate epithelial scattering from stromal scattering.

The proposed probe design provides a simple and efficient means to selectively collect light from both the epithelium and the stroma, and enables acquisition of reflectance spectra unique to each of the two layers. As a result, optical trends from both tissue layers can be monitored for any changes associated with pre-cancer progression. Spectra unique to the epithelium will be sensitive to dysplastic changes in epithelial cells, whereas spectra unique to the stroma will be sensitive to dysplastic changes in collagen fibers and microvessel density.

In addition to providing resolution of spectral information from epithelial and stromal layers, the proposed design is extremely compact. The overall dimension of the fiber-optic probe is roughly determined by the lens diameter, which is as small as 1 mm. Such a small probe can provide easy access to epithelial tissues including the cervix and the oral cavity, and can also be integrated into an endoscope for detection of dysplasia in otherwise inaccessible organ sites such as the intestine.

The principle of depth selectivity using lens coupled fibers can also be applied to target epithelial fluorescence in fluorescence spectroscopy. Since sapphire has no autofluorescence, the design can possibly be extended for use in fluorescence measurements as well. In fact, initial results reported by Schwarz et al. [95] are promising, but modeling studies are required to characterize depth selectivity specific to fluorescence measurements.

## 5.5 CONCLUSIONS

The diagnostic performance of *in vivo* biomedical optical spectroscopy is strongly dependent on the ability of the fiber-optic probe to target diagnostically significant features. Computational studies are necessary to investigate the relationship between probe geometry and origin of detected optical signal. The goal of the research presented in this chapter was to use Monte Carlo modeling to suggest a probe design for reflectance-based detection of pre-cancer in epithelial tissues. Simulations have been performed to evaluate different probe geometries with respect to the sampling depth. The results provide a guideline for design and optimization of a fiber-optic probe that can resolve spectral information from the epithelium and the stroma. Selective targeting of these two distinct layers will enable simultaneous assessment of dysplastic changes unique to each layer, and will improve the ability of reflectance spectroscopy to differentiate pre-cancerous epithelial tissue from normal epithelial tissue.

# Chapter 6: FDTD Modeling of Light Scattering from Normal and Dysplastic Cervical Cells at Different Epithelial Depths

## 6.1 INTRODUCTION

Understanding the changes in light scattering properties of dysplastic epithelial cells relative to normal epithelial cells is required to facilitate interpretation of tissue spectra obtained with scattering-based optical diagnostic techniques including reflectance spectroscopy, light scattering spectroscopy (LSS), and polarized reflectance spectroscopy. It has been demonstrated that reflectance confocal microscopy (RCM), optical coherence tomography (OCT), and optical coherence microscopy (OCM) can differentiate between normal and dysplastic epithelium in many different organ sites [96-103]. Therefore, these imaging modalities have also emerged as promising tools for detection of epithelial pre-cancer. Optical signals obtained with RCM, OCT, or OCM are modulated by the scattering properties of the tissue being imaged. Therefore, a detailed analysis of the light scattering characteristics of epithelial cells can lead to a better interpretation of acquired images, and aid in screening and diagnosis of pre-invasive cancer.

Changes in the nuclei of the epithelial cells are the most important indicators of dysplasia. These changes include increased nuclear size, asymmetric nuclear shape, increased DNA content, and hyperchromasia with coarse and irregular chromatin clumping [84, 104]. To illustrate nuclear changes associated with dysplasia, Fig. 6.1 shows two different cervical biopsy images, one classified as a normal epithelium [Fig. 6.1(a)] and the other as a highly dysplastic epithelium [Fig. 6.1(b)].

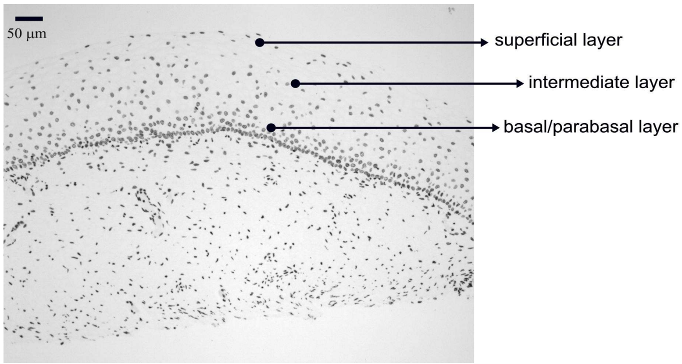

(a)

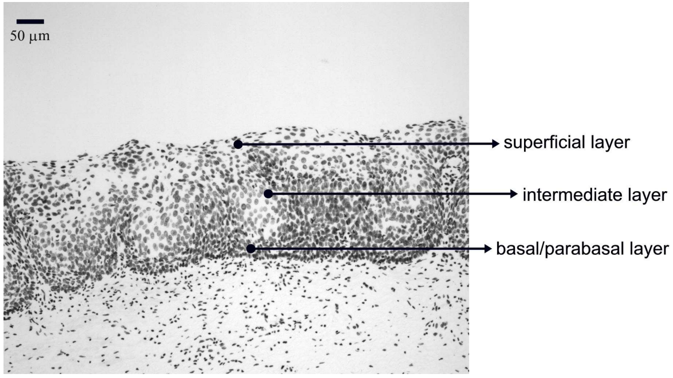

(b)

Figure 6.1: (a) Normal and (b) highly dysplastic cervical biopsy images showing the basal/parabasal, intermediate, and superficial epithelial layers. The biopsies are stained with Feulgen-Thionin, which is stoichiometric for DNA.

Figure 6.1 demonstrates that the density of nuclei is greater in the case of dysplasia, where large pleomorphic nuclei occupy the whole epithelium. The superficial, intermediate, and basal/parabasal layers describing different regions of the epithelium are also indicated on the figure. Note that for both the normal and the dysplastic epithelium, each epithelial depth displays different characteristics, with the superficial nuclei being smaller and more condensed and the basal nuclei larger and rounder.

Pathologists have traditionally used atypical nuclear features in the epithelium as one of the major diagnostic criteria for dysplasia. DNA ploidy has also been suggested to be a significant prognostic factor for assessing disease status and predicting treatment outcomes [105-107]. The optical diagnostic techniques described above have the potential to be used for determining the structure of epithelial cells without the need for biopsy removal. They can non-invasively provide quantitative information about nuclear features that can be used for early clinical diagnosis of pre-invasive cancerous changes.

The extraction of quantitative morphological information from signals obtained in LSS or polarized reflectance spectroscopy has so far been achieved using models based on Mie theory for homogeneous spherical scatterers [21, 22, 108, 109]. Although these studies have yielded promising results using theoretical formalism based on Mie scattering, which approximates the cells and their nuclei as homogeneous spherical objects, there is currently no experimental evidence for the validity of using Mie theory to model light scattering from cells. Biological cells are complex inhomogeneous structures that cannot be adequately described as simple Mie scatterers. The nuclear features and organelles are likely to contribute to scattering from cells. In fact, cellular scattering measurements demonstrate that the scatterer sizes in biological cells range from 0.4 µm to 2.0

μm [110]. These scatterer sizes indicate that scattering arises not only from nuclei but also from structures within the nuclei and possibly from cytoplasmic organelles. Therefore, establishing a better understanding of light scattering at the cellular level requires more detailed modeling that can incorporate complicated morphology and internal structure characteristic of cells.

The FDTD method has recently provided a flexible approach to study scattering that arises from inhomogeneous epithelial cells of arbitrary shape [43-45], and it has offered important insights into the relationship between cellular morphology and light scattering. Results show that for amelanotic epithelial cells, which have a low volume fraction of mitochondria, inhomogeneities in the nucleus play an important role in determining high-angle scattering characteristics, while the nuclear size is important in forward scattering [45]. The FDTD method has also been used to investigate how the light scattering properties of cervical cells are affected by changes in nuclear morphology, DNA content, and chromatin texture that occur during neoplastic progression [13]. Results indicate that cellular scattering properties are sensitive to DNA content of nuclei and chromatin texture in addition to nuclear size.

This chapter describes the use of the implemented FDTD algorithm described in *Chapter 3* to model light scattering from normal and dysplastic cervical cells at three different epithelial depths, namely basal/parabasal, intermediate, and superficial. Construction of realistic cell geometries is a crucial part of modeling. In this work, I use morphological features and chromatin texture information obtained from quantitative histopathology to create realistic cell models within the FDTD grid.

## 6.2 METHODS

### 6.2.1 Quantitative Histopathology

To use FDTD modeling to study the scattering characteristics of normal and dysplastic cells, nuclear changes associated with dysplasia must first be quantified. This can be achieved by analyzing quantitative images of Feulgen-Thionin stained cervical cell nuclei. The Feulgen-Thionin stain is stoichiometric for DNA [84, 111], therefore these images provide information about nuclear morphology, DNA content and chromatin organization, and highlight the differences between normal and dysplastic cervical cell nuclei.

The quantitative images used in this chapter were provided by the British Columbia Cancer Agency (Vancouver, Canada). The clinical study was conducted at The University of Texas M.D. Anderson Cancer Center in Houston. Each patient involved in the study underwent colposcopy. Four adjacent tissue sections were sliced from each biopsy taken during the colposcopic examination. Three of the tissue sections were stained with hematoxylin and eosin (H&E) and used for clinical diagnosis. A group of pathologists classified the sections as either normal, human papilloma virus (HPV), or cervical intraepithelial neoplasia (CIN). The CIN sections were further sub-classified as CIN 1 (mild dysplasia), CIN 2 (moderate dysplasia), or CIN 3 (severe dysplasia or squamous carcinoma *in situ*). The remaining fourth tissue section was stained with Feulgen-Thionin and used for quantitative histopathologic analysis at the British Columbia Cancer Agency. A pathologist mapped the diagnostic area on the Feulgen-Thionin stained tissue section, indicating the region containing the cells with the worst diagnosis. An in-house semi-automatic image analysis system (Department of Cancer Imaging, British Columbia Cancer Agency) was then used to acquire an image of the section. A special image analysis software automatically carried out the process of nuclear segmentation and the calculation of nuclear feature statistics. All the nuclei imaged were also categorized into four different epithelial depths, namely basal, parabasal, intermediate, and superficial. This classification was based on the location of a specific nucleus relative to the entire thickness of the epithelium and also on the cell examination.

In this work, I only consider normal and CIN 3 nuclei. The quantitative histopathologic analysis included 5 normal biopsies taken from 4 different patients, and 16 CIN 3 biopsies taken from 16 different patients. The total number of normal nuclei imaged was 562, and the total number of CIN 3 nuclei imaged was 1069. For the calculation of nuclear feature statistics, I combined nuclei from basal and parabasal layers in a single category, since it was usually very difficult to distinguish between the two, especially in the case of severe dysplasia.

Figure 6.2 shows a subset of the nuclear images provided. Each pixel corresponds to an area of 0.34 μm × 0.34 μm.

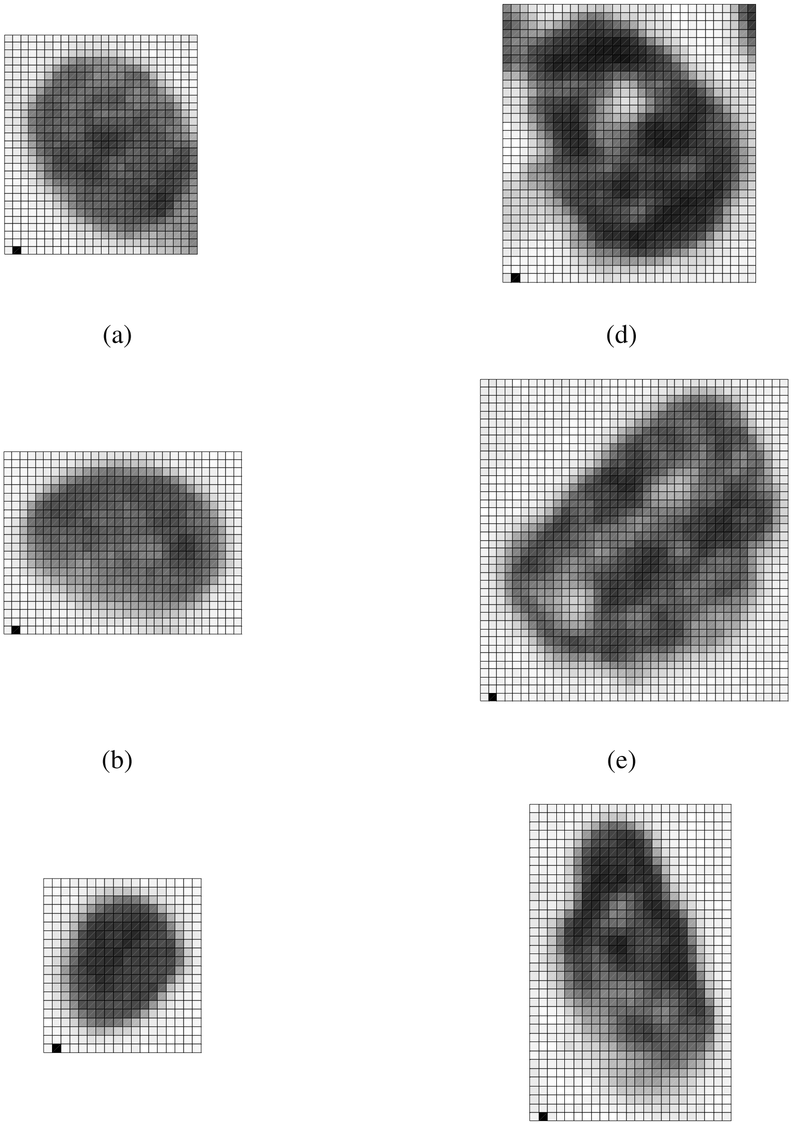

(a) (d)

(b) (e)

(c) (f)

Figure 6.2: Quantitative images for (a) normal, basal/parabasal, (b) normal, intermediate, (c) normal, superficial, (d) CIN 3, basal/parabasal, (e) CIN 3, intermediate, and (f) CIN 3, superficial, nuclei. Each pixel shown is 0.34 μm × 0.34 μm.

The figure shows the differences between nuclei in different layers and demonstrates most of the features characteristic of CIN 3. It is important to consider nuclei in different layers separately since there are differences in their size and chromatin structure. Normal basal/parabasal and intermediate cell nuclei are usually large with distinct chromatin network, while superficial cell nuclei are small and pyknotic [112]. This is also evident in Fig. 6.2, where the nucleus in (c) is smaller compared to the nuclei in (a) and (b), and the image appears darker indicating a denser internal composition.

As Fig. 6.2 demonstrates, CIN 3 nuclei are significantly larger than normal nuclei. Normal nuclei appear rounder, whereas CIN 3 nuclei are asymmetric and appear darker. The relative intensity changes are attributed to the differences in DNA content, and regions with higher DNA content appear darker on images. Nuclei in (d) – (f) also show coarse chromatin clumping and condensation, while the nuclei in (a) – (c) have a more homogeneous chromatin distribution.

The nuclear feature statistics that will be used in FDTD modeling can be divided into two different groups. The first group is related to nuclear morphology, and includes information about nuclear size and nuclear shape. The second group provides statistics about DNA content, chromatin organization, and chromatin texture that collectively describe the dielectric properties of the nuclei.

#### *6.2.1.1 Nuclear Morphology Statistics*

The features that are used to describe nuclear morphology include nuclear area, mean radius, maximum radius, and eccentricity. Nuclear morphology features for each nucleus have been calculated by the in-house image analysis system.

### *6.2.1.2 DNA Content and Chromatin Texture Statistics*

Feulgen-Thionin is stoichiometric for DNA. Therefore, the DNA content, and thus the average refractive index, of a nucleus can be assumed to be directly related to the average pixel intensity in an image. Chromatin texture can be described in terms of the magnitude of refractive index fluctuations that correspond to the variations in pixel intensity, and the spatial frequency of refractive index fluctuations that corresponds to the size of chromatin clumps present.

DNA content and chromatin texture statistics have been calculated by analyzing a subset of nuclear images provided. The total number of nuclei analyzed in each diagnostic category was 60. To extrapolate the average pixel intensity in an image to the mean refractive index $n$, a conversion factor was required. As a starting point, it was first assumed that the mean refractive index of a normal nucleus was 1.39 [113-115], and that of a CIN 3 nucleus was 1.42 [13, 21, 22, 45], independent of the layer. This assumption provided a scale factor to find a relation between change in pixel intensity and the corresponding change in absolute refractive index. The natural logarithm of the pixel intensity averaged over all the normal nuclei images was assumed to be proportional to 1.39, and the natural logarithm of the pixel intensity averaged over all the CIN 3 nuclei images was assumed to be proportional to 1.42. Then, by calculating the average pixel intensity for nuclei in different layers, a unique refractive index value was assigned to nuclei in each layer. The magnitude of refractive index fluctuations, $\Delta n$, was calculated by observing the intensity variations over images.

To find the size of the largest chromatin clumps, and thus the minimum spatial frequency of refractive index fluctuations characterizing each nucleus, a two-dimensional Fast Fourier Transform (FFT) was performed on each image and the resulting spatial frequency components dominating the spectrum were analyzed.

### 6.2.2 Cell Construction in FDTD Modeling

Cervical epithelial cells have a low fraction of mitochondria, and the main contribution to cellular scattering comes from the nucleus [98, 116]. Therefore, FDTD simulations described will model the cervical cells as heterogeneous nuclei embedded in homogeneous cytoplasm. This approach also has the advantage of isolating the effects of nuclear morphology and chromatin organization on light scattering.

Results from quantitative histopathology provided all the parameters related to nuclear morphology and dielectric properties necessary to construct a heterogeneous nucleus in an FDTD grid. First, an ellipsoid nucleus was created and every point inside the ellipsoid was assigned a constant refractive index value. The dimensions were based on the mean radius, maximum radius, and the eccentricity. To create the refractive index variations inside the nucleus, small cubes with refractive index in the range $n \pm \Delta n$ were placed randomly throughout the ellipsoid. The purpose of using cubes as opposed to other three-dimensional structures was to simplify the algorithm for placing non-overlapping heterogeneities within the FDTD grid. The size of the cubes was selected randomly from an interval. The lower size limit was 0.34 μm, which corresponded to the resolution of the nuclear images provided. The upper limit on the cube size was given by the size of the largest chromatin clump present.

### 6.2.3 FDTD Simulation Parameters

The FDTD simulations for cervical cell nuclei were performed at a vacuum wavelength of λ=1064 nm. This wavelength was chosen so that the results would be applicable to imaging techniques such as RCM, OCT, and OCM. The refractive index of the cytoplasm was set to 1.36 [13, 113-115], and the FDTD grid spacing used was 1/20 of the wavelength inside the cytoplasm. After a cell nucleus was constructed in the FDTD grid, the computational domain was extended to enable implementation of the PML boundary condition, but the memory required for each simulation did not exceed 2 Gb, allowing the computations to be carried out on a PC.

A total of eighteen simulations were carried out. Nine of these simulations were for normal nuclei and the other nine were for CIN 3 nuclei. The nuclear parameters were chosen such that for each diagnostic category there were three basal/parabasal nuclei simulations, three intermediate nuclei simulations, and three superficial nuclei simulations. For each different simulation representing these six different categories, the simulation parameters were randomly selected from the acceptable ranges calculated through quantitative histopathologic analysis.

## 6.3 RESULTS

### 6.3.1 Quantitative Histopathology Results

Table 6.1 shows the average and the standard deviation of parameters that describe nuclear morphology.

Table 6.1: Nuclear morphology statistics for normal and CIN 3 nuclei.

| Layer | Number of nuclei analyzed | Nuclear area ($\mu m^2$) | Mean radius ($\mu m$) | Maximum radius ($\mu m$) | Eccentricity |
|---|---|---|---|---|---|
| Normal | | | | | |
| Basal/parabasal | 326 | 36.36 ± 12.60 | 3.24 ± 0.61 | 4.02 ± 0.80 | 1.46 ± 0.34 |
| Intermediate | 203 | 40.06 ± 7.59 | 3.43 ± 0.34 | 4.24 ± 0.48 | 1.42 ± 0.25 |
| Superficial | 33 | 25.80 ± 5.37 | 2.80 ± 0.28 | 3.97 ± 0.60 | 2.07 ± 0.70 |
| CIN 3 | | | | | |
| Basal/parabasal | 569 | 51.74 ± 22.47 | 3.94 ± 2.60 | 5.41 ± 1.33 | 1.88 ± 0.63 |
| Intermediate | 416 | 56.88 ± 20.32 | 4.10 ± 2.14 | 5.26 ± 1.03 | 1.54 ± 0.37 |
| Superficial | 84 | 43.90 ± 16.19 | 3.70 ± 2.19 | 5.38 ± 1.34 | 2.13 ± 0.68 |

As Table 6.1 demonstrates, nuclear area, mean radius, maximum radius, and eccentricity all increase with dysplasia. In most cases, the relative standard deviation values of CIN 3 parameters are greater indicating nuclear pleomorphism, a well-known characteristic of dysplasia.

Table 6.2 shows the computed averages for the mean refractive index *n*, the largest chromatin clump size and the corresponding minimum spatial frequency. The range given for the magnitude of the refractive index fluctuations, *Δn*, corresponds to the extreme intensity variations in a specific layer.

Table 6.2: Dielectric properties of normal and CIN 3 nuclei.

| Layer | Number of nuclei analyzed | n | Δn | Largest chromatin clump size (μm) | Minimum spatial frequency ($\mu m^{-1}$) |
|---|---|---|---|---|---|
| Normal | | | | | |
| Basal/parabasal | 20 | 1.387 | ± (0.004 - 0.007) | 1.02 | 0.98 |
| Intermediate | 20 | 1.372 | ± (0.004 - 0.006) | 0.85 | 1.18 |
| Superficial | 20 | 1.414 | ± (0.005 - 0.008) | 0.85 | 1.18 |
| CIN 3 | | | | | |
| Basal/parabasal | 20 | 1.426 | ± (0.008 - 0.010) | 1.36 | 0.74 |
| Intermediate | 20 | 1.404 | ± (0.007 - 0.009) | 1.02 | 0.98 |
| Superficial | 20 | 1.431 | ± (0.008 - 0.011) | 1.19 | 0.84 |

Table 6.2 demonstrates that *n* increases for CIN 3 nuclei indicating elevated DNA content. The refractive index fluctuations *Δn* are also higher corresponding to increased heterogeneity. Larger chromatin clumps associated with CIN 3 are also evidenced in Table 6.2.

### 6.3.2 FDTD Simulation Results

#### *6.3.2.1 Scattering Patterns*

Figure 6.3 shows the scattering patterns obtained from (a) the basal/parabasal nuclei simulations, (b) the intermediate nuclei simulations, and (c) the superficial nuclei simulations. All of the scattering patterns have been averaged over the azimuthal angle so that they are functions of the scattering angle only. The blue curves in Fig. 6.3 represent the results for the normal nuclei, and the red curves represent the results for the CIN 3 nuclei. The angular resolution for the scattering angle is $1^o$, and the scattering intensity is given in arbitrary units.

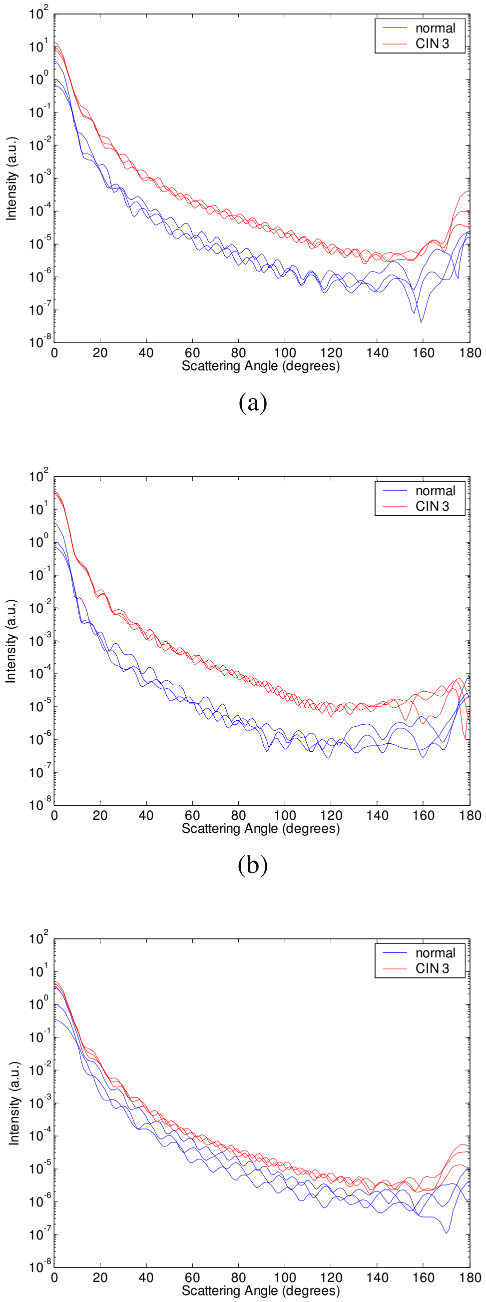

(a)

(b)

(c)

Figure 6.3: Scattering patterns of (a) basal/parabasal, (b) intermediate, and (c) superficial, nuclei. Three simulation results are shown for each diagnostic category.

Figure 6.3 shows that for basal/parabasal and superficial cell nuclei, the intensity of scattered light is higher for CIN 3 nuclei for all scattering angles. For intermediate cell nuclei, however, the intensity is higher for CIN 3 nuclei for up to about 175°, but for angles very close to 180°, the intensity of light scattered from normal nuclei is usually higher. The figure also demonstrates that the variation in the scattering patterns of nuclei belonging to the same diagnostic category is generally greater for normal nuclei, although the standard deviations in the simulation parameters are greater for CIN 3 nuclei. This can be attributed to the fact that CIN 3 nuclei are larger in size, they have higher refractive indices, and they are more heterogeneous. Therefore, the intensity maxima and minima in their scattering patterns are not very pronounced, resulting in relatively less varied intensity distributions.

Figure 6.4 shows the scattering patterns averaged over three different simulation results.

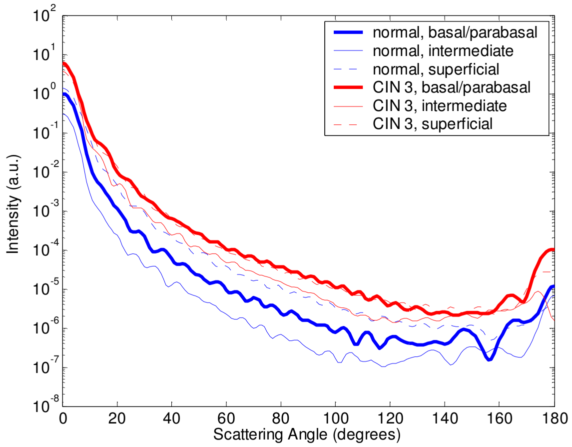

Figure 6.4: Averaged scattering patterns.

The most significant differences between normal and CIN 3 nuclei are for the intermediate layer, whereas the superficial layer has the smallest intensity differences.

### *6.3.2.2 Scattering Phase Functions*

A scattering phase function is obtained by normalizing the scattering pattern such that its integral over the solid angle equals one. Figure 6.5 shows the phase functions corresponding to the scattering patterns in Fig. 6.4.

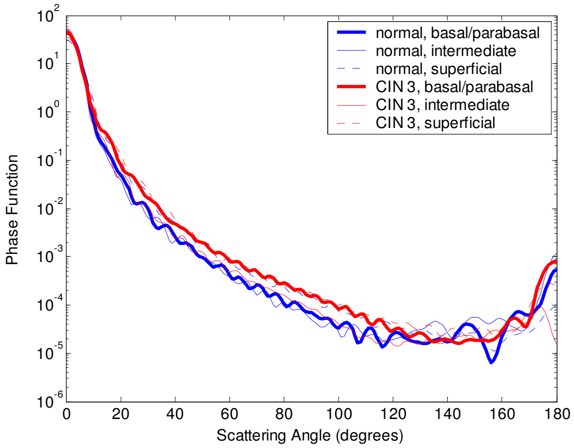

Figure 6.5: Phase functions.

As Fig. 6.5 demonstrates, the overall shape of the phase functions are very similar for small angles, but differences start to appear after about 120°. This is especially true for the intermediate and superficial cell nuclei. For angles greater than 120°, scattering from a normal intermediate nucleus is more probable than scattering from a CIN 3 intermediate nucleus. For angles greater than 150°, the scattering probability for a CIN 3 superficial nucleus exceeds the scattering probability for a normal superficial nucleus.

### *6.3.2.3 Calculation of Scattering Cross-sections*

The scattering cross-sections have been calculated for all the nuclei simulated. Figure 6.6 shows the computed averages of the scattering cross-section values for the normal and CIN 3 nuclei in basal/parabasal, intermediate, and superficial layers.

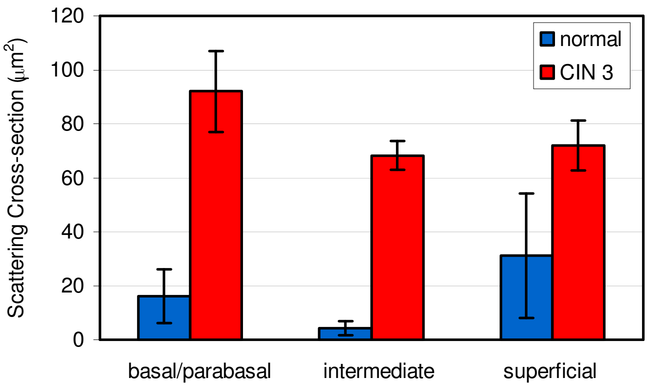

Figure 6.6: Scattering cross-sections for normal and CIN 3 nuclei in basal/parabasal, intermediate, and superficial layers.

The scattering cross-sections are significantly greater for CIN 3 nuclei. For both diagnostic categories, intermediate nuclei have the smallest cross-section.

#### *6.3.2.4 Integration of Scattering Patterns over High Angles*

Most of the optical diagnostic techniques under development mainly depend on the measurement of backscattered light. An understanding of the high-angle scattering properties of cells is essential in interpreting images obtained with RCM, OCT, and OCM. Extraction of morphological information using spectroscopic techniques also necessitates a quantitative understanding of high-angle scattering. Moreover, differences in scattering properties of dysplastic cells relative to normal cells are expected to be enhanced for backscattering geometries since most of the changes associated with dysplasia potentially modulate high-angle scattering. For example, high-angle scattering has been shown to be sensitive to DNA content [107].

To assess the differences in scattered light collected in optical imaging techniques, such as in RCM, OCT, or OCM, the scattering patterns can be integrated over high angles to estimate the overall changes in collected light intensity. Assuming a numerical aperture of about 0.8 for the collection optics, the region of interest in the scattering patterns of Fig. 6.3 is the angular range $140^o$-$180^o$. Figure 6.7 compares the scattering intensities integrated over this range.

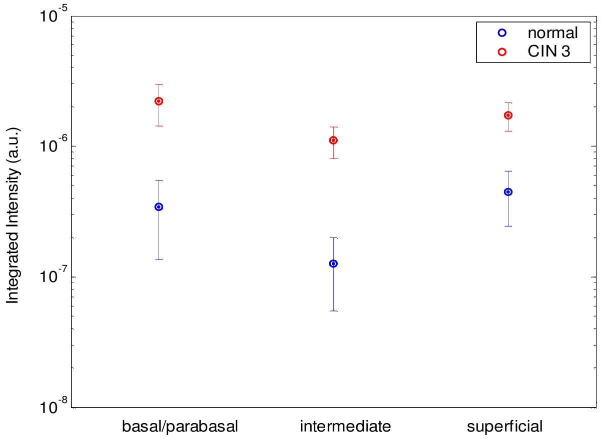

Figure 6.7: Integrated scattering patterns over the angular range 140°-180°.

The elevation of integrated intensity for CIN 3 nuclei is evident in Fig. 6.7. This elevation is about an order of magnitude for the basal/parabasal and intermediate layers, whereas it is relatively smaller for the superficial layer.

## 6.4 DISCUSSION

FDTD simulation results show that there are significant differences in the scattering properties of normal and CIN 3 cervical cell nuclei. Results also validate the importance of treating cell nuclei at different epithelial depths separately since scattering properties vary from layer to layer, especially in normal epithelium.

In this work, quantitative histopathology proved to be a suitable way to define nuclear morphology and dielectric structure specific to each different epithelial layer, and also to quantify dysplastic changes in nuclei. This provided realistic input for FDTD modeling. It is important to note, however, that the calculation of refractive index values presented in Table 6.2 did not consider any possible effect of acetic acid applied to the cervical tissue before biopsy removal. Acetic acid can potentially alter the refractive index profile of nuclei, and assessment of its effect is a current research topic.

The scattering patterns in Fig. 6.4 indicate that changes associated with dysplasia generally lead to increased scattering. The increase in scattering intensity for CIN 3 nuclei at small scattering angles is due to an increase in nuclear size. High-angle scattering is sensitive to nuclear refractive index profile. Since CIN 3 nuclei are more heterogeneous, the increase in scattering intensity at high angles is also expected. Figure 6.4 shows that basal/parabasal and superficial nuclei follow this trend. Intermediate nuclei also follow this trend up to about $175^o$, but the backscattered light intensity for CIN 3 nuclei drops to below that of normal nuclei. A possible reason for this behavior is that the mean refractive index for normal intermediate nuclei is very close to that of cytoplasm, as shown in Table 6.2. Therefore, any heterogeneities introduced into the nucleus can lead to dramatic increase in backscattered light. This is also evident in Fig. 6.4 that shows that the averaged scattering pattern for normal intermediate nuclei has the most prominent peak at $180^o$.

The phase functions in Fig. 6.5 demonstrate that the greatest differences in the scattering probabilities of normal and CIN 3 nuclei tend to occur for high angles. Since high-angle scattering from nuclei is expected to be more sensitive to internal structure rather than the overall size and the mean refractive index, the enhancement of differences for high angle scattering probabilities is a significant result in terms of the possibility of probing the chromatin texture and organization of nuclei in different diagnostic categories.

Figure 6.6 shows that the nuclei in the intermediate layer have the smallest scattering cross-section and that basal/parabasal layer cross-section is greater than that of the intermediate layer. This scattering trend has been observed in confocal images of cervical tissue. As an illustration, Fig. 6.8 shows confocal images of (a) basal/parabasal (300 μm below the surface), (b) intermediate (150 μm below the surface), and (c) superficial layers (50 μm below the surface) of *ex vivo* normal cervical epithelium. The measured lateral and axial resolution of the confocal system used are 0.8 μm and 2-3 μm, respectively [98].

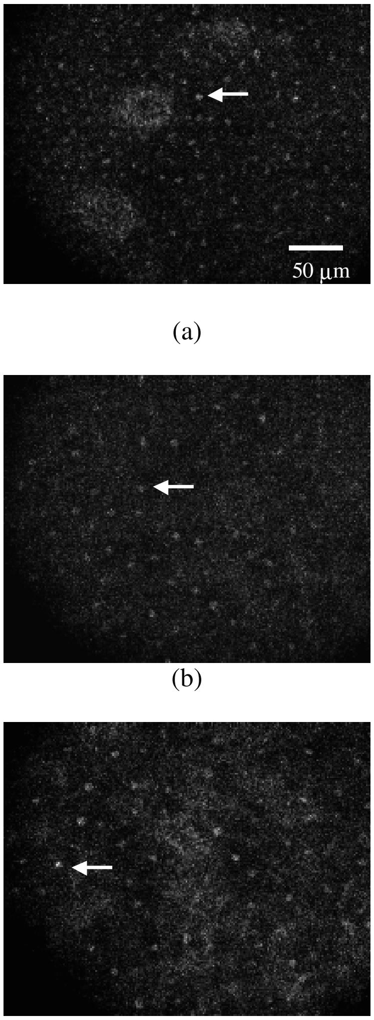

(a)

(b)

(c)

Figure 6.8: Confocal images of (a) basal/parabasal, (b) intermediate, and (c) superficial, layers of a normal cervical epithelium. The arrows point to nuclei.

The nuclei observed in the images demonstrate that scattering decreases in going from the superficial layer to the intermediate layer, but then increases in the basal/parabasal layer. Note that the confocal system operates at a wavelength of 810 nm and the images have been acquired after the application of acetic acid

[98], but scattering from nuclei follows the general trend observed in Fig. 6.6. The interpretation of confocal images can more appropriately be made by considering the integrated intensity values of Fig. 6.7, since confocal microscopy basically provides a map of integrated high angle scattering from nuclei. Figure 6.9 compares the gray scale values obtained from confocal images to the integrated scattering intensities shown in Fig. 6.7. The gray scale values given for each layer have been calculated by recording pixel intensities (0-255) from ten different locations representing nuclear areas on the images. The standard deviations of these pixel intensities are also shown. The figure demonstrates good correlation between change in pixel intensities from one layer to another and the corresponding change in integrated scattering intensities.

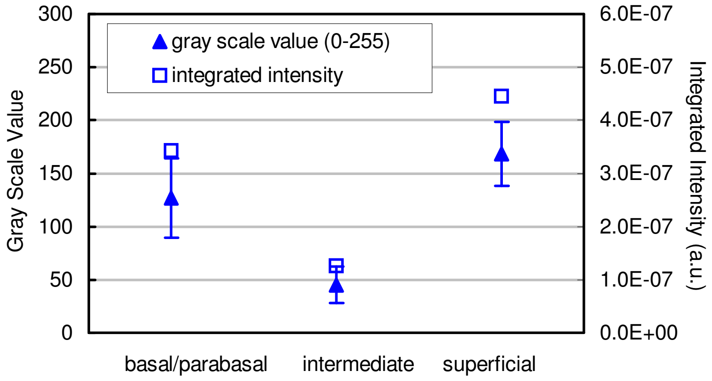

Figure 6.9: Comparison of the gray scale values from confocal images of normal cervical tissue to the integrated scattering intensities from Fig. 6.7.

An overall increase in scattering from dysplastic cell nuclei is evidenced in the calculated cross-section values, whereas Fig. 6.7 specifically shows the elevation of high-angle scattering. Increased high-angle scattering from tumorigenic cells has been previously reported by Mourant et al. [107, 117], who carried out angle-dependent light scattering measurements on tumorigenic and nontumorigenic rat embryo fibroblasts. Also, increase in backscattered light intensity has been noted in a study by Pan et al. [118] involving the use of OCT imaging for detection of tumorigenesis in rat bladders. Finally, confocal images of cervical biopsies presented in papers by Collier et al. [98] and Drezek et al. [116] also showed elevated scattering from dysplastic cell nuclei, consistent with the FDTD modeling results.

## 6.5 CONCLUSIONS

The goal of the research described in this chapter was to use FDTD modeling to analyze the light scattering properties of normal and dysplastic cervical cells at different epithelial depths. The results provide an improved understanding of the relationship between morphological and biochemical structure of cells and light scattering.

Since the FDTD method provides a flexible approach to simulate light scattering from arbitrarily inhomogeneous structures, its use is not restricted to analysis of cells. The method can be used to investigate the light scattering properties of other microscopic tissue constituents. The next chapter will focus on analyzing light scattering from collagen fiber meshes, with the ultimate goal of providing an improved understanding of the micro-optical properties of the stromal layer beneath the epithelium.

# Chapter 7: FDTD Modeling of Light Scattering from Collagen Fiber Meshes and Trends in Micro-Optical Properties of Normal and Cancerous Stroma

## 7.1 INTRODUCTION

Epithelial cell nuclei are the main scattering centers in the epithelium, and FDTD modeling results presented in the previous chapter can be used to better interpret tissue spectra obtained with scattering-based optical spectroscopic techniques that are emerging as potential tools for detection of pre-cancerous changes in epithelial tissues. Results from FDTD simulations also provide important insights into intrinsic optical contrast observed in images obtained using reflectance confocal microscopy (RCM), optical coherence tomography (OCT), and optical coherence microscopy (OCM), which are promising new optical imaging technologies for detection of epithelial pre-cancer.

Collagen fibers are the main scatterers in the stroma underlying the epithelium, but little is known about their scattering properties. Due to the high refractive index and fibrous nature of collagen fibers, scattering in the stroma is much higher compared to scattering in the epithelial layer. Stromal scattering contributes significantly to spectroscopic reflectance signals acquired from epithelial tissues. Therefore, characterization of stromal scattering is necessary to better interpret spectral signatures or to develop more reliable computational models to describe light transport in epithelial tissues. As described in *Chapter 5*, extensive efforts have recently been made to optimize design of fiber-optic probes or to develop techniques and algorithms in order to separate spectroscopic signatures from different tissue layers. These efforts are likely to benefit from a more comprehensive understanding of stromal scattering. Further, previous studies indicate that the collagen matrix degrades as dysplasia develops [14-17]. Structural changes resulting from decomposition of collagen fibers can lead to changes in stromal scattering [6, 9]. Thus, there may be clinically relevant information in optical signals from the stroma. Analysis of the scattering characteristics of collagen fibers may be an important step towards depicting a more complete picture of dysplastic changes in optical properties of epithelial tissues. From an imaging perspective, the penetration depth achievable with RCM is usually limited to the epithelial layer, but modalities such as OCT and OCM are capable of probing the stromal layer. Two-dimensional, multispectral imaging systems are also sensitive to stromal optical properties. Any optical contrast resulting from differences in scattering properties of normal and dysplastic stroma can be used as an additional diagnostic measure.

The number of studies analyzing the scattering properties of collagen fibers is very limited. This is partly due to the lack of available information about specific morphology, structure, and orientation of fibers constituting the collagen matrix. Freund et al. [119] studied the effects of fibril orientation on light scattering in the cornea by treating the fibrils as parallel finite-length cylinders. Since collagen fibrils in the corneal stroma have a highly regular spatial arrangement, assumption of aligned cylindrical scatterers is justified. Saidi et al. [120] modeled scattering by collagen fibers in neonatal skin using two-dimensional cylindrical Mie theory. In this study, the fibers were assumed to be infinitely long cylinders that ran parallel to the tissue surface. Organization of the collagen matrix and orientation of collagen fibers in the matrix can vary significantly for different tissue types. Stroma beneath the epithelia lining the internal surfaces of the body is characterized by collagen fibers that are randomly oriented and intricately interlaced [121, 122]. In these tissues, collagen fibers are not unidirectional and can have extremely irregular alignment. Description of these fibers as simple cylindrical scatterers may be an oversimplification. Since the FDTD method does not put any limitations on the scattering structure to be simulated, it provides a flexible approach to study scattering from randomly oriented and interlaced collagen fibers. In such cases, however, it is extremely difficult to quantify the length, diameter, or orientation of fibers, and to create realistic three-dimensional models for light scattering analysis.

Histological staining and electron microscopy have been widely used to observe and study the structural properties of collagen fibers [121-123], but these techniques only provide two-dimensional information and are not adequate for visualization of fibers in three dimensions. In addition, fixation and dehydration associated with histological analysis or electron microscopy are likely to affect the organization and volume fraction of fibers in the stroma. A more suitable approach to study the complex nature of the fibrous meshes created by collagen fibers has been proposed in a recent study by Wu et al. [124] that describes extraction of structural information about fibers in a collagen gel from optical sections acquired using a reflectance confocal microscope. An image processing algorithm developed in conjunction with confocal imaging is used to create surface-rendered images of the collagen gel, enabling three-dimensional visualization. Collagen is a well-known source of autofluorescence and nonlinear emission [125, 126]. Therefore, other techniques that have the potential to enable three-dimensional structural visualization of collagen fibers involve fluorescence confocal microscopy, multi-photon microscopy and second-harmonic generation imaging, all of which can provide high contrast and optical sectioning capabilities [126-128].

This chapter describes the use of the implemented FDTD algorithm described in *Chapter 3* to model light scattering from collagen fiber meshes. To create realistic collagen mesh models, optical sections from the stroma of normal and abnormal oral cavity biopsy samples have been acquired using fluorescence confocal microscopy. These optical sections provide realistic input for construction of three-dimensional collagen meshes. FDTD modeling is then used to analyze the intensity and angular distribution of light scattered from the constructed fiber meshes, and to establish trends for cancerous changes in stromal scattering properties.

## 7.2 METHODS

### 7.2.1 Biopsy Collection and Confocal Imaging of Fresh Tissue Slices

Clinically normal and abnormal oral cavity biopsy pairs were obtained, with informed consent, from patients at The University of Texas M.D. Anderson Cancer Center. Biopsies remained in chilled tissue culture medium until they were sectioned into 200 μm thick transverse tissue slices with a Krumdieck tissue slicer. Each tissue slice was imaged with a Leica SP2 AOBS confocal laser-scanning fluorescence microscope equipped with a 40×, 1.25 NA oil immersion objective. Optical stacks were obtained from the stromal part of the tissue slices, within 200 μm below the basement membrane. The excitation wavelength used was in the UV range (351-364 nm) with detection set from 380 nm to 550 nm. At this excitation wavelength, stromal fluorescence is mainly attributed to collagen [125, 129], enabling visualization of collagen fibers. Lateral pixel size was set to 0.732 μm, and an axial step size of 1 μm was used to optically section the tissue samples. Each optical stack included 8-10 optical sections, corresponding to a total depth of 8-10 μm. Since the diameter of the collagen fibers is expected to be on the order of several μm [121, 122], such a resolution level is considered to be sufficient for image analysis. Note that reflectance imaging can also be used to obtain structural information about the stroma, but fluorescence images tend to provide a better visualization of fibers due to characteristic collagen autofluorescence.

### 7.2.2 Image Processing for Segmentation of Collagen Fibers and Construction of Collagen Fiber Meshes for FDTD Modeling

I have implemented an image processing algorithm in Matlab that can be used to segment out collagen fibers from a series of optical sections and to construct a three-dimensional collagen fiber mesh for direct input into the FDTD computational grid. The first step was to determine a region of interest in a confocal image. The selected region of interest corresponded to an area of 8 μm × 8 μm. Eight consecutive optical sections corresponding to the same lateral position were used to create a volume of interest with a size of 8 μm × 8 μm × 8 μm. The second step of the algorithm involved interpolation of the selected optical sections to represent the volume of interest with a finer grid size. As described in *Chapter 3*, FDTD modeling requires that the grid spacing for the computational domain be less than a given upper limit. Therefore, resampling the original volume of interest was necessary to satisfy this threshold and ensure the stability of the computations. Interpolation was first carried out in the lateral direction, and then in the axial direction. In both cases, cubic splines were used to interpolate the original pixel intensity values. Next, each interpolated optical section was processed to segment out the collagen fibers. Segmentation was performed using a clustering algorithm. Fuzzy c-means clustering [130] was used to reduce the number of gray levels to two and to create a binary representation of the three-dimensional grid. In this binary representation, a voxel value of 0 indicates the outside medium surrounding the collagen fibers, and a voxel value of 1 indicates collagen. Implementing a clustering algorithm provided a simple, efficient means of segmenting out collagen fibers in the three-dimensional grid and eliminated the necessity to resort to threshold-based processing, which would require manual intervention.

The algorithm was applied to confocal image stacks obtained from two pairs of clinically normal and abnormal tongue biopsies. Four meshes were constructed from each biopsy by sampling different areas on the confocal images. Therefore, a total of sixteen (eight normal and eight abnormal) collagen fiber meshes were available for FDTD simulations.

### 7.2.3 Characterization of Collagen Fiber Meshes

#### *7.2.3.1 Volume Fraction of Collagen Fibers*

Volume fraction is defined to be the fraction of the computational grid occupied by collagen fibers. This parameter is easy to compute since each collagen fiber mesh can be described by a binary intensity function $I(x, y, z)$, which represents the occupation state of each voxel or grid cell in the computational domain at the coordinates $(x, y, z)$.

#### *7.2.3.2 Spatial Organization of Collagen Fibers*

In addition to the fraction of the computational grid occupied by the collagen fibers, we need a metric to describe the texture of the collagen meshes constructed. Since stromal collagen fibers are characterized by random spatial orientation, a suitable approach to characterize three-dimensional texture is to use statistical features. Haralick features are widely used in the field of biomedical imaging to characterize natural textures and are computed based on co-occurrence matrices [131, 132]. These matrices describe the frequency of occurrence of pixel pairs with specified intensity levels. A co-occurrence matrix, $C_d(i, j)$, is a matrix where the $(i, j)$th element represents the frequency of occurrence of two neighboring pixels in the direction $d$ with gray levels $i$ and $j$. For binary images, where $i$ and $j$ can only assume the values 0 and 1, the co-occurrence matrix will have four entries. Since collagen fiber meshes are described by volumetric grid data, we can compute co-occurrence matrices separately for the three dimensions.

If *I(x, y, z)* represents the grid data where a voxel value of 0 indicates outside medium, and a voxel value of 1 indicates collagen, the co-occurrence matrices for the *x*, *y*, and *z* directions are defined by

$$\begin{aligned} C_x(i, j) &= \text{number of voxels with } I(x, y, z) = i \text{ and } I(x+1, y, z) = j, \\ C_y(i, j) &= \text{number of voxels with } I(x, y, z) = i \text{ and } I(x, y+1, z) = j, \\ C_z(i, j) &= \text{number of voxels with } I(x, y, z) = i \text{ and } I(x, y, z+1) = j, \end{aligned} \tag{7.1}$$

with $i, j \in \{0, 1\}$.

The matrices in Equation (7.1) are generally normalized to express the matrix entries as probability measures. Normalized co-occurrence matrices are given by

$$\hat{C}_{x,y,z}(i, j) = \frac{C_{x,y,z}(i, j)}{\sum_i \sum_j C_{x,y,z}(i, j)}. \tag{7.2}$$

It is possible to define many different texture features using the normalized co-occurrence matrices. Two features that can be computed to characterize the collagen meshes created are generally referred to as contrast and correlation. These parameters are defined as [131, 132]

$$contrast_{x,y,z} = \sum_i \sum_j (i - j)^2 . \hat{C}_{x,y,z}(i, j), \tag{7.3}$$

and

$$correlation_{x,y,z} = \sum_i \sum_j (i - \bar{I})(j - \bar{I}) . \hat{C}_{x,y,z}(i, j), \tag{7.4}$$

where $\overline{I}$ is the mean intensity and is equal to the volume fraction due to the binary representation of the three-dimensional structure in question. Since contrast depends on the difference of $i$ and $j$, this parameter is expected to assume large values when the three-dimensional structure has frequent intensity transitions from 0 to 1, or from 1 to 0. A large value for correlation indicates that the three-dimensional structure has large connected subcomponents.

Contrast and correlation values for the $x$, $y$, and $z$ dimensions have been calculated separately for each of the sixteen collagen fiber meshes created. These values are expected to provide some insight into the three-dimensional organization of the collagen fibers.

### 7.2.4 FDTD Simulation Parameters

The FDTD simulations for the collagen fiber meshes created have been performed at a vacuum wavelength of $\lambda$=1064 nm, for a plane wave traveling in the $z$ direction. This wavelength was chosen so that the results would, as in the previous chapter, be applicable to imaging techniques such as RCM, OCT, and OCM. The refractive index of the outside medium was set to 1.35 [115]. Grid cells corresponding to collagen fibers were assigned refractive indices that were randomly selected from the range 1.40-1.45 [115]. The FDTD grid spacing used was 1/20 of the wavelength in the outside medium. This grid spacing is commonly employed in FDTD modeling, and was preset during the interpolation step of the algorithm used to create the collagen fiber meshes. The size of each mesh was 8 μm × 8 μm × 8 μm, corresponding to about 210 × 210 × 210 grid cells. The computational domain was extended to enable implementation of the PML boundary condition, but the memory required for each simulation did not exceed 2 Gb, allowing the computations to be carried out on a PC.

## 7.3 RESULTS

### 7.3.1 Confocal Imaging of Fresh Tissue Slices

Figure 7.1 shows confocal images of tissue slices from a clinically normal and a clinically abnormal biopsy pair used in this study. The top parts of the images are roughly parallel to the basement membrane and hence to the tissue surface. Collagen fibers can be identified due to their bright autofluorescence.

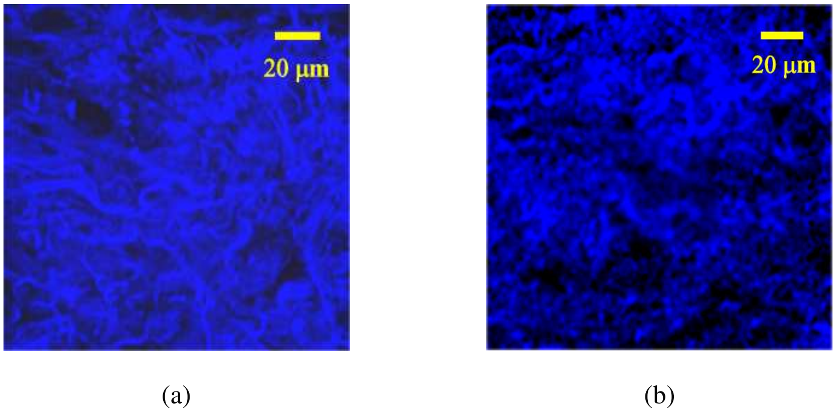

(a) (b)

Figure 7.1: Confocal images of (a) clinically normal, and (b) clinically abnormal biopsy pair. Collagen fibers are visible due to autofluorescence.

Note that the stroma of the normal tissue is characterized by dense collagen fibers [Fig. 7.1(a)], whereas the stroma of the abnormal tissue is less dense and appears less structured [Fig. 7.1(b)]. The tissue sections imaged in this study were later submitted for histopathologic analysis. The abnormal sections were classified as squamous cell carcinoma (SCC).

### 7.3.2 Constructed Collagen Fiber Meshes for FDTD Modeling

Figure 7.2 provides a step-by-step illustration of the image processing algorithm used to construct three-dimensional collagen fiber meshes by showing the results for a particular image set after each intermediate step. In the figure, the $x$ and $z$ coordinates define the lateral image plane, and the $y$ coordinate defines the axial direction. The three optical sections shown in Fig. 7.2(b) and Fig. 7.2(c) are from different depths within the imaged tissue sample and correspond to the images on the top, in the middle, and at the bottom of the image stack. To give a better insight into the three-dimensional organization of the fibers, Figure 7.2(d) presents an isosurface-rendered representation of the collagen mesh created from the image stack.

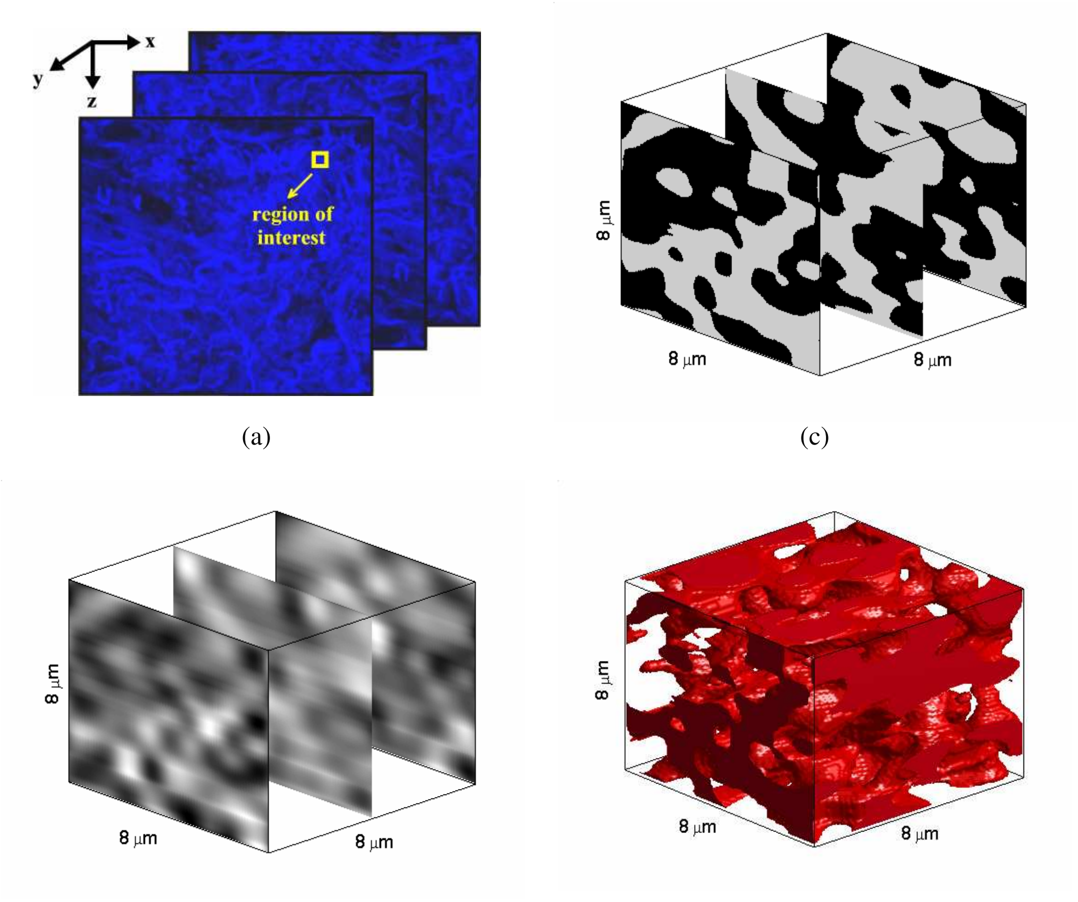

(a) (c)

(b) (d)

Figure 7.2: Construction of a three-dimensional collagen fiber mesh from a series of optical sections. (a) Selection of a region of interest in the original confocal image set, followed by (b) interpolation using cubic splines and (c) segmentation of collagen fibers through fuzzy c-means clustering. An isosurface-rendered representation of the collagen fiber mesh is shown in (d).

Figure 7.2 demonstrates the random and irregular alignment of collagen fibers in the stroma, which is especially evident in Fig. 7.2(d). It is hard to quantify the organizational tendencies of the collagen fibers, validating the necessity to resort to statistical features to distinguish structural differences.

Table 7.1 shows the parameters that have been computed to characterize the collagen meshes constructed. The table lists the values averaged over four meshes corresponding to each biopsy and the associated standard deviations. Contrast and correlation values given represent averages over the *x*, *y*, and *z* dimensions. No specific trend was observed when the three directions were considered separately, suggesting no directional preference for collagen fiber organization.

Table 7.1: Parameters for characterization of collagen fiber meshes.

| Biopsy | Volume Fraction | Contrast | Correlation |
|---|---|---|---|
| Patient 1 | | | |
| Normal | 0.48 ± 0.01 | 0.020 ± 0.001 | 0.239 ± 0.001 |
| Abnormal | 0.40 ± 0.04 | 0.021 ± 0.002 | 0.227 ± 0.010 |
| Patient 2 | | | |
| Normal | 0.49 ± 0.02 | 0.021 ± 0.002 | 0.239 ± 0.001 |
| Abnormal | 0.39 ± 0.04 | 0.019 ± 0.002 | 0.227 ± 0.009 |

Table 7.1 demonstrates that the volume fraction of collagen fibers for the abnormal biopsies is lower compared to the volume fraction for the normal biopsies, and the difference is about 20% in both cases. The standard deviation values for the volume fractions are also higher for the abnormal biopsies, indicating more variability. Despite no observable trend for the contrast values, there are significant differences between the correlation values for the normal and the abnormal biopsies. Collagen fiber meshes constructed from the abnormal

biopsies have lower correlation values compared to the collagen meshes constructed from the normal biopsies. Lower correlation values suggest increased disorder in three-dimensional organization of the collagen fibers. As in the case of the volume fraction, the standard deviation values are higher for the abnormal cases.

To elucidate any interdependence among volume fraction, contrast, and correlation, Figure 7.3 shows scatter plots of these parameters calculated for each of the collagen meshes created. Scatter plots of contrast versus volume fraction, correlation versus volume fraction, and correlation versus contrast are shown in Figs. 7.3(a), 7.3(b), and 7.3(c), respectively.

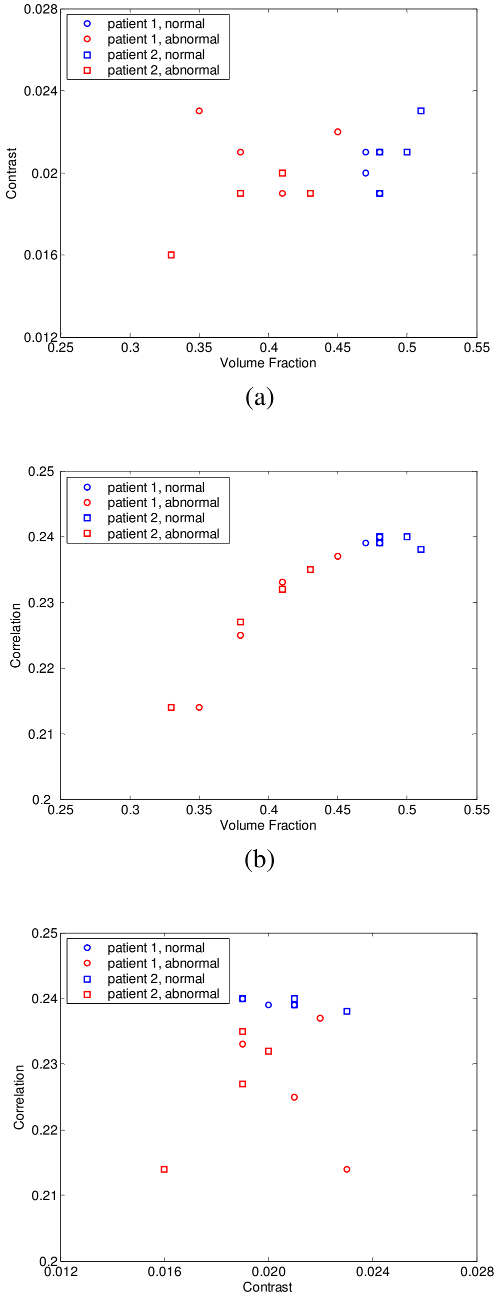

(a)

(b)

(c)

Figure 7.3: Scatter plots of (a) contrast versus volume fraction, (b) correlation versus volume fraction, and (c) correlation versus contrast.

Figure 7.3 further illustrates that the parameters that provide the best separation between normal and abnormal cases are the volume fraction and the correlation. The trend shown in Fig. 7.3(b) indicates that volume fraction and correlation are not independent, and correlation increases with increasing volume fraction. The relative rate of increase in correlation is higher for small volume fractions.

### 7.3.3 FDTD Simulation Results

#### *7.3.3.1 Scattering Patterns*

Figure 7.4 shows the scattering patterns obtained from the FDTD simulations. The scattering patterns of the collagen fiber meshes corresponding to the first patient are shown in Fig. 7.4(a), and the scattering patterns for the collagen fiber meshes corresponding to the second patient are shown in Fig. 7.4(b). All of the scattering patterns were averaged over the azimuthal angle so that they were functions of the scattering angle only. The blue curves in Fig. 7.4 represent the results for the normal collagen fiber meshes, and the red curves represent the results for the abnormal collagen fiber meshes. The angular resolution for the scattering angle is $1^{o}$, and the scattering intensity is given in arbitrary units.

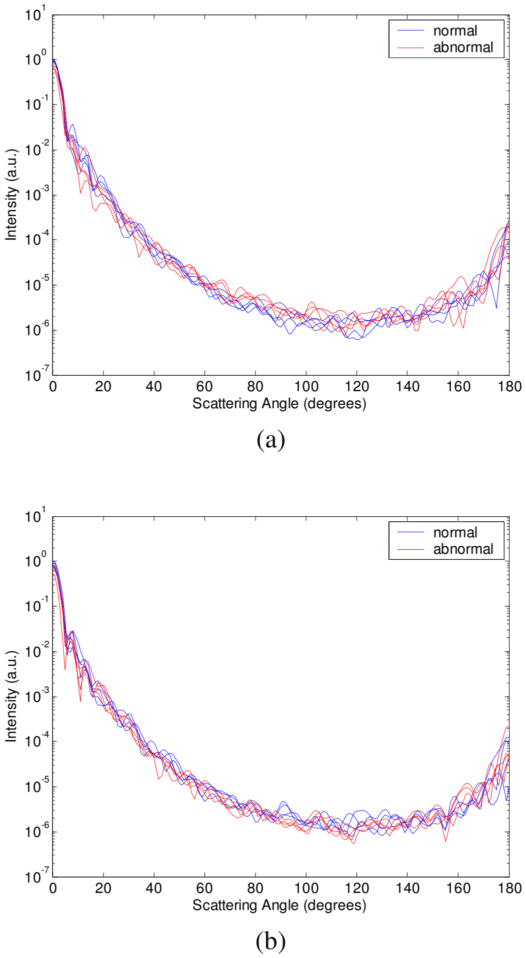

Figure 7.4: Scattering patterns of collagen fiber meshes for (a) patient 1, and (b) patient 2. The results of all sixteen simulations are shown.

Figure 7.4 shows that the scattering patterns of all the collagen fiber meshes created have similar shape. They are highly peaked in the forward direction, and the scattering intensity covers a dynamic range of about six orders of magnitude.

Figure 7.5 shows the scattering patterns averaged over four meshes corresponding to each biopsy. Figure 7.5(a) shows the scattering patterns over the angular range $0^{o}$-$180^{o}$. Figure 7.5(b) zooms in on the scattering patterns for $0^{o}$-$40^{o}$ to enhance intensity differences for small scattering angles, and Fig. 7.5(b) zooms in on the scattering patterns for $140^{o}$-$180^{o}$ to show differences in high-angle scattering.

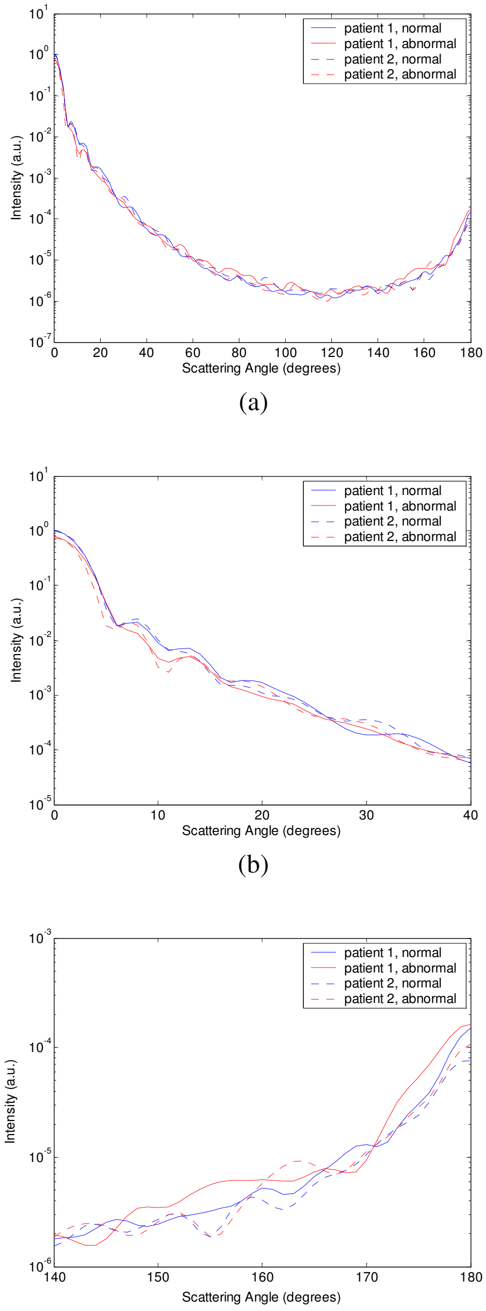

(a)

(b)

(c)

Figure 7.5: Averaged scattering patterns for (a) 0°-180°, (b) 0°-40°, and (c) 140°-180°. The results for the two patients are shown separately.

It is evident in Fig. 7.5(b) that the intensity of light scattered in the forward direction is higher for the normal meshes. The intensity for small scattering angles decreases in the case of abnormal meshes. On the other hand, Fig. 7.5(c) shows that for a given patient, the intensity of high-angle scattering tends to be higher for the abnormal meshes.

Figure 7.6 combines the scattering patterns shown in Fig. 7.5(a) by averaging the intensity values corresponding to each diagnostic category. This figure characterizes the angle-dependent scattering properties of normal versus abnormal collagen fiber meshes.

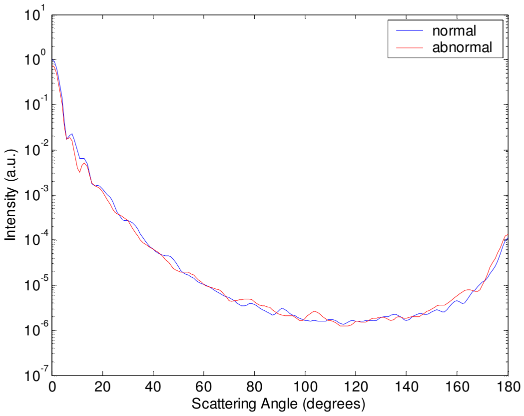

Figure 7.6: Averaged scattering patterns for normal and abnormal collagen fiber meshes.

Figure 7.6 shows that differences in the scattering patterns of normal and abnormal collagen fiber meshes are rather subtle. The overall trend indicates that forward scattering is higher for the normal meshes, whereas backscattering is higher for the abnormal meshes.

#### *7.3.3.2 Scattering Phase Functions*

A scattering phase function is obtained by normalizing the scattering pattern so that its integral over the solid angle equals one. Figure 7.7 shows the phase functions corresponding to the scattering patterns in Fig. 7.5. As in the case of Fig. 7.5, the phase functions for the angular range $0^o$-$180^o$ are shown in Fig. 7.7(a). Figures 7.7(b) and 7.7(c) zoom in on regions of small-angle and high-angle scattering, respectively.

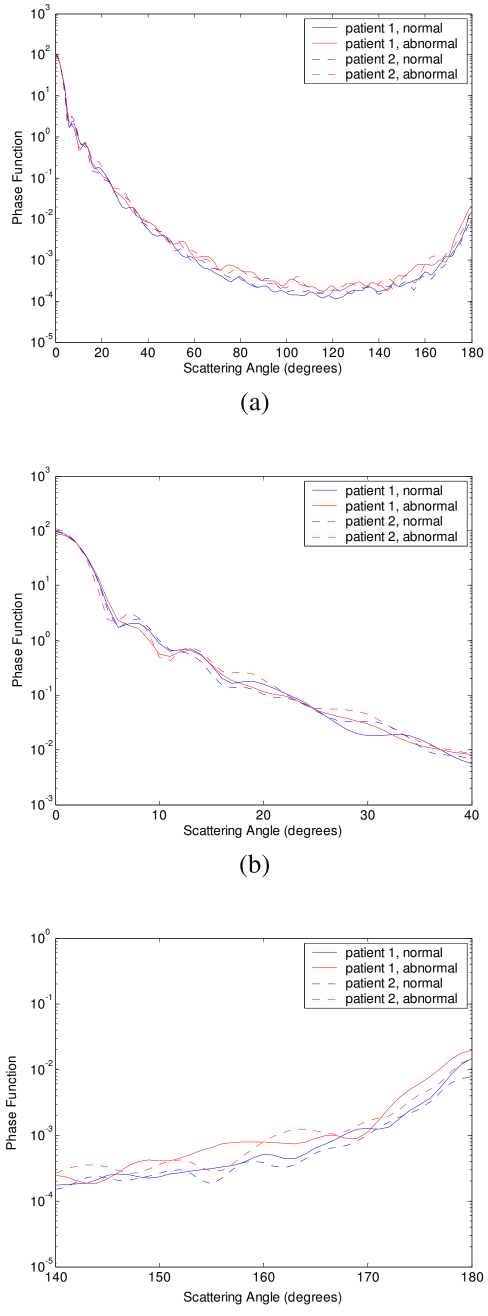

(a)

(b)

(c)

Figure 7.7: Phase functions for (a) $0^o$-$180^o$, (b) $0^o$-$40^o$, and (c) $140^o$-$180^o$. The results for the two patients are shown separately.

As Fig. 7.7(a) demonstrates, the overall shapes of the phase functions are very similar for small scattering angles. For angles greater than about 40°, however, scattering from abnormal collagen fiber meshes is more probable than scattering from normal collagen fiber meshes. Figures 7.7(b) and 7.7(c) further illustrate that there are no significant differences in small-angle scattering probabilities for normal and abnormal meshes, but high-angle scattering probabilities are greater for the abnormal meshes. This is also evident in Fig. 7.8, which presents the phase functions averaged over each diagnostic category.

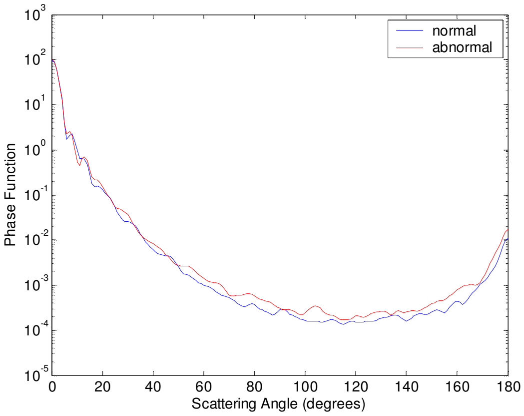

Figure 7.8: Averaged phase functions for normal and abnormal collagen fiber meshes.

### *7.3.3.3 Calculation of Scattering Cross-Sections*

The scattering cross-sections have been calculated for all the collagen fiber meshes simulated. Figure 7.9 shows the averages of the scattering cross-section values for normal and abnormal meshes corresponding to each biopsy.

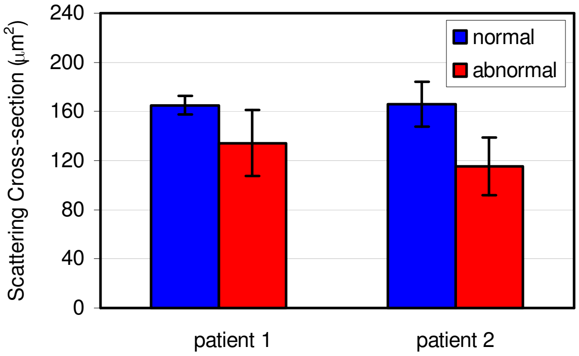

Figure 7.9: Scattering cross-sections for normal and abnormal collagen fiber meshes. The results for the two patients are shown separately.

The scattering cross-section values are greater for the normal meshes. For the first patient, the average cross-section for the abnormal meshes is about 20% smaller than the average cross-section for the normal meshes. For the second patient, the difference is about 30%.

### *7.3.3.4 Trends in High-Angle Scattering Properties*

Optical imaging techniques such as RCM, OCT, and OCM are sensitive to high-angle scattering properties of tissue constituents. Assuming a numerical aperture of about 0.8 for the collection optics, scattering over the angular range $140^o$-$180^o$ is of particular interest. To assess any differences in scattered light collected with these imaging techniques, the scattering patterns shown in Fig. 7.4 can be integrated over this angular range. Figure 7.10 illustrates the high-angle scattering properties of the collagen meshes simulated. Figure 7.10(a) shows the scattering intensities integrated over $140^o$-$180^o$. To highlight the differences in relative high-angle scattering probabilities of normal and abnormal collagen fiber meshes, Figure 7.10(b) shows the phase functions integrated over the same angular range.

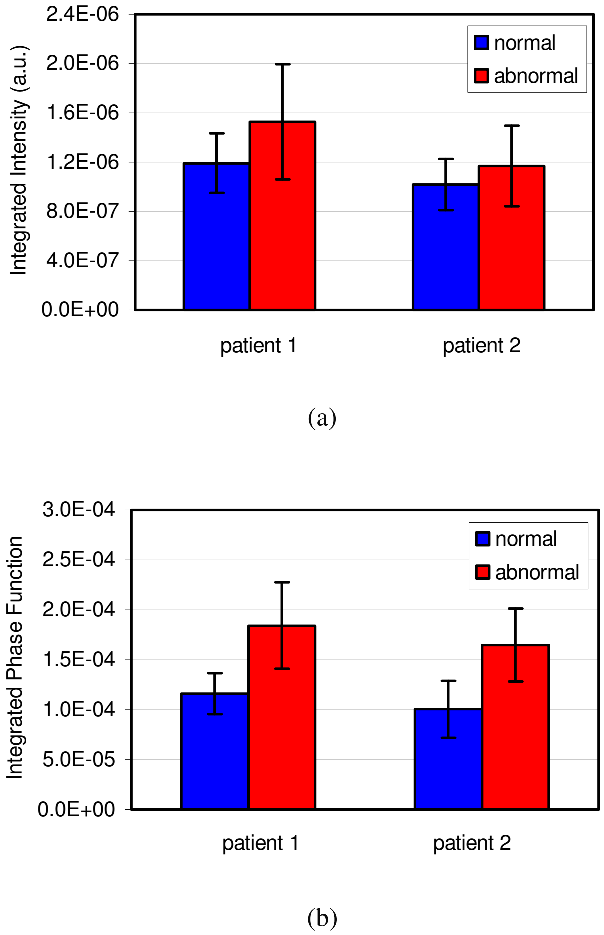

Figure 7.10: High-angle scattering properties of normal and abnormal collagen meshes. (a) Scattering intensities and (b) phase functions, both integrated over the angular range 140°-180°. The results for the two patients are shown separately.

Integrated scattering intensities tend to be higher for the abnormal meshes, but the relative standard deviation values associated with the averages shown in Fig. 7.10(a) indicate that there can be extensive variability among meshes from the same biopsy. Therefore, the differences in integrated scattering intensities for the normal and the abnormal collagen fiber meshes are not significant. The differences in integrated phase functions shown in Fig. 7.10(b), however, are significant. For the first patient, the average high-angle scattering probability for the abnormal meshes is about 50% higher compared to the normal meshes. For the second patient, the difference is about 70%. Increased high-angle scattering probabilities for the abnormal meshes are consistent with the trends observed in Fig. 7.7.

#### *7.3.3.5 Influence of Volume Fraction and Spatial Organization of Collagen Fibers on the Scattering Properties of Collagen Fiber Meshes*

The scatter plots in Figs. 7.11 and 7.12 provide an explicit connection between the volume fraction and spatial organization of collagen fibers, and the computed scattering properties of the collagen fiber meshes. Figure 7.11 illustrates the dependence of scattering cross-section on volume fraction, contrast, and correlation.

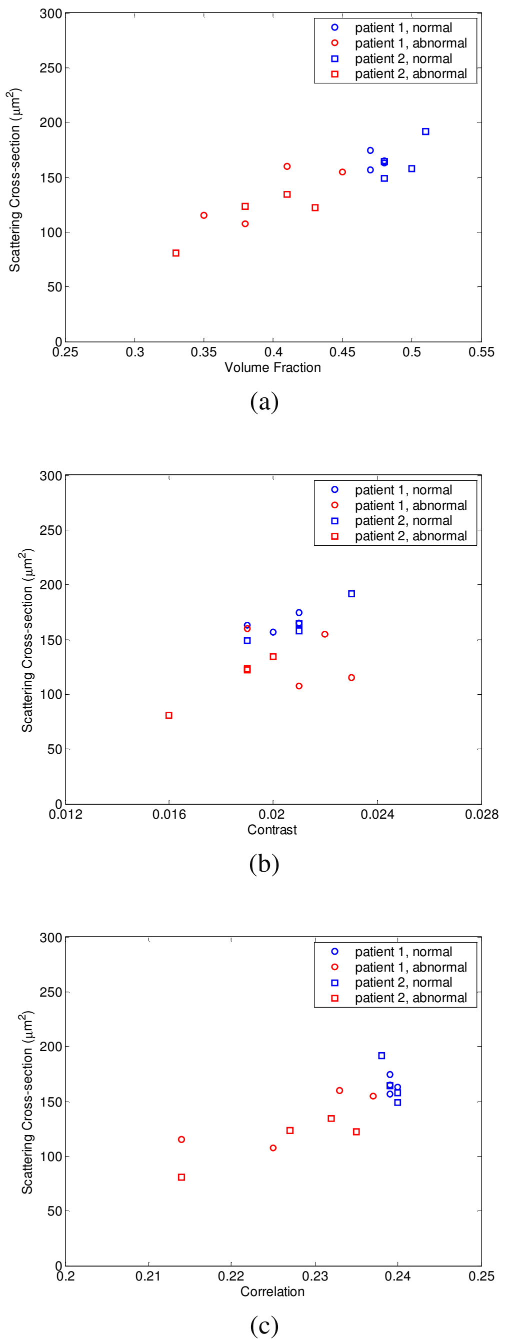

(a)

(b)

(c)

Figure 7.11: Dependence of scattering cross-section on (a) volume fraction, (b) contrast, and (c) correlation.

Figure 7.11 demonstrates that scattering cross-section is highly correlated to volume fraction of collagen fibers and increases with increasing volume fraction. There is also good separation between normal and abnormal cases. There is no particular trend for the contrast values, but scattering cross-section is also highly dependent on correlation with good separation between normal and abnormal cases.

Figure 7.12 focuses on the high-angle scattering properties of the meshes and shows the dependence of scattering intensity and phase function, both integrated over $140^o$-$180^o$, on the same structural parameters as in Fig. 7.11.

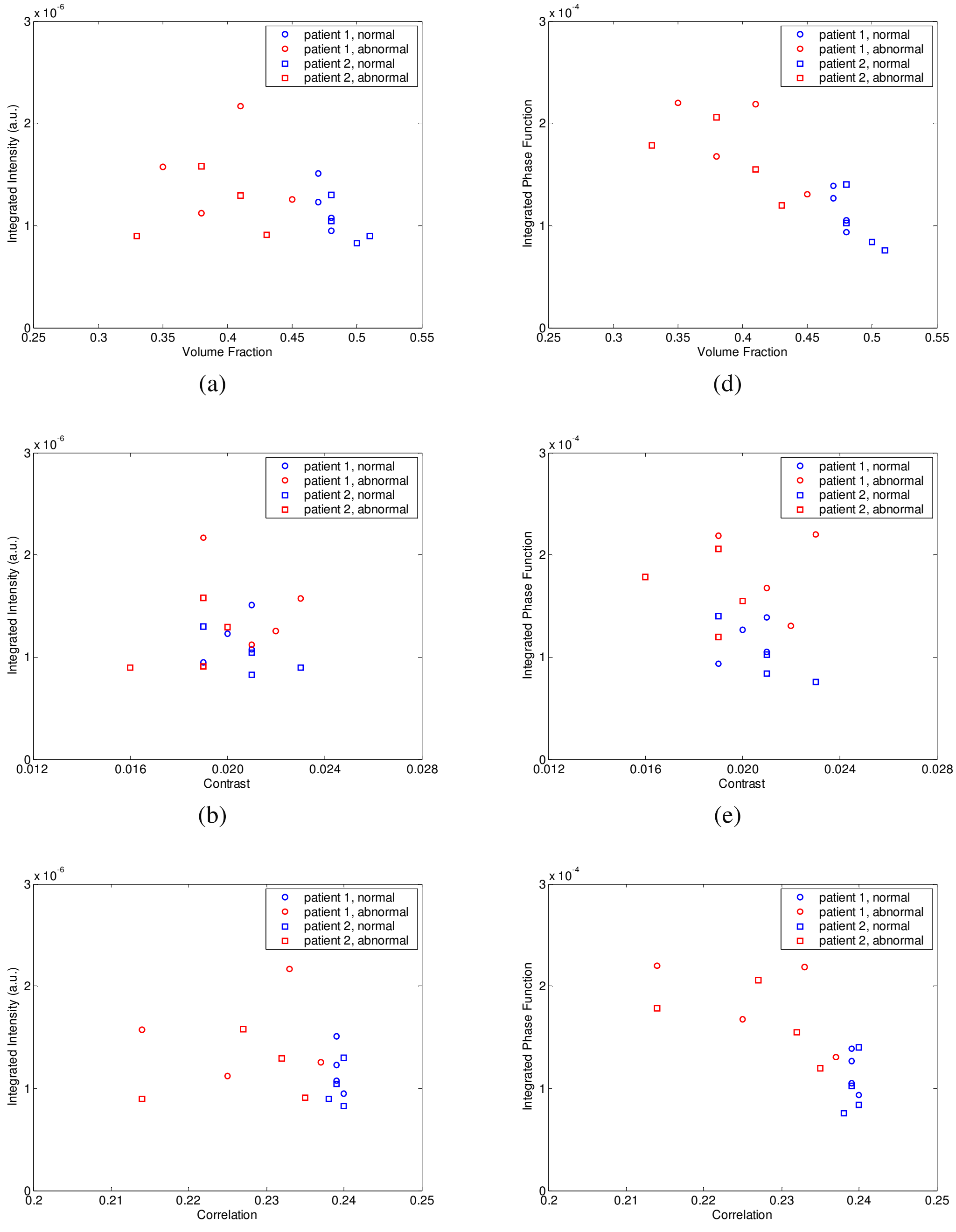

(a) (d)

(b) (e)

(c) (f)

Figure 7.12: Dependence of scattering intensity and phase function, both integrated over 140°-180°, on (a, d) volume fraction, (b, e) contrast, and (c, f) correlation.

Results shown in Fig. 7.12 indicate that integrated scattering intensity has no apparent dependence on volume fraction, contrast, or correlation. Integrated phase function, on the other hand, is highly correlated to volume fraction and decreases as volume fraction increases. Note that this trend is opposite to that observed for the cross-section, which increases with increasing volume fraction. Integrated phase function also tends to assume lower values as correlation increases.

## 7.4 DISCUSSION

### 7.4.1 Trends in Structural Properties of Normal and Abnormal Collagen Fiber Meshes

Most of the studies analyzing morphological, structural, and architectural changes that accompany development of epithelial pre-cancer have mostly focused on the epithelium. Dysplastic changes in epithelial cells, including increased nuclear size and irregular chromatin clumping, have been well-documented, and extraction of such nuclear features from optical signals obtained using scattering-based imaging and spectroscopic techniques has been of great interest. Atypical features in epithelial cells constitute one of the major pathological trademarks of pre-invasive cancer [84], and extraction of these features from optical signals provides a basis to assess the diagnostic performance of optical technologies by directly comparing the results to routine histologic findings.

It is believed that cancer progression is also accompanied by mechanisms that lead to remodeling of the stroma and hence structural variations in the collagen matrix [14, 15, 126]. The autofluorescence images shown in Fig. 7.1 illustrate typical differences between normal and abnormal stroma. Collagen matrix of the normal stroma has a more regular structural organization, whereas the matrix of the abnormal stroma appears loose and degraded. Collagen fibers in the abnormal stroma have a more disorganized appearance in the sense that they are shorter and more detached from each other, and they also have an irregular aggregation tendency. These characteristics are consistent with autofluorescence patterns observed in stroma of normal and abnormal epithelial tissue [16, 17].

The parameters given in Table 1 quantify structural and organizational tendencies of collagen fibers. The results confirm that volume fraction of collagen fibers in the stroma tends to decrease with cancer progression. Statistical features computed provide some insight into organization of fibers in the collagen matrix. Although shorter and more disconnected fibers in the case of abnormal stroma would intuitively suggest increased contrast, the results shown in Table 1 and Fig. 7.3 imply no such trend. This can be explained by the fact that although degradation of fibers may result in a greater number of fiber segments, this does not automatically lead to more frequent intensity transitions in the images. Extra space created between fiber segments can be regarded as additional constant intensity regions that negate the effect of intensity transitions brought about by fiber breakdown. Therefore, contrast may not have the potential to reveal structural differences in the stroma. Correlation values for normal and abnormal meshes, on the other hand, are significantly different. Correlation is consistently lower for the abnormal collagen fiber meshes. It is important to note that correlation values increase with increasing volume fraction, as evidenced in Fig. 7.3(b). This, however, does not imply that decreased correlation for abnormal meshes is necessarily a result of decreased volume fraction. Definition of correlation in Equation 7.4 ensures that decreased volume fraction does not always lead to decrease in correlation, and it is entirely possible for a three-dimensional structure to have a smaller volume fraction and yet a higher correlation value. Thus, interdependence of volume fraction and correlation is a characteristic of the collagen fiber meshes created, and decrease in both of these parameters simultaneously suggests that loss of collagen with cancer progression is accompanied by increased disorder.

The three-dimensional structural parameters presented in this work were based on confocal image stacks of tissue slices from only two patients. To prove that these parameters were representative of typical stroma, I have performed image analysis on confocal images of paired oral cavity biopsies from five additional patients diagnosed with SCC or invasive cancer. These images were acquired prior to this study, and optical stacks were not available for three-dimensional analysis. Instead, the image processing algorithm was applied in two dimensions. In accordance with the three-dimensional analysis, four regions of interest were selected from each confocal image, resulting in a total of forty (twenty normal and twenty abnormal) 8 μm × 8 μm image segments. Two-dimensional image analysis showed that the averaged occupation fraction of collagen fibers was 0.49 ± 0.02 for the normal biopsies and 0.40 ± 0.03 for the abnormal biopsies. The contrast values were again comparable for both diagnostic categories, the average being 0.023 ± 0.003 for the normal cases and 0.022 ± 0.002 for the abnormal cases. Finally, the average correlation was 0.237 ± 0.002 for the normal biopsies and 0.226 ± 0.006 for the abnormal biopsies. All of these values obtained from two-dimensional image analysis were very close those presented in Table 7.1. Note also that the additional biopsy pairs were from different oral cavity sites including the floor of the mouth, retromolar trigone, and the tongue. This indicates that the three-dimensional collagen fiber meshes used for FDTD simulations were valid models characterizing typical stromal organization.

### 7.4.2 Light Scattering Properties of Normal and Abnormal Collagen Fiber Meshes

FDTD simulation results indicate that cancerous changes in stromal collagen matrix lead to decreased small-angle scattering. This is especially evident from the scattering patterns shown in Fig. 7.5. The scattering cross-sections in Fig. 7.9 characterize the overall strength of scattering from the collagen fiber meshes created. For highly forward scattering structures, scattering cross-sections are dominated by the small-angle scattering intensities. Therefore, the fact that abnormal meshes have smaller cross-sections is a manifestation of decreased small-angle scattering intensities.

The phase functions in Fig. 7.7 and Fig. 7.8 show that for angles greater than $40^o$, scattering is more probable in the case of abnormal meshes. Integrated phase functions in Fig. 7.10 further verify this observation for the angular range $140^o$-$180^o$.

Scatter plots in Fig. 7.11 demonstrate that volume fraction and correlation strongly influence scattering cross-section. Decreased scattering cross-section with progression of cancer is a direct consequence of decreased volume fraction and correlation. Figure 7.12, on the other hand, illustrates that decrease in these parameters has the opposite effect on high-angle scattering probabilities. Integrated phase functions, however, appear to have a stronger dependence on volume fraction than on correlation. Note that since volume fraction and correlation are interdependent, it is not possible to deconvolve the effects of these two structural parameters and make independent conclusions about their exclusive influence on scattering properties of collagen meshes.

Scattering cross-sections computed in the previous chapter for epithelial cell nuclei were on the order of 20 $\mu m^2$ for normal cells and 80 $\mu m^2$ for dysplastic cells. Comparison of the scattering cross-sections in Fig. 7.9 to these values reveals the highly scattering nature of collagen fiber meshes. Especially for normal tissue, the scattering strength of collagen meshes is about eight times the scattering strength of epithelial cell nuclei. This result is consistent with significant differences observed in scattering coefficients reported in *Chapter 4* for epithelial and stromal layers of normal tissue.

Decrease in overall scattering from collagen fiber meshes brought about by cancer progression and the corresponding increase in high-angle scattering probability have important implications for diagnostic optical imaging and spectroscopy. Differences in scattering properties of normal and abnormal collagen matrix need to be taken into account when developing models of light propagation through the stromal layer, or when analyzing optical signals acquired from epithelial tissues.

It is important to note that the study presented here involved structural information extracted from cancerous tissue samples. The question that remains to be answered is whether there are analogous changes in dysplastic or pre-cancerous tissues. Similar analysis needs to be carried out for pre-cancerous epithelial tissue samples. Results of such an analysis can delineate any dysplastic changes in structural properties of stromal collagen matrix and the corresponding alterations in stromal scattering properties.

## 7.5 CONCLUSIONS

Cancer progression in epithelial tissues is accompanied by structural and morphological changes in the stromal collagen matrix. Analysis of the influence of these changes on stromal scattering properties can improve our ability to extract diagnostic information from optical signals. Since collagen fibers in the matrix form an extremely intricate mesh, analysis of the light scattering properties of these fibers is challenging. The goal of the research presented in this chapter was to use FDTD modeling to establish a relationship between structural properties of collagen fiber meshes and light scattering. This work provides further evidence that FDTD modeling can be an invaluable computational tool in the field of biomedical optics as it can be applied to scattering problems that involve extremely heterogeneous structures.

FDTD modeling results presented here and in the previous chapter serve to further our understanding of the micro-optical properties of epithelial tissues. Analysis of the influence of pre-cancerous or cancerous changes on scattering properties of tissue constituents can provide guidelines for development and assessment of optical technologies for cancer screening and diagnosis.

# Chapter 8: Conclusions

## 8.1 SUMMARY AND CONTRIBUTIONS

Optical diagnostic techniques have the potential to improve early detection of pre-cancerous changes in tissues. Morphological, structural, and biochemical changes associated with dysplastic progression can be effectively monitored using optical spectroscopy and imaging, since these changes give rise to intrinsic contrast in optical signals. Optical techniques can be implemented in real time without the need for biopsy removal, and are expected to have major impact in clinical practice and patient care.

This dissertation described a series of modeling studies aimed at establishing an improved understanding of reflectance properties of normal and pre-cancerous epithelial tissues, with the ultimate goal of revealing the potential of reflectance-based optical diagnosis of epithelial pre-cancer. Specific contributions of the research presented in this dissertation involve:

- Implementation of a Monte Carlo code that facilitates analysis of spectroscopic reflectance measurements from multi-layered tissues. The code provides sufficient flexibility to enable simulation of sophisticated fiber-optic probe geometries that can be implemented for *in vivo* signal acquisition.
- Implementation of a three-dimensional Finite-Difference Time-Domain (FDTD) code that uses the perfectly matched layer boundary condition

and enables numerical solution of light scattering problems involving microscopic tissue constituents.

- Application of Monte Carlo modeling to establish a quantitative understanding of optical contrast observed in spatially resolved reflectance spectra of normal and pre-cancerous epithelial tissues.
- Application of Monte Carlo modeling to provide guidelines for design and optimization of fiber-optic probes that can enhance diagnostic potential of *in vivo* reflectance spectroscopy.
- Application of FDTD modeling to study the micro-optical properties of epithelial tissues. Analysis of the light scattering properties of microscopic tissue constituents such as epithelial cell nuclei and collagen fibers provides an improved understanding of how pre-cancerous changes alter light propagation in tissues.

A brief description of Monte Carlo modeling was given in *Chapter 2*. The implemented Monte Carlo code provided the computational framework necessary to carry out simulations on the bulk tissue level. Analysis of light propagation at the microscopic tissue level entails the use of computational electromagnetics. The implementation of the FDTD method, which is one of the most popular computational techniques for solution of scattering problems, was described in detail in *Chapter 3*. Incorporation of the perfectly matched layer (PML) boundary condition to terminate the FDTD computational domain increased the dynamic range of FDTD modeling to a level required to study scattering from structures with biologically relevant sizes and refractive indices. This was a significant improvement over the previous FDTD implementation by our group, where artificial reflections due to less efficient boundary conditions led to over-prediction of high-angle scattering by up to two or even three orders of magnitude.

The goal of the research described in *Chapter 4* was to carry out Monte Carlo modeling studies to explain the differences observed in spatially resolved reflectance spectra of normal and dysplastic cervical tissue. Predictions from simulations agree well with trends that characterize *in vivo* measurements and provide important insights into how the combined effects of increased epithelial scattering, increased stromal absorption, and decreased stromal scattering can reproduce spectral differences observed in reflectance measurements from dysplastic cervix. Results from this study can facilitate development of analytical photon propagation models that enable inverse estimation of diagnostically relevant optical parameters from *in vivo* reflectance measurements. Simulation results also demonstrate that the clinical fiber-optic probe geometry currently in use is mostly sensitive to optical properties of the highly scattering stroma and cannot be used to probe the weakly scattering epithelial layer.

Fiber-optic probes that selectively collect scattered light from both the epithelium and the underlying stroma are likely to improve diagnostic performance of *in vivo* reflectance spectroscopy by revealing diagnostic features unique to each layer. In *Chapter 5*, I presented Monte Carlo models to evaluate fiber-optic probe geometries with respect to sampling depth and depth resolution.

Based on the simulation results, I propose a probe design that utilizes half-ball lens coupled source and detector fibers to isolate epithelial scattering from stromal scattering and hence to resolve spectral information from the two layers. The proposed probe is extremely compact and can provide easy access to different organ sites. The computational models described in this chapter have helped our group design a novel fiber-optic probe to record spectroscopic signals from epithelial tissues. Clinical trials are currently underway to test the use of this novel probe for optical diagnosis of pre-cancer in the oral cavity.

The research described in the rest of the dissertation was targeted towards establishing a better understanding of the micro-optical properties of normal and dysplastic epithelial tissues. In *Chapter 6*, I used FDTD modeling to investigate differences in angle-dependent scattering properties of normal and dysplastic cervical cells. Specifically, the scattering patterns and phase functions have been computed for normal and dysplastic cervical cells at three different epithelial depths, namely basal/parabasal, intermediate, and superficial. Construction of cervical cells within the FDTD computational grid was based on morphological and chromatin texture features obtained from quantitative histopathology. Results show that angle-dependent scattering characteristics are different not only for normal and dysplastic cells but also for cells at different epithelial depths. The calculated scattering cross-sections are significantly greater for dysplastic cells. The scattering cross-sections of cells at different depths indicate that scattering decreases in going from the superficial layer to the intermediate layer, but then increases in the basal/parabasal layer. Increased scattering from dysplastic cervical cells and a layer-to-layer variation in epithelial scattering properties are consistent with trends observed in confocal images of *ex vivo* cervical tissue.

The goal of the research presented in *Chapter 7* was to use FDTD modeling to analyze light scattering from collagen fiber meshes. To create realistic collagen mesh models, optical sections from stromal part of normal and abnormal oral cavity biopsy samples have been acquired using fluorescence confocal microscopy. These optical sections provided realistic input for construction of three-dimensional collagen meshes. FDTD modeling results show that abnormal meshes have smaller scattering cross-sections compared to the normal meshes. Phase functions computed indicate that high-angle scattering probabilities tend to be higher for abnormal meshes. These results provide invaluable insights into the micro-optical properties of normal and cancerous stroma.

In conclusion, the modeling studies presented in this dissertation provide a framework to meaningfully interpret optical signals obtained from epithelial tissues and to optimize design of optical sensors for *in vivo* reflectance measurements. Computational analysis of the scattering properties of microscopic tissue constituents serves to further our understanding of how pre-cancerous changes alter light propagation in different tissue layers, giving rise to intrinsic optical contrast. The results obtained throughout this research will have significant impact in the field of biomedical optical spectroscopy and imaging, and will benefit researchers targeting early, noninvasive diagnosis of pre-invasive cancerous changes in epithelial tissues.

## 8.2 FUTURE RESEARCH DIRECTIONS

Modeling studies play an integral role in technology development and assessment, and the field of biomedical optics is no exception. The research described in this dissertation provides extensive evidence that numerical and computational analysis of light propagation in tissues facilitates development and optimization of optical diagnostic techniques. In this section, I briefly discuss several possible future research directions that are mainly natural extensions of the modeling work described in the previous chapters.

The research studies presented in *Chapter 6* and *Chapter 7* demonstrate that FDTD modeling provides a flexible computational approach to study micro-optical properties of tissues. A fundamental issue with any computational study is that it is crucial to generate realistic and relevant model input. In *Chapter 6*, quantitative histopathology was used to define nuclear morphology and dielectric structure, and to quantify dysplastic changes in cell nuclei. In *Chapter 7*, fluorescence confocal microscopy was used to create realistic collagen fiber mesh models for FDTD input. It is important to note, however, that alternative imaging techniques that provide higher resolution can be used in conjunction with FDTD modeling to investigate the effect of finer structural details on light scattering properties of microscopic tissue constituents.

Results in *Chapter 6* demonstrate that scattering properties of the epithelium is depth dependent, and scattering decreases in going from the superficial layer to the intermediate layer, but then increases in the basal layer.

Such a trend can significantly affect the overall spectral response, especially when reflectance measurements are obtained using fiber-optic probe geometries that can provide enhanced sensitivity to the epithelial layer. The influence of this layer-to-layer variation can be investigated by modeling the epithelium as a three-layer medium.

In this work, Monte Carlo modeling has been used to simulate photon propagation on the bulk tissue level, whereas FDTD modeling has been employed to study light scattering at the microscopic level. These two modeling schemes can be combined into a hybrid algorithm that allows sampling of scattering directions from phase functions obtained using the FDTD method. As described in *Chapter 2*, Monte Carlo modeling of photon transport in tissues is generally performed using the Henyey-Greenstein phase functions, which approximate the scattering patterns calculated by Mie theory for homogeneous spherical scatterers. This approximation may not be valid for complex phase functions of cells in the epithelium or collagen fibers in the stroma. The phase functions can significantly affect the Monte Carlo results depending on the source-detector geometry in question [133, 134]. Therefore, incorporation of FDTD phase functions into Monte Carlo modeling can provide a more realistic assessment of tissue reflectance.

An important issue in implementing a hybrid Monte Carlo and FDTD algorithm is how to relate the scattering cross-sections computed using the FDTD method to bulk scattering coefficients of different tissue layers. If the spatial distribution of the scatterers in the tissue is discrete and the number density of these scatterers is low, the effects of multiple scattering will be negligible. In this case, the scattering coefficient can be computed by multiplying the scattering cross-section of a single scatterer by the number density [135]. This may be a valid assumption for cell nuclei that are discretely distributed in the epithelium. In dysplastic tissue, however, the density of nuclei in the epithelium increases and the validity of ignoring multiple scattering effects becomes questionable. The situation is even more complicated in the stroma. Since the scattering centers in the stroma are collagen fibers that are characterized by intricate spatial organization, conversion of scattering cross-sections to scattering coefficients requires more profound theoretical considerations.

It is important to note that the FDTD method can, in principle, be used to model light propagation on the bulk tissue level. Extensive memory requirements, however, render such an analysis impractical, at least with computational resources currently available.

In summary, the computational work described in this dissertation can be extended to develop more sophisticated and refined models of light propagation in tissues. These models will be instrumental in devising strategies to optimize design of next-generation *in vivo* systems, and will provide guidelines to exploit the clinical potential of optical diagnostic techniques to the utmost extent.

# References

1. J. R. Mourant, I. J. Bigio, J. Boyer, R. L. Conn, T. Johnson, and T. Shimada, “Spectroscopic diagnosis of bladder cancer with elastic light scattering,” *Lasers in Surgery and Medicine* **17**, 350-357 (1995).

2. F. Koenig, R. Larne, H. Enquist, F. J. McGovern, K. T. Schomacker, N. Kollias, and T. F. Deutsch, “Spectroscopic measurement of diffuse reflectance for enhanced detection of bladder carcinoma,” *Urology* **51**, 342-345 (1998).

3. G. Zonios, L. T. Perelman, V. Backman, R. Manoharan, M. Fitzmaurice, J. Van Dam, and M. S. Feld, “Diffuse reflectance spectroscopy of human adenomatous colon polyps *in vivo*,” *Applied Optics* **38**, 6628-6637 (1999).

4. I. J. Bigio, S. G. Bown, G. Briggs, C. Kelley, S. Lakhani, D. Pickard, P. M. Ripley, I. G. Rose, and C. Saunders, “Diagnosis of breast cancer using elastic-scattering spectroscopy: preliminary clinical results,” *Journal of Biomedical Optics* **5**, 221-228 (2000).

5. I. Georgakoudi, B. C. Jacobson, J. Van Dam, V. Backman, M. B. Wallace, M. G. Müller, Q. Zhang, K. Badizadegan, D. Sun, G. A. Thomas, L. T. Perelman, and M. S. Feld, “Fluorescence, reflectance, and light-scattering spectroscopy for evaluating dysplasia in patients with Barrett’s esophagus,” *Gastroenterology* **120**, 1620-1629 (2001).

6. M. G. Müller, T. A. Valdez, I. Georgakoudi, V. Backman, C. Fuentes, S. Kabani, N. Laver, Z. Wang, C. W. Boone, R. R. Dasari, S. M. Shapshay, and M. S. Feld, “Spectroscopic detection and evaluation of morphologic and biochemical changes in early human oral carcinoma,” *Cancer* **97**, 1681-1692 (2003).

7. A. Garcia-Uribe, N. Kehtarnavaz, G. Marquez, V. Prieto, M. Duvic, and L. V. Wang, “Skin cancer detection by spectroscopic oblique-incidence reflectometry: classification and physiological origins,” *Applied Optics* **43**, 2643-2650 (2004).

8. R. J. Nordstrom, L. Burke, J. M. Niloff, and J. F. Myrtle, “Identification of cervical intraepithelial neoplasia (CIN) using UV-excited fluorescence and

diffuse-reflectance tissue spectroscopy," *Lasers in Surgery and Medicine* **29**, 118-127 (2001).

9. I. Georgakoudi, E. E. Sheets, M. G. Müller, V. Backman, C. P. Crum, K. Badizadegan, R. R. Dasari, and M. S. Feld, "Trimodal spectroscopy for the detection and characterization of cervical precancers *in vivo*," *American Journal of Obstetrics and Gynecology* **186**, 374-382 (2002).

10. Y. N. Mirabal, S. K. Chang, E. N. Atkinson, A. Malpica, M. Follen, and R. Richards-Kortum, "Reflectance spectroscopy for *in vivo* detection of cervical precancer," *Journal of Biomedical Optics* **7**, 587-594 (2002).

11. W. K. Huh, R. M. Cestero, F. A. Garcia, M. A. Gold, R. S. Guido, K. McIntyre-Seltman, D. M. Harper, L. Burke, S. T. Sum, R. F. Flewelling, and R. D. Alvarez, "Optical detection of high-grade cervical intraepithelial neoplasia *in vivo*: results of a 604-patient study," *American Journal of Obstetrics and Gynecology* **190**, 1249-1257 (2004).

12. M. P. Bard, A. Amelink, M. Skurichina, M. den Bakker, S. A. Burgers, J. P. van Meerbeeck, R. P. Duin, J. G. Aerts, H. C. Hoogsteden, H. J. Sterenborg, "Improving the specificity of fluorescence bronchoscopy for the analysis of neoplastic lesions of the bronchial tree by combination with optical spectroscopy: preliminary communication," *Lung Cancer* **47**, 41-47 (2005).

13. R. Drezek, M. Guillaud, T. Collier, I. Boiko, A. Malpica, C. MacAulay, M. Follen, and R. Richards-Kortum, "Light scattering from cervical cells throughout neoplastic progression: influence of nuclear morphology, DNA content, and chromatin texture," *Journal of Biomedical Optics* **8**, 7-16 (2003).

14. K. J. Heppner, L. M. Matrisian, R. A. Jensen, and W. H. Rodgers, "Expression of most matrix metalloproteinase family members in breast cancer represents a tumor-induced host response," *The American Journal of Pathology* **149**, 273-282 (1996).

15. W. C. Parks, *Matrix Metalloproteinases*, Academic, San Diego (1998).

16. I. Pavlova, K. Sokolov, R. Drezek, A. Malpica, M. Follen, and R. Richards-Kortum, "Microanatomical and biochemical origins of normal and precancerous cervical autofluorescence using laser-scanning fluorescence confocal microscopy," *Photochemistry and Photobiology* **77**, 550-555 (2003).

17. P. Wilder-Smith, K. Osann, N. Hanna, N. El Abbadi, M. Brenner, D. Messadi, and T. Krasieva, "*In vivo* multiphoton fluorescence imaging: a novel approach to oral malignancy," *Lasers in Surgery and Medicine* **35**, 96-103 (2004).

18. P. Ravazoula, V. Zolota, O. Hatjicondi, G. Sakellaropoulos, G. Kourounis, and M. E. Maragoudakis, "Assessment of angiogenesis in human cervical lesions," *Anticancer Research* **16**, 3861-3864 (1996).

19. J. S. Lee, H. S. Kim, J. J. Jung, M. C. Lee, and C. S. Park, "Angiogenesis, cell proliferation and apoptosis in progression of cervical neoplasia," *Analytical and Quantitative Cytology and Histology* **24**, 103-113 (2002).

20. M. G. Müller, I. Georgakoudi, Q. Zhang, J. Wu, and M. S. Feld, "Intrinsic fluorescence spectroscopy in turbid media: disentangling effects of scattering and absorption," *Applied Optics* **40**, 4633-4646 (2001).

21. V. Backman, R. Gurjar, K. Badizadegan, I. Itzkan, R. R. Dasari, L. T. Perelman, and M. S. Feld, "Polarized light scattering spectroscopy for quantitative measurement of epithelial cellular structures *in situ*," *IEEE Journal of Selected Topics in Quantum Electronics* **5**, 1019-1026 (1999).

22. K. Sokolov, R. A. Drezek, K. Gossage, and R. R. Richards-Kortum, "Reflectance spectroscopy with polarized light: is it sensitive to cellular and nuclear morphology?," *Optics Express* **5**, 302-317 (1999).

23. W. M. Star, "Diffusion theory of light transport," in *Optical-Thermal Response of Laser-Irradiated Tissue*, A. J. Welch and M. J. C. van Gemert, eds., Plenum, New York (1995).

24. T. J. Farrell, M. S. Patterson, B. Wilson, "A diffusion theory model of spatially resolved, steady-state diffuse reflectance for the noninvasive determination of tissue optical properties *in vivo*," *Medical Physics* **19**, 879-888 (1992).

25. P. Thueler, I. Charvet, F. Bevilacqua, M. St. Ghislain, G. Ory, P. Marquet, P. Meda, B. Vermeulen, and C. Depeursinge, "*In vivo* endoscopic tissue diagnostics based on spectroscopic absorption, scattering, and phase function properties," *Journal of Biomedical Optics* **8**, 495-503 (2003).

26. B. Chen, K. Stamnes, and J. J. Stamnes, "Validity of the diffusion approximation in bio-optical imaging," *Applied Optics* **40**, 6356-6366 (2001).

27. J. Ripoll, D. Yessayan, G. Zacharakis, and V. Ntziachristos, "Experimental determination of photon propagation in highly absorbing and scattering media," *Journal of the Optical Society of America A* **22**, 546-551 (2005).

28. S. L. Jacques and L. Wang, "Monte Carlo modeling of light transport in tissues," in *Optical-Thermal Response of Laser-Irradiated Tissue*, A. J. Welch and M. J. C. van Gemert, eds., Plenum, New York (1995).

29. R. Drezek, K. Sokolov, U. Utzinger, I. Boiko, A. Malpica, M. Follen, and R. Richards-Kortum, "Understanding the contributions of NADH and collagen to cervical tissue fluorescence spectra: modeling, measurements, and implications," *Journal of Biomedical Optics* **6**, 385-396 (2001).

30. I. V. Meglinski and S. J. Matcher, "Computer simulation of the skin reflectance spectra," *Computer Methods and Programs in Biomedicine* **70**, 179-186 (2003).

31. D. Hidovic-Rowe and E. Claridge, "Modelling and validation of spectral reflectance for the colon," *Physics in Medicine and Biology* **50**, 1071-1093 (2005).

32. I. V. Meglinskii and S. D. Matcher, "Analysis of the spatial distribution of detector sensitivity in a multilayer randomly inhomogeneous medium with strong light scattering and absorption by the Monte Carlo method," *Optics and Spectroscopy* **91**, 654-659 (2001).

33. T. J. Pfefer, K. T. Schomacker, M. N. Ediger, and N. S. Nishioka, "Light propagation in tissue during fluorescence spectroscopy with single-fiber probes," *IEEE Journal of Selected Topics in Quantum Electronics* **7**, 1004-1012 (2001).

34. T. J. Pfefer, K. T. Schomacker, M. N. Ediger, and N. S. Nishioka, "Multiple-fiber probe design for fluorescence spectroscopy in tissue," *Applied Optics* **41**, 4712-4721 (2002).

35. M. Larsson, W. Steenbergen, and T. Strömberg, "Influence of optical properties and fiber separation on laser doppler flowmetry," *Journal of Biomedical Optics* **7**, 236-243 (2002).

36. C. Zhu, Q. Liu, and N. Ramanujam, "Effect of fiber optic probe geometry on depth-resolved fluorescence measurements from epithelial tissues: a Monte Carlo simulation," *Journal of Biomedical Optics* **8**, 237-247 (2003).

37. M. C. Skala, G. M. Palmer, C. Zhu, Q. Liu, K. M. Vrotsos, C. L. Marshek-Stone, A. Gendron-Fitzpatrick, and N. Ramanujam, "Investigation of fiber-optic probe designs for optical spectroscopic diagnosis of epithelial pre-cancers," *Lasers in Surgery and Medicine* **34**, 25-38 (2004).

38. T. J. Pfefer, L. S. Matchette, C. L. Bennett, J. A. Gall, J. N. Wilke, A. J. Durkin, and M. N. Ediger, "Reflectance-based determination of optical properties in highly attenuating tissue," *Journal of Biomedical Optics* **8**, 206-215 (2003).

39. J. Swartling, J. S. Dam, and S. Andersson-Engels, "Comparison of spatially and temporally resolved diffuse-reflectance measurement systems for determination of biomedical optical properties," *Applied Optics* **42**, 4612-4620 (2003).

40. J. Wu, F. Partovi, M. S. Feld, and R. P. Rava, "Diffuse reflectance from turbid media: an analytical model of photon migration," *Applied Optics* **32**, 1115-1121 (1993).

41. A. Taflove, *Computational Electrodynamics: The Finite-Difference Time-Domain Method*, Artech House, Norwood (1995).

42. A. Taflove, ed., *Advances in Computational Electrodynamics: The Finite-Difference Time-Domain Method*, Artech House, Norwood (1998).

43. A. Dunn, R. Richards-Kortum, "Three-dimensional computation of light scattering from cells," *IEEE Journal of Selected Topics in Quantum Electronics* **2**, 898-905 (1996).

44. R. Drezek, A. Dunn, R. Richards-Kortum, "Light scattering from cells: finite-difference time-domain simulations and goniometric measurements," *Applied Optics* **38**, 3651-3661 (1999).

45. R. Drezek, A. Dunn, R. Richards-Kortum, "A pulsed finite-difference time-domain (FDTD) method for calculating light scattering from biological cells over broad wavelength ranges," *Optics Express* **6**, 147-157 (2000).

46. H. Jiangping, A. Karlsson, J. Swartling, and S. Andersson-Engels, "Light scattering by multiple red blood cells," *Journal of the Optical Society of America A* **21**, 1953-1961 (2004).

47. A. Karlsson, H. Jiangping, J. Swartling, and S. Andersson-Engels, “Numerical simulations of light scattering by red blood cells,” *IEEE Transactions on Biomedical Engineering* **52**, 13-18 (2005).

48. C. Liu, C. Capjack, and W. Rozmus, “3-D simulation of light scattering from biological cells and cell differentiation,” *Journal of Biomedical Optics* **10**, 014007 (2005).

49. J. Q. Lu, P. Yang, and X. Hu, “Simulations of light scattering from a biconcave red blood cell using the finite-difference time-domain method,” *Journal of Biomedical Optics* **10**, 024022 (2005).

50. L. Wang, S. L. Jacques, and L. Zheng, “MCML – Monte Carlo modeling of light transport in multi-layered tissues,” *Computer Methods and Programs in Biomedicine* **47**, 131-146 (1995).

51. A. J. Welch, C. Gardner, R. Richards-Kortum, E. Chan, G. Criswell, J. Pfefer, and S. Warren, “Propagation of fluorescent light,” *Lasers in Surgery and Medicin*e **21**, 166-178 (1997).

52. L. Wang and S. L. Jacques, “Monte Carlo modeling of light transport in muli-layered tissues in standard C,” MCML Software Manual, see http:// omlc.ogi.edu/pubs/pdf/man_mcml.pdf, Oregon Medical Laser Center (1998).

53. A. Taflove and M. E. Brodwin, “Numerical solution of steady-state electromagnetic scattering problems using the time-dependent Maxwell’s equations,” *IEEE Transactions on Microwave Theory and Techniques* **23**, 623-630 (1975).

54. J. Berenger, “A perfectly matched layer for the absorption of electromagnetic waves,” *Journal of Computational Physics* **114**, 185-200 (1994).

55. J. Berenger, “Three-dimensional perfectly matched layer for the absorption of electromagnetic waves,” *Journal of Computational Physics* **127**, 363-379 (1996).

56. D. S. Katz, E. T. Thiele, and A. Taflove, “Validation and extension to three dimensions of the Berenger PML absorbing boundary condition for FDTD meshes,” *IEEE Microwave and Guided Wave Letters* **4**, 268-270 (1994).

57. J. Berenger, "Perfectly matched layer for the FDTD solution of wave-structure interaction problems," *IEEE Transactions on Antennas and Propagation* **44**, 110-117 (1996).

58. J. Berenger, "Improved PML for the FDTD solution of wave-structure interaction problems," *IEEE Transactions on Antennas and Propagation* **45**, 466-473 (1997).

59. C. A. Balanis, *Advanced Engineering Electromagnetics*, Wiley, New York (1989).

60. H. C. van de Hulst, *Light Scattering by Small Particles*, Dover, New York (1981).

61. C. F. Bohren and D. R. Huffman, *Absorption and Scattering of Light by Small Particles*, Wiley, New York (1998).

62. D. Arifler, "Modeling light scattering from cells using the finite-difference time-domain method with a perfectly matched layer boundary condition," MS Thesis, Biomedical Engineering Department, The University of Texas at Austin (2002).

63. A. Dunn, "Light scattering properties of cells," PhD Dissertation, Electrical and Computer Engineering Department, The University of Texas at Austin (1997).

64. A. H. Gandjbakhche, R. F. Bonner, A. E. Arai, and R. S. Balaban, "Visible-light photon migration through myocardium *in vivo*," *American Journal of Physiology* **277**, H698-H704 (1999).

65. D. A. Boas, J. P. Culver, J. J. Stott, and A. K. Dunn, "Three dimensional Monte Carlo code for photon migration through complex heterogeneous media including the adult human head," *Optics Express* **10**, 159-170 (2002).

66. M. S. Patterson, S. Andersson-Engels, B. C. Wilson, and E. K. Osei, "Absorption spectroscopy in tissue-simulating materials: a theoretical and experimental study of photon paths," *Applied Optics* **34**, 22-30 (1995).

67. U. Utzinger and R. Richards-Kortum, "Fiber optic probes for biomedical optical spectroscopy," *Journal of Biomedical Optics* **8**, 121-147 (2003).

68. M. Larsson, H. Nilsson, and T. Strömberg, "*In vivo* determination of local skin optical properties and photon path length by use of spatially resolved

diffuse reflectance with applications in laser Doppler flowmetry," *Applied Optics* **42**, 124-134 (2003).

69. A. Pifferi, J. Swartling, E. Chikoidze, A. Torricelli, P. Taroni, A. Bassi, S. Andersson-Engels, and R. Cubeddu, "Spectroscopic time-resolved diffuse reflectance and transmittance measurements of the female breast at different interfiber distances," *Journal of Biomedical Optics* **9**, 1143-1151 (2004).

70. C. Zhu, G. M. Palmer, T. M. Breslin, F. Xu, and N. Ramanujam, "Use of a multiseparation fiber optic probe for the optical diagnosis of breast cancer," *Journal of Biomedical Optics* **10**, 024032 (2005).

71. S. K. Chang, D. Arifler, R. Drezek, M. Follen, and R. Richards-Kortum, "An analytical model to describe fluorescence spectra of normal and pre-neoplastic epithelial tissue: comparison with Monte Carlo simulations and clinical measurements," *Journal of Biomedical Optics* **9**, 511-522 (2004).

72. J. C. Finlay and T. H. Foster, "Hemoglobin oxygen saturations in phantoms and *in vivo* from measurements of steady-state diffuse reflectance at a single, short source-detector separation," *Medical Physics* **31**, 1949-1959 (2004).

73. J. C. Finlay and T. H. Foster, "Recovery of hemoglobin oxygen saturation and intrinsic fluorescence with a forward-adjoint model," *Applied Optics* **44**, 1917-1933 (2005).

74. R. L. P. van Veen, A. Amelink, M. Menke-Pluymers, C. van der Pol, and H. J. C. M. Sterenborg, "Optical biopsy of breast tissue using differential path-length spectroscopy," *Physics in Medicine and Biology* **50**, 2573-2581 (2005).

75. P. R. Bargo, S. A. Prahl, T. T. Goodell, R. A. Sleven, G. Koval, G. Blair, and S. L. Jacques, "*In vivo* determination of optical properties of normal and tumor tissue with white light reflectance and an empirical light transport model during endoscopy," *Journal of Biomedical Optics* **10**, 034018 (2005).

76. D. C. Walker, B. H. Brown, A. D. Blackett, J. Tidy, and R. H. Smallwood, "A study of the morphological parameters of cervical squamous epithelium," *Physiological Measurement* **24**, 121-135 (2003).

77. T. Collier, D. Arifler, A. Malpica, M. Follen, and R. Richards-Kortum, "Determination of epithelial tissue scattering coefficient using confocal microscopy," *IEEE Journal of Selected Topics in Quantum Electronics* **9**, 307-313 (2003).

78. J. Qu, C. MacAulay, S. Lam, and B. Palcic, "Optical properties of normal and carcinomatous bronchial tissue," *Applied Optics* **33**, 7397-7405 (1994).

79. S. Prahl, "Optical absorption of hemoglobin," see http://omlc.ogi.edu/spectra/hemoglobin/, Oregon Medical Laser Center (1999).

80. I. V. Meglinski and S. J. Matcher, "Quantitative assessment of skin layers absorption and skin reflectance spectra simulation in the visible and near-infrared spectral regions," *Physiological Measurement* **23**, 741-753 (2002).

81. S. L. Jacques, "Skin optics," see http://omlc.ogi.edu/news/jan98/skinoptics.html, Oregon Medical Laser Center (1998).

82. C. Brookner, U. Utzinger, M. Follen, R. Richards-Kortum, D. Cox, and E. N. Atkinson, "Effects of biographical variables on cervical fluorescence emission spectra," *Journal of Biomedical Optics* **8**, 479-483 (2003).

83. A. J. Bailey, R. G. Paul, and L. Knott, "Mechanisms of maturation and ageing of collagen," *Mechanisms of Ageing and Development* **106**, 1-56 (1998).

84. L. G. Koss, *Diagnostic Cytology and Its Histopathologic Bases*, Lippincott, Philadelphia (1992).

85. T. J. Pfefer, L. S. Matchette, A. M. Ross, and M. N. Ediger, "Selective detection of fluorophore layers in turbid media: the role of fiber-optic probe design," *Optics Letters* **28**, 120-122 (2003).

86. T. Papaioannou, N. W. Preyer, Q. Fang, A. Brightwell, M. Carnohan, G. Cottone, R. Ross, L. R. Jones, and L. Marcu, "Effects of fiber-optic probe design and probe-to-target distance on diffuse reflectance measurements of turbid media: an experimental and computational study at 337 nm," *Applied Optics* **43**, 2846-2860 (2004).

87. T. P. Moffitt and S. A. Prahl, "Sized-fiber reflectometry for measuring local optical properties," *IEEE Journal of Selected Topics in Quantum Electronics* **7**, 952-958 (2001).

88. L. Nieman, A. Myakov, J. Aaron, and K. Sokolov, "Optical sectioning using a fiber probe with an angled illumination-collection geometry: evaluation in engineered tissue phantoms," *Applied Optics* **43**, 1308-1319 (2004).

89. T. A. Winning and G. C. Townsend, “Oral mucosal embryology and histology,” *Clinics in Dermatology* **18**, 499-511 (2000).

90. A. Amelink and H. J. C. M. Sterenborg, “Measurement of the local optical properties of turbid media by differential path-length spectroscopy,” *Applied Optics* **43**, 3048-3054 (2004).

91. Y. L. Kim, Y. Liu, V. M. Turzhitsky, H. K. Roy, R. K. Wali, and V. Backman, “Coherent backscattering spectroscopy,” *Optics Letters* **29**, 1906-1908 (2004).

92. Y. L. Kim, Y. Liu, R. K. Wali, H. K. Roy, and V. Backman. “Low-coherent backscattering spectroscopy for tissue characterization,” *Applied Optics* **44**, 366-377 (2005).

93. R. M. Verdaasdonk and C. Borst, “Optics of fibers and fiber probes,” in *Optical-Thermal Response of Laser-Irradiated Tissue*, A. J. Welch and M. J. C. van Gemert, eds., Plenum, New York (1995).

94. J. T. Motz, M. Hunter, L. H. Galindo, J. A. Gardecki, J. R. Kramer, R. R. Dasari, and M. S. Feld, “Optical fiber probe for biomedical Raman spectroscopy,” *Applied Optics* **43**, 542-554 (2004).

95. R. A. Schwarz, D. Arifler, S. K. Chang, I. Pavlova, I. A. Hussain, V. Mack, B. Knight, A. M. Gillenwater, and R. Richards-Kortum, “Ball lens coupled fiber-optic probe for depth-resolved spectroscopy of epithelial tissue,” *Optics Letters* **30**, 1159-1161 (2005).

96. K. J. Busam, K. Hester, C. Charles, D. L. Sachs, C. R. Antonescu, S. Gonzalez, and A. C. Halpern, “Detection of clinically amelonatic malignant melanoma and assessment of its margins by *in vivo* confocal scanning laser microscopy,” *Archives of Dermatology* **137**, 923-929 (2001).

97. M. Rajadhyaksha, G. Menaker, T. Flotte, P. J. Dwyer, and S. Gonzalez, “Confocal examination of nonmelanoma cancers in thick skin excisions to potentially guide mohs micrographic surgery without frozen histopathology,” *Journal of Investigative Dermatology* **117**, 1137-1143 (2001).

98. T. Collier, A. Lacy, R. Richards-Kortum, A. Malpica, and M. Follen, “Near real time confocal microscopy of amelanotic tissue: detection of dysplasia in *ex vivo* cervical tissue,” *Academic Radiology* **9**, 504-512 (2002).

99. A. L. Clark, A. M. Gillenwater, T. G. Collier, R. Alizadeh-Naderi, A. K. El-Naggar, and R. R. Richards-Kortum, "Confocal microscopy for real-time detection of oral cavity neoplasia," *Clinical Cancer Research* **9**, 4714-4721 (2003).

100. C. A. Jesser, S. A. Boppart, C. Pitris, D. L. Stamper, G. P. Nielsen, M. E. Brezinski, and J. G. Fujimoto, "High resolution imaging of transitional cell carcinoma with optical coherence tomography: feasibility for the evaluation of bladder pathology," *The British Journal of Radiology* **72**, 1170-1176 (1999).

101. C. Pitris, C. Jesser, S. A. Boppart, D. Stamper, M. E. Brezinski, and J. G. Fujimoto, "Feasibility of optical coherence tomography for high-resolution imaging of human gastrointestinal tract malignancies," *Journal of Gastroenterology* **35**, 87-92 (2000).

102. J. M. Poneros, S. Brand, B. E. Bouma, G. J. Tearney, C. C. Compton, and N. S. Nishioka, "Diagnosis of specialized intestinal metaplasia by optical coherence tomography," *Gastroenterology* **120**, 7-12 (2001).

103. A. L. Clark, A. Gillenwater, R. Alizadeh-Naderi, A. K. El-Naggar, and R. Richards-Kortum, "Detection and diagnosis of oral neoplasia with an optical coherence microscope," *Journal of Biomedical Optics* **9**, 1271-1280 (2004).

104. J. Thiran and B. Macq, "Morphological feature extraction for the classification of digital images of cancerous tissues," *IEEE Transactions on Biomedical Engineering* **43**, 1011-1020 (1996).

105. K. Erhardt, G. Auer, E. Bjorkholm, G. Forsslund, B. Moberger, C. Silfversward, G. Wicksell, and A. Zetterberg, "Prognostic significance of nuclear DNA content in serious ovarian tumors," *Cancer Research* **44**, 2198-2202 (1984).

106. C. J. Rodenburg, C. J. Cornelisse, P. A. M. Heintz, J. Hermans, and G. J. Fleuren, "Tumor ploidy as a major prognostic factor in advanced ovarian cancer," *Cancer* **59**, 317-323 (1987).

107. J. R. Mourant, M. Canpolat, C. Brocker, O. Esponda-Ramos, T. M. Johnson, A. Matanock, K. Stetter, and J. P. Freyer, "Light scattering from cells: the contribution of the nucleus and the effects of proliferative status," *Journal of Biomedical Optics* **5**, 131-137 (2000).

108. C. Yang, L. T. Perelman, A. Wax, R. R. Dasari, and M. S. Feld, "Feasibility of field-based light scattering spectroscopy," *Journal of Biomedical Optics* **5**, 138-143 (2000).

109. R. S. Gurjar, V. Backman, L. T. Perelman, I. Georgakoudi, K. Badizadegan, I. Itzkan, R. R. Dasari, and M. S. Feld, "Imaging human epithelial properties with polarized light-scattering spectroscopy," *Nature Medicine* **7**, 1245-1248 (2001).

110. J. R. Mourant, J. P. Freyer, A. H. Hielscher, A. A. Eick, D. Shen, and T. M. Johnson, "Mechanisms of light scattering from biological cells relevant to noninvasive optical-tissue diagnostics," *Applied Optics* **37**, 3586-3593 (1998).

111. M. Guillaud, A. Doudkine, D. Garner, C. MacAulay, and B. Palcic, "Malignancy associated changes in cervical smears: systematic changes in cytometric features with the grade of dysplasia," *Analytical Cellular Pathology* **9**, 191-204 (1995).

112. I. Ramzy, *Essentials of Gynecologic and Obstetric Pathology*, Appleton-Century-Crofts, Norwalk (1983).

113. R. Barer, "Refractometry and interferometry of living cells," *Journal of the Optical Society of America* **47**, 545-556 (1957).

114. A. Brunsting and P. Mullaney, "Differential light scattering from spherical mammalian cells," *Biophysical Journal* **14**, 439-453 (1974).

115. J. M. Schmitt and G. Kumar, "Turbulent nature of refractive-index variations in biological tissue," *Optics Letters* **21**, 1310-1312 (1996).

116. R. A. Drezek, T. Collier, C. K. Brookner, A. Malpica, R. Lotan, R. R. Richards-Kortum, and M. Follen, "Laser scanning confocal microscopy of cervical tissue before and after application of acetic acid," *American Journal of Obstetrics and Gynecology* **182**, 1135-1139 (2000).

117. J. R. Mourant, T. M. Johnson, V. Doddi, and J. P. Freyer, "Angular dependent light scattering from multicellular spheroids," *Journal of Biomedical Optics* **7**, 93-99 (2002).

118. Y. Pan, J. P. Lavelle, S. I. Bastacky, S. Meyers, G. Pirtskhalaishvili, M. L. Zeidel, and D. L. Farkas, "Detection of tumorigenesis in rat bladders with optical coherence tomography," *Medical Physics* **28**, 2432-2440 (2001).

119. D. E. Freund, R. L. McCally, and R. A. Farrell, “Effects of fibril orientations on light scattering in the cornea,” *Journal of the Optical Society of America A* **3**, 1970-1982 (1986).

120. I. S. Saidi, S. L. Jacques, and F. K. Tittel, “Mie and Rayleigh modeling of visible-light scattering in neonatal skin,” *Applied Optics* **34**, 7410-7418 (1995).

121. M. H. Ross, L. J. Romrell, and G. I. Kaye, *Histology: A Text and Atlas*, Lippincott, Baltimore (1995).

122. T. Ushiki, “Collagen fibers, reticular fibers and elastic fibers: a comprehensive understanding from a morphological viewpoint,” *Archives of Histology and Cytology* **65**, 109-126 (2002).

123. B. Eyden and M. Tzaphlidou, “Structural variations of collagen in normal and pathological tissues: role of electron microscopy,” *Micron* **32**, 287-300 (2001).

124. J. Wu, B. Rajwa, D. L. Filmer, C. M. Hoffmann, B. Yuan, C. Chiang, J. Sturgis, and J. P. Robinson, “Automated quantification and reconstruction of collagen matrix from 3D confocal datasets,” *Journal of Microscopy* **210**, 158-165 (2003).

125. R. Richards-Kortum and E. Sevick-Muraca, “Quantitative optical spectroscopy for tissue diagnosis,” *Annual Review of Physical Chemistry* **47**, 555-606 (1996).

126. P. Friedl, “Dynamic imaging of cellular interactions with extracellular matrix,” *Histochemistry and Cell Biology* **122**, 183-190 (2004).

127. W. R. Zipfel, R. M. Williams, R. Christie, A. Y. Nikitin, B. T. Hyman, and W. W. Webb, “Live tissue intrinsic emission microscopy using multiphoton-excited native fluorescence and second harmonic generation,” *Proceedings of the National Academy of Sciences* **100**, 7075-7080 (2003).

128. A. Zoumi, X. Lu, G. S. Kassab, and B. Tromberg, “Imaging coronary artery microstructure using second-harmonic and two-photon fluorescence microscopy,” *Biophysical Journal* **87**, 2778-2786 (2004).

129. K. Sokolov, J. Galvan, A. Myakov, A. Lacy, R. Lotan, and R. Richards-Kortum, “Realistic three-dimensional epithelial tissue phantoms for biomedical optics,” *Journal of Biomedical Optics* **7**, 148-156 (2002).

130. R. O. Duda, P. E. Hart, and D. G. Stork, *Pattern Classification*, Wiley, New York (2001).

131. R. M. Haralick, K. Shanmugam, and I. Dinstein, "Textural features for image classification," *IEEE Transactions on Systems, Man, and Cybernetics* **SMC-3**, 610-621 (1973).

132. H. Soltanian-Zadeh, F. Rafiee-Rad, and S. Pourabdollah-Nejad D, "Comparison of multiwavelet, wavelet, Haralick, and shape features for microcalcification classification in mammograms," *Pattern Recognition* **37**, 1973-1986 (2004).

133. J. R. Mourant, J. Boyer, A. H. Hielscher, and I. J. Bigio, "Influence of the scattering phase function on light transport measurements in turbid media performed with small source-detector separations," *Optics Letters* **21**, 546-548 (1996).

134. F. Bevilacqua and C. Depeursinge, "Monte Carlo study of diffuse reflectance at source-detector separations close to one transport mean free path," *Journal of the Optical Society of America A* **16**, 2935-2945 (1999).

135. A. Ishimaru, *Wave Propagation and Scattering in Random Media, Vol. 1: Single Scattering and Transport Theory*, Academic, San Diego (1978).

# Vita

Dizem Arifler, the daughter of Gunay and Soner Arifler, was born in Nicosia, Cyprus on September 19, 1979. In 1996, she was awarded a full scholarship through the Cyprus-America Scholarship Program to study Physics at The University of Texas at Austin. She received her B.S. degree in Physics (Highest Honors) in May 2000. In August 2000, she entered the Graduate School at The University of Texas at Austin where she received her M.S. degree in Biomedical Engineering in May 2002. She continued her studies towards a Ph.D. degree in Biomedical Engineering immediately after receiving her M.S. degree. In 2003, she was awarded a Cullen Trust Student Endowment Fellowship through the Graduate School of The University of Texas at Austin.

Permanent address: Malazgirt Sokak
Yetkili 2 Apartmani, No: 4
Kyrenia, Cyprus

This dissertation was typed by the author.